THESIS

MINIMIZING THE IMPACT OF FILAMENT QUALITY ON FDM PARTS USING FEED FORWARD CONTROL

Submitted by

Rohan Madhu

Department of Mechanical Engineering

In partial fulfillment of the requirements

For the Degree of Master of Science

Colorado State University

Fort Collins, Colorado

Summer 2026

Master's Committee:

Advisor: David Prawel

Wade Troxell
Steve Simske

ABSTRACT

MINIMIZING THE IMPACT OF FILAMENT QUALITY ON FDM PARTS USING FEED FORWARD CONTROL

The quality of fused deposition modeling (FDM) parts is strongly influenced by variations in filament geometry and consistency, particularly diameter deviations that disrupt the intended volumetric flow into the melt zone. These fluctuations can lead to poor inter-layer bonding and internal voids, both of which reduce mechanical performance.

This research presents a Feed Forward (FFC) Control system developed to minimize the effect of filament dimensional variability on print quality. The system employs dual orthogonal diameter sensors to continuously monitor real-time filament geometry and compute the instantaneous volumetric error relative to the nominal 1.75 mm target. Using this data, the algorithm preemptively adjusts feed rate before deposition, compensating for under or over extrusion without relying on slower feedback corrections.

The performance of the FFC system is evaluated through comprehensive experiments involving over 200,000 logged data points and 240 printed specimens across multiple commercial filament vendors. Key performance indicators include diameter precision, pressure decay rate (leaks) in sealed tubes and tensile strength of test coupons. Pressure decay rate was selected as a functional performance metric, as it directly captures leakage behavior arising from internal porosity and volumetric inconsistencies, thereby providing a practical measure of part quality. Tensile strength was used as a measure of mechanical performance, reflecting the quality of interlayer bonding of printed parts under load. Results show that FFC control significantly improves extrusion uniformity, leading to higher tensile strength and lower leak rates. Furthermore, statistical analysis reveals that filament prices do not consistently correlate with geometric or mechanical quality; in several cases, lower cost filaments achieved equivalent or superior performance to premium filaments.

In summary, this study delivers a practically deployable Feed Forward Control strategy for desktop FDM printers that compensates for filament variability using low-cost sensors and open-source firmware modifications.

ACKNOWLEDGEMENTS

Two years ago, I took a leap of faith in leaving behind a stable job to pursue a master's degree in mechanical engineering, driven by a desire to deepen my understanding and grow as an engineer. This journey was not just about academics, but about reconnecting with the curiosity that first drew me to engineering; building, questioning, and continuously improving.

I would like to express my sincere gratitude to Dr. David Prawel for giving me the opportunity to be a part of his lab and for his constant guidance throughout this journey. Your patience, persistence, and ability to challenge my thinking played a crucial role in shaping this work. Thank you for being the unstoppable force whenever I found myself acting as the immovable object.

I would like to thank my committee members, Dr. Wade Troxell and Dr. Steve Simske, for their time, guidance, and valuable insights, which greatly contributed to improving the quality of this work. This work builds upon the strong foundation laid by Tyler Gerry and Daniel Watling, who developed the feed-forward control system. I am grateful for the opportunity to further explore and improve upon their contributions. As with any meaningful engineering system, feed-forward control was not developed in a day, but through continuous iteration, experimentation, and learning.

My journey in engineering has always been rooted in hands-on problem solving, from my early experiences of building mechanical models to later designing and developing systems in academic and professional settings. That mindset of learning through building and refining has strongly influenced the way I approached this research.

I have also had the privilege of working with several talented undergraduate students at Colorado State University; Liam Yieter, Maddie Potter, Aidan Bracy, Nicholas Clark, Mia Allen, Sarah Goudjil, and Kelli McGuire, whose efforts and collaboration have contributed to this work in many ways.

I would like to thank my peers and colleagues at SAMD and ARC at CSU for fostering a supportive and collaborative environment, and for providing access to the tools and machines that made this research possible.

I would also like to thank Dr. Dean Bartles and George Barnych for their support in sponsoring this research and for asking insightful questions that challenged our assumptions and helped drive the project in new and meaningful directions.

Finally, I would like to thank the two most important people in my life, my parents. From my earliest days of curiosity, when my father first guided me through assembling my first mechanical system and my mom helping me solve Tangram puzzles, to this moment, their support has been unwavering. They have been the constant circle around my life, giving me the courage to take risks, pursue higher education, and discover a path that I truly enjoy.

I am also deeply grateful to the friends I made within the university community ; for the moments of support, laughter, and joy that made this journey all the more meaningful.

TABLE OF CONTENTS

1 CHAPTER 1- AIMS AND METHODS

1.1 Introduction:

Additive manufacturing (AM) has evolved from a rapid prototyping tool into a widely adopted manufacturing approach capable of producing functional end-use components[1], [2], [3]. Among polymer-based AM processes, material extrusion, commonly referred to as fused deposition modeling (FDM) or melt extrusion (MEX), remains the most accessible and widely deployed technology due to its affordability, ease of use, and open-source ecosystem[4]. According to ASTM F42.91 [5]melt extrusion involves the thermal processing and layer-wise deposition of polymer filament to form three-dimensional parts.

Despite its widespread adoption, melt extrusion continues to suffer from inconsistent part quality and limited process reliability. Mechanical strength, interlayer bonding, porosity, and dimensional accuracy are highly sensitive to process parameters including extrusion temperature, layer height, feed rate, ambient conditions, and material variability[6], [7], [8], [9], [10]. Desktop systems in particular exhibit significant variability in as-printed properties, often resulting in failed builds, wasted material, and poor reliability, resulting in reduced confidence in the process for structural applications.

A significant body of research has focused on in-situ monitoring techniques [11], [12], [13] to improve process understanding and defect detection in melt extrusion systems. Sensors measuring vibration, current draw, temperature, acoustic emissions, and visual data have been integrated into printers to detect anomalies during fabrication. Image-based methods and machine learning approaches have been explored to classify print faults and predict build outcomes. However, most prior work has emphasized monitoring and post hoc identification of defects rather than actively preventing their occurrence through real-time control intervention.

One of the most dynamic and influential variables in melt extrusion is filament diameter[14], [15]. Because the volumetric flow rate of extruded material is directly proportional to the filament cross-sectional area and feed rate, even small variations in filament diameter can result in measurable deviations in deposited material volume which directly affects interlayer bonding. Unlike thermal parameters, which are subject to inherent lag and inertia, filament diameter variations represent a non-thermal input disturbance that can theoretically be compensated in real time without dynamic delay.

Commercial polymer filaments are nominally specified at 1.75 mm diameter; however, manufacturing tolerances, material inconsistencies, and handling can introduce localized diameter fluctuations and ovality[16], [17]. These geometric deviations propagate into volumetric deposition errors that may affect:

- Internal density
- Interlayer adhesion
- Porosity distribution
- Tensile strength

While previous research [18] has demonstrated that filament diameter variability can be detected using in-situ sensing, limited work has quantitatively evaluated whether actively compensating for this variability improves structural performance across a broad range of commercially available materials.

This thesis proves real-time feed forward control (FFC) based on dual orthogonal filament diameter sensing can reduce the sensitivity of printed part performance to filament geometric variability. Rather than merely detecting anomalies, the system adjusts the extruder feed rate in real time to maintain consistent volumetric deposition, thereby mitigating under- or over-extrusion caused by filament diameter fluctuations.

To evaluate the effectiveness of this control strategy, two distinct test geometries were employed:

1. Pressure tubes, designed to assess part density and interlayer bonding through pressure decay testing.
2. Tensile coupons, used to quantify mechanical strength and fracture behavior under uniaxial loading.

In this work, "**quality**" is defined through these two complementary performance metrics. Pressure retention reflects the presence of voids and leakage pathways within the printed structure, while tensile strength captures the strength of layer bonding of the printed material. By analyzing both metrics independently, this study differentiates between localized porosity-driven defects and distributed bonding mechanisms that govern structural failure.

Unlike prior studies that introduced seeded filament defects under controlled laboratory conditions[18], this research evaluates naturally occurring diameter variability across ten commercial filament vendors of PETG, representing a wide range of prices. Over 480 printed specimens were fabricated with feed forward control enabled and disabled, allowing statistical comparison across materials, printers, and build conditions.

1.2 Aims:

1. Quantify how feed forward control influences extrusion uniformity and pressure tube leakage.

2. Determine whether FFC reduces the sensitivity of pressure decay behavior to geometric variability.

3. Evaluate the extent to which FFC affects tensile performance across different PETG filaments.

4. Evaluate whether filament geometric characteristics (including diameter variability and ovality) correlate with pressure decay and tensile performance, identify the metrics that strongly predict part quality, and determine whether these geometric properties are associated with filament cost.

1.3 Material and Methods:

In prior work [18], [19], an in-situ filament diameter monitoring system was developed to dynamically adjust the volumetric flow rate during 3D printing. This real-time control significantly improved the consistency of material deposition, reduced occurrences of over- and under-extrusion, and enhanced both layer adhesion and tensile properties of printed parts. To validate the system's effectiveness, controlled deformations were introduced into the filament prior to printing. These deformations created localized reductions in filament diameter, leading to variations in road width and reduced inter-layer bonding strength within the printed structure. A set of pressure tubes was printed using the deformed filament, and their performance was assessed through pressure decay testing. By varying the size and strain of the deformations, the study induced a range of bonding defects. The results showed that when the local volume loss exceeded 40 mm^3, a measurable decline in the printed part's quality (defined above) was observed, demonstrating the sensitivity of bonding performance to filament inconsistency.

1.3.1 Current Study: Installation of upgraded FFC System

Building on this prior work, the current study conducts a large-scale evaluation of the Feed Forward Control (FFC) system using a broader set of materials and performance metrics. A total of 240 pressure tubes and 240 tensile coupons were printed using ten different filament models of different prices to assess the impact of filament variability on both internal pressure retention and tensile strength.

The experimental setup featured a Prusa MK3S+ 3D printer (Prague, Czech Republic) with a single extruder head. A custom-built filament diameter sensor housing was designed to accommodate two orthogonally aligned diameter sensors, enabling real-time monitoring of both primary and secondary filament axes. This configuration allowed for the detection of filament ovality, a key factor in flow rate variation. In addition to filament diameter, the system measured ambient temperature, humidity, and for pressure tubes, the mass of the as-printed part to evaluate consistency in material usage.

The FFC system integrates with Klipper and relies on a Raspberry Pi to run correction algorithms and interface with custom-built hardware. The setup includes:

- A custom filament diameter sensor module measuring filament cross-section in real time.
- A correction algorithm that adjusts the extruder stepper motor rate in proportion to the detected diameter change.
- A calibration file that maps the relationship between extruded volume, diameter, and print speed to ensure accurate compensation across a variety of conditions.

The system architecture is designed to be flexible and easily deployed. The repository includes:

- A Klipper macro (flow_adjust.cfg) that performs the real-time correction.
- Example configuration files (printer.cfg) showing how to integrate the correction routine.
- A logging tool (FFC_log_parser.py) to visualize the correction effect and monitor filament variation during prints.

- A simulation tool (simulator.ipynb) that models the impact of various filament inconsistencies on flow behavior, allowing users to tune correction parameters before deployment.

Dual-sensor housing was fabricated specifically for this study to enable high-precision, orthogonal diameter tracking. This allowed for improved resolution in measuring filament cross-sectional consistency and supported real-time feed rate adjustments as part of the FFC strategy. By combining both pressure decay analysis and tensile testing, this study offers a comprehensive assessment of how filament diameter variability, particularly in cross-sectional shape affects the structural integrity of objects 3D printed using melt extrusion.

1.3.2 Filament Diameter Sensor

The filament diameter sensor used is based on InFiDEL sensor designed by Thomas Sanladerer, with an RP2040 microcontroller and a TMAG5273 Hall effect sensor as the sensing element[19]. A cross-sectional view of the full sensor is shown in Figure 1.

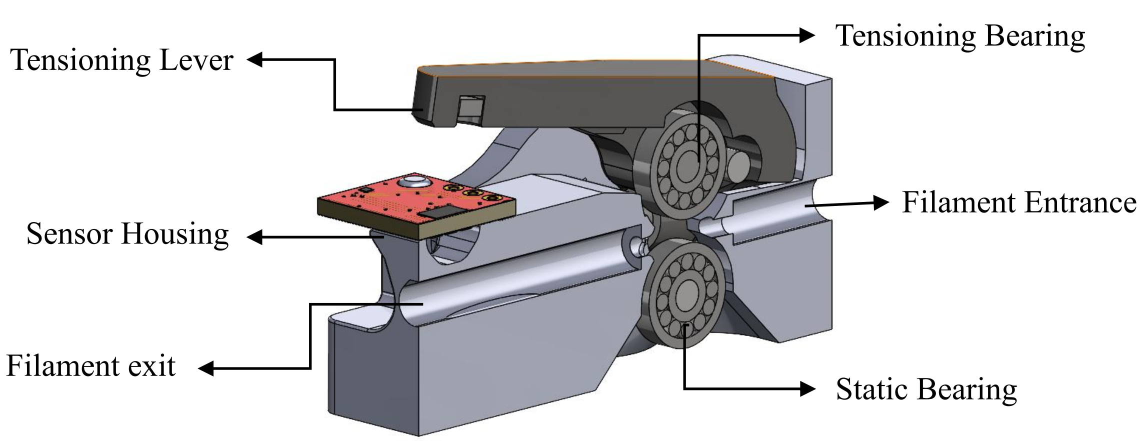

Figure 1-Cross sectional view of Filament Diameter sensor

The filament diameter sensor is mounted in line with the filament path and takes passive measurements of the filament diameter before it enters the extruder assembly. The sensor assembly consists of two idler bearings, which ride on the outer surface of the filament. As the filament is pulled through the sensor, variations in diameter cause the tensioning bearing to move. These movements are mechanically amplified by the class-3 lever and cause a magnet at the end of the lever to move in relation to a statically mounted hall effect sensor. The hall effect sensor measures the magnitude of the local magnetic field, outputting it as a voltage signal. The signals are then processed using a calibration algorithm and converted into diameter readings.

1.3.3 Validation and testing of TMAG5273 Sensor

The original InFiDEL diameter sensor used in prior work incorporated an SS495A analog Hall-effect sensor. While this configuration provided adequate performance for proof-of-concept experiments, the expanded scope of the present study required improved measurement resolution, digital signal stability, and temperature compensation. For this reason, the SS495A was replaced with the TMAG5273, a 3-axis digital Hall-effect sensor with integrated 16-bit analog-to-digital conversion (ADC) and on-chip temperature compensation.

Figure 2-Real time view of the FFW system

To evaluate the suitability of the TMAG5273 for high-resolution filament diameter sensing, a combination of simulation-based and analytical validation was performed.

1.3.3.1 Magnetic Field Response and Temperature Stability

The TMAG5273 sensor was evaluated using Texas Instruments' Magnetic Sensor Simulation Tool. The simulations examined the sensor's output response under varying magnetic field strength, temperature, and supply voltage conditions.

The sensor does not output diameter directly; rather, it measures magnetic field intensity (in millitesla, mT), which is generated by a small permanent magnet attached to the tensioning lever of the mechanical amplification system. As filament diameter changes, the lever position changes, altering the magnet-to-sensor distance and therefore the measured magnetic field.

Temperature simulations were conducted to evaluate signal drift across the expected laboratory operating range. Two models were compared:

- Sensor output with internal temperature compensation enabled (Fig. 3)
- Sensor output without temperature compensation (Fig .4)

Results showed that without compensation, the magnetic field reading shifted measurably across temperature variation. With compensation enabled, the output remained significantly more stable, indicating that the built-in correction algorithm effectively mitigates thermal drift.

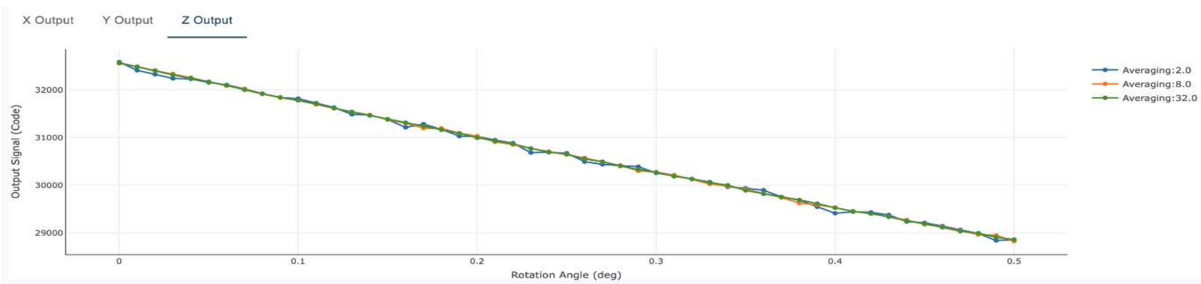

Figure 4-TMAG 5273 With Temperature Compensation

This is critical because uncorrected temperature-induced magnetic drift would appear as false filament diameter variation, reducing measurement fidelity during long print durations.

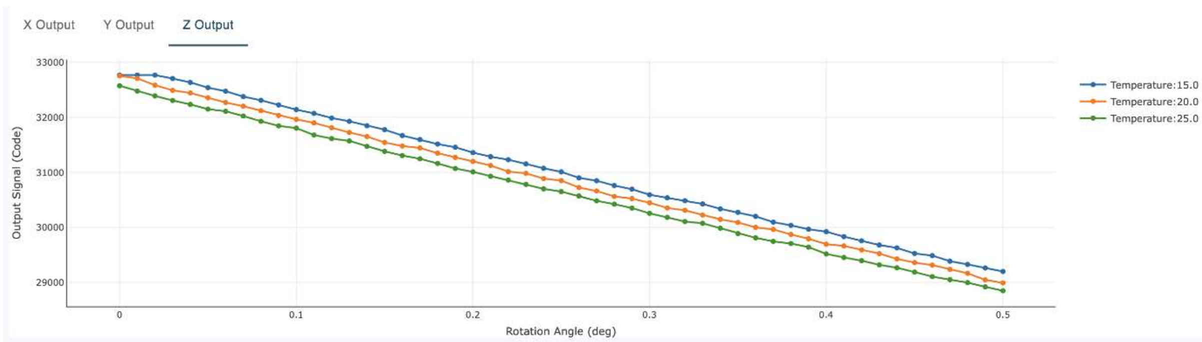

Figure 3-TMAG 5273 Without Temperature Compensation

1.3.3.2 Effect of Supply Voltage Variation

In addition to temperature stability, the TMAG5273 sensor was evaluated for sensitivity to supply voltage variation using Texas Instruments' Magnetic Sensor Simulation Tool. This analysis was performed because voltage fluctuations can introduce measurement drift in Hall-effect sensing systems, particularly when analog-output sensors are used in electrically noisy environments such as printer control systems.

For comparison purposes, an analog-output Hall-effect sensor (Texas Instruments DRV5055) was also simulated under varying supply voltage conditions. The DRV5055 represents a conventional analog Hall sensor architecture in which output voltage is directly proportional to both magnetic field strength and supply voltage. This comparison was performed to illustrate the susceptibility of analog sensors to supply voltage fluctuations relative to the digitally compensated TMAG5273. The DRV5055 was not used in the experimental printer system; it was included solely as a reference for evaluating voltage sensitivity.

The TMAG5273 exhibited minimal output variation with changing supply voltage, particularly when operated with its internal ADC and digital output architecture. Increasing the oversampling from 2× to 16× further improved signal stability by reducing noise and smoothing small fluctuations in the output (Fig. 5 & Fig. 6). This indicates that the TMAG5273 is relatively insensitive to moderate supply voltage variation and is therefore well suited for use in embedded printer environments where small electrical fluctuations may occur.

In contrast, the analog-output DRV5055 showed a stronger dependence of output on supply voltage (Fig. 7). Because analog Hall-effect sensors produce a voltage proportional to the sensed magnetic field, any change in the supply voltage can directly influence the sensor output and appear as a false change in magnetic field strength. In the context of filament diameter sensing, this would translate into an apparent diameter fluctuation even when the filament geometry remains unchanged.

This comparison highlights an important advantage of the TMAG5273 for the present application. Its digital output architecture reduces susceptibility to supply-voltage-induced measurement drift, improving the reliability of diameter estimation during long-duration prints. For a feed forward control system, this is important because false diameter readings could result in unnecessary correction commands to the extruder, thereby reducing compensation accuracy. Overall, the voltage variation analysis, together with the temperature compensation analysis, supports the selection of the TMAG5273 as a more stable sensing element than analog Hall-effect alternatives for real-time diameter monitoring.

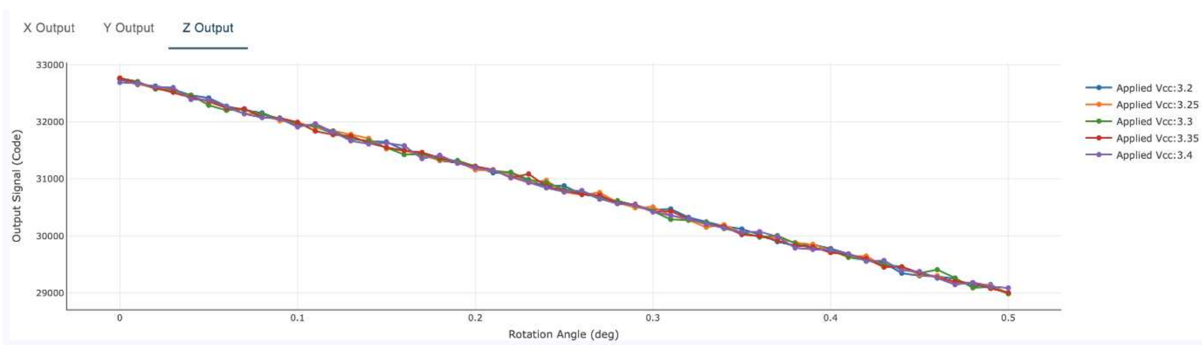

Figure 5-TMAG 5273 With Built in ADC and Varied input Voltage 2x sampling

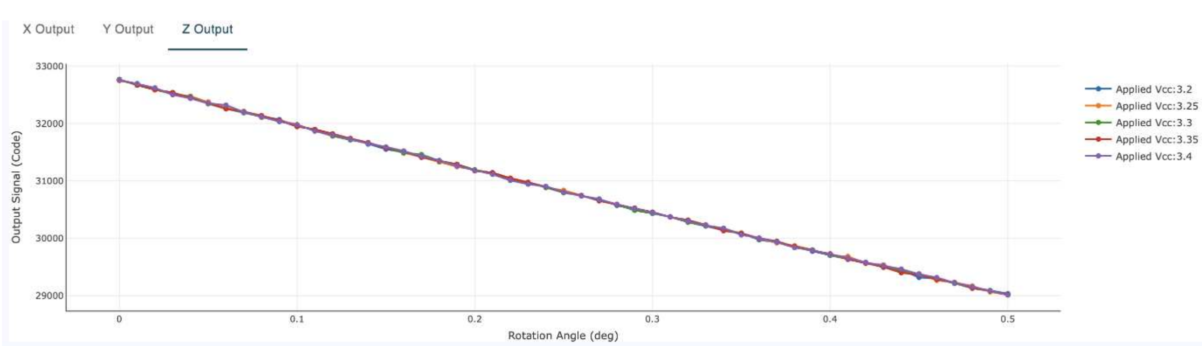

Figure 6-TMAG 5273 With Built in ADC and Varied input Voltage 16x sampling

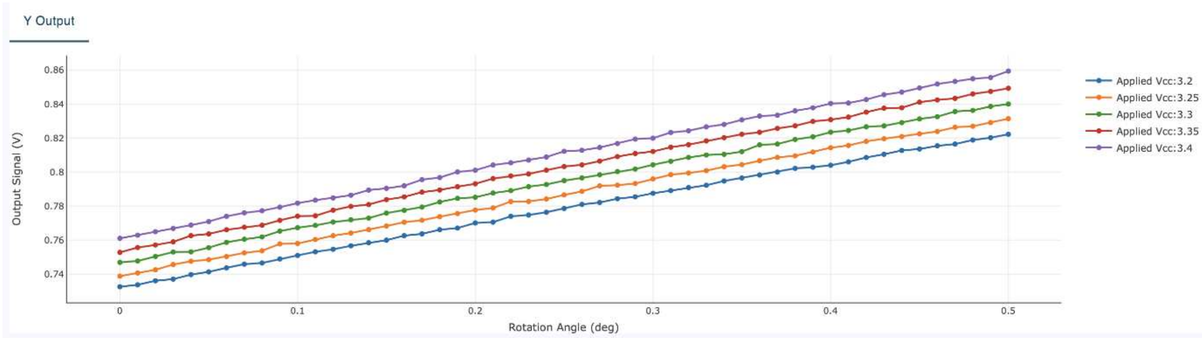

Figure 7-Analog Output Sensor (DRV5055) and Varied input Voltage

1.3.3.3 ADC Resolution and Magnetic Sensitivity

The TMAG5273 provides a 16-bit digital output over its configured magnetic measurement range. In the selected configuration (±40 mT full-scale range), the theoretical magnetic resolution is:

$$\frac{80\ \text{mT}}{2^{16}} \approx 0.0012\ \text{mT per LSB}$$

TMAG5273 contains an internal analog to digital converter (ADC) which transforms the measured magnetic field into a digital numerical value. The ADC has 16-bit resolution, meaning the magnetic measurement range is divided into 2^{16} discrete levels. The smallest detectable increment in digital output corresponds to one least significant bit.

By comparison, the previously used SS495A analog sensor provided approximately 0.0327 mT resolution when digitized with a 12-bit ADC. Thus, the TMAG5273 improves magnetic resolution by more than an order of magnitude.

However, magnetic resolution alone does not determine filament diameter resolution. The mechanical amplification system converts small lever displacements into amplified magnetic displacement at the sensor. The combined magnetic sensitivity and mechanical gain determine effective diameter resolution.

1.3.3.4 Theoretical Diameter Resolution

Using the calibrated relationship between magnetic field change and lever displacement, and between lever displacement and filament diameter change, the effective diameter resolution was estimated.

Under ideal conditions (noise-free signal, stable voltage, no magnet hysteresis), the theoretical diameter resolution improved from approximately 0.0011 mm (previous system) to approximately 0.000033 mm (33 nm) when using the TMAG5273 with mechanical amplification. This theoretical value represents the minimum detectable change based solely on analog-to-digital converter (ADC) limits and mechanical gain.

1.3.3.5 Practical Resolution, Sampling Rate, and Noise Considerations

While the preceding analysis establishes the minimum detectable diameter increment under ideal digital and mechanical gain assumptions, practical system performance is influenced by additional mechanical and electrical noise sources.

In practice, the smallest reliably distinguishable diameter change is larger than the ideal LSB value due to noise and mechanical effects.

During operation, measurement variability arises from:

- Minor magnetic field non-uniformity
- Mechanical vibration of the filament path
- Lever dynamics
- Electrical noise within the embedded system

These effects introduce small variations in successive measurements even when the filament geometry is constant. Therefore, the effective repeatable resolution is governed by overall system stability rather than by ADC alone.

Importantly, the digital resolution of the TMAG5273 is several orders of magnitude smaller than typical commercial filament diameter tolerances (±0.05 mm). This ensures that sensors do not limit the ability to detect meaningful geometric variation during printing. Instead, system performance is dominated by actual filament variability.

1.3.3.6 Sampling Rate and Oversampling

The sensor conversion timing also determines how frequently diameter measurements can be obtained. According to the device timing specifications, the base magnetic conversion time for a single-axis measurement is approximately 25 μs.

When oversampling is enabled, the sensor internally averages multiple magnetic conversions before reporting a value. With 16× oversampling, the effective conversion time increases proportionally:

$$t_{conv} = 25\,\mu s \times 16 = 400\,\mu s$$

The maximum theoretical sampling frequency is therefore the inverse of the conversion time:

$$f_s = \frac{1}{400 \times 10^{-6}} \approx 2500 \text{ samples per second}$$

Accounting for communication and firmware processing overhead, the sustained sampling rate in the implemented system is approximately:

$$f_s \approx 2.4 \text{ kS/s}$$

This sampling frequency is substantially higher than the dynamic rate at which filament diameter varies during extrusion. For typical printing speeds, this corresponds to multiple diameter measurements per millimeter of filament travel, ensuring that localized geometric fluctuations are captured with adequate temporal resolution.

1.3.3.7 Relevance to Filament Tolerances

It is important to emphasize that the objective of this sensing architecture is not nanometer scale metrology, but reliable detection of filament diameter fluctuations relative to nominal commercial tolerances (±0.05 mm). Because the validated practical resolution is several orders of magnitude smaller than typical manufacturing variation, sensor discretization and sampling rate do not limit the feed forward compensation strategy.

1.3.4 KIAUH: Klipper Installation and Update Helper

In the context of additive manufacturing, particularly desktop MEX printing, open-source firmware platforms such as Klipper have become increasingly popular due to their flexibility, performance, and community support. However, the process of installing and configuring Klipper along with essential companion software like user interfaces can be complex, especially for users without deep technical expertise. To address this, a command-line tool named KIAUH (Klipper Installation And Update Helper) has been developed to streamline and automate the setup process.

KIAUH is an interactive BASH script that enables users to install, manage, and update Klipper firmware and related software components on Linux-based single-board computers, such as the Raspberry Pi. It supports the installation of Klipper itself, along with associated services like Moonraker (an HTTP API server for Klipper), Fluidd and Mainsail (web-based user interfaces), Obico (remote monitoring and control), and KlipperScreen (touchscreen interface). The script provides an intuitive menu-driven interface that allows users to select installation and configuration options without needing to execute multiple individual commands manually.

KIAUH is particularly well-suited for experimental and research environments where rapid deployment and reproducibility of printer configurations are essential. It enables reproducible setups by handling all dependencies, software updates, and service management through a single interface. Additionally, it offers features for managing multiple printer instances, performing backups, and integrating third-party tools such as mobile monitoring platforms and enhanced visualizations like PrettyGCode.

KIAUH is designed to run on Debian-based distributions (e.g., Raspberry Pi OS, Ubuntu), and it is widely used in the hobbyist and research 3D printing communities due to its simplicity and reliability. The KIAUH script can be installed by cloning the GitHub repository and executing the shell script, which launches an interactive setup wizard. It assumes that the operating system has been pre-configured with network access and SSH capability.

KIAUH plays a critical role in this project by enabling the rapid deployment of a Klipper-based firmware environment on a Raspberry Pi, which was then integrated with custom monitoring and control systems for evaluating print reliability and process variability in material extrusion additive manufacturing. Its modular and open-source nature also allowed for the incorporation of additional tools and logging capabilities necessary for experimental data collection and analysis.

1.3.5 Pressure Tube Leak Testing Methodology

1.3.5.1 Rationale for Pressure-Based Evaluation

The objective of the pressure tube test was to quantify how filament geometric variability influences structural continuity and sealing integrity in melt-extruded parts. While tensile testing evaluates tensile strength under axial loading, it is less sensitive to localized interlayer discontinuities. In contrast, pressure retention testing is highly sensitive to micro voids, and interlayer gaps that form preferential leakage pathways[20].

Printed hollow cylindrical tubes were selected as test specimens because they:

- Amplify the effect of small volumetric deficits.
- Allow non-destructive quantitative evaluation.
- Isolate sealing integrity from tensile failure modes.

1.3.5.2 Apparatus Development and Sealing Method Evolution

To achieve the objectives of this study, three Prusa i3 MK3S+ 3D printers were employed, each operated using Klipper firmware. Two of the printers were dedicated to producing pressure test

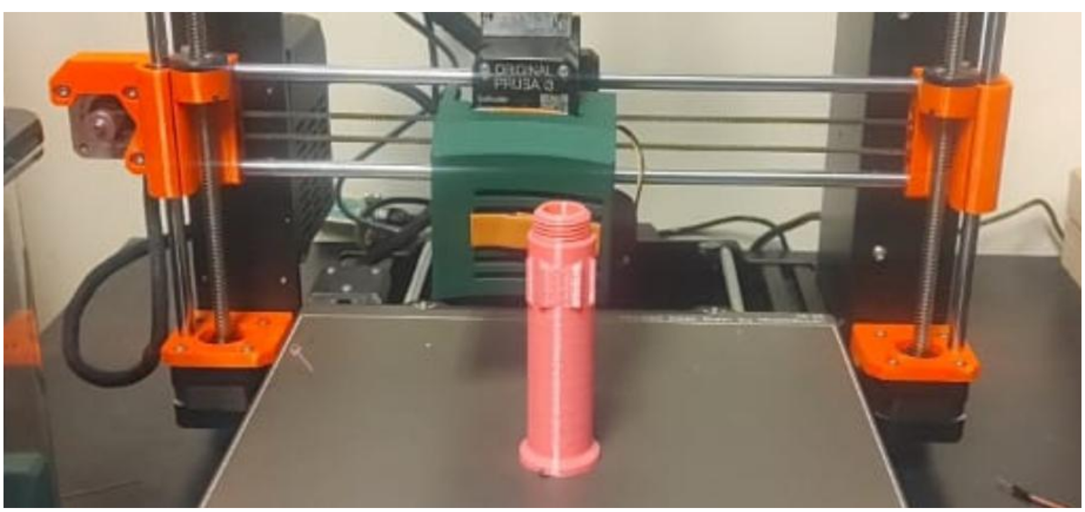

Figure 8-Ram head to push the coupon out after printing

coupons, while the third was used exclusively for tensile test coupons. All printers were managed through the Mainsail web interface under the custom Chrome profile.

Printing operations were fully automated, featuring a ram mechanism to eject the tube once a print was completed. The only required manual intervention was filament replacement within the dry boxes within which they were stored and used. Purge lines were programmed in G-code to print one layer above the previous purge line, preventing overlap between successive lines.

During the initial pressure testing phase, the pressure tube was inserted into a pipe after applying a lubricated layer around its surface. While this lubrication was sufficient for testing, the system exhibited considerable variation. The connected PTFE tubing contained kinks, which may have affected airflow, and because it was an older tube, there was also a possibility of undetected leaks influencing the test results. A new design and workflow were developed to mitigate this risk.

The idea was to make the system as leak proof as possible and eliminate the need for applying lubricant around the tube before testing it out.

To ensure repeatable and reliable pressure testing, the tube design and sealing interface were developed iteratively to satisfy several functional requirements. The tubes needed to integrate seamlessly with the testing apparatus, withstand routine handling without structural damage, and maintain internal pressure for a minimum duration of 25–30 minutes under test conditions. Additionally, the design was required to achieve airtight sealing without the use of lubricants, as lubricants could introduce variability in sealing performance and potentially confound leakage measurements.

An NPT male threaded interface was selected for the tube design to facilitate secure mounting and sealing. A 1/4-inch NPT thread was chosen over a 1/2-inch alternative due to its compatibility with available fittings.

Iteration 1

The initial iteration was developed to determine an appropriate thread depth for secure attachment to the testing apparatus and to identify suitable grip locations for tightening. Early prototypes demonstrated that insufficient thread engagement resulted in poor sealing reliability, while excessive engagement increased the risk of cracking during installation due to hoop stress concentration near the threaded region.

Grip placement was also evaluated to ensure that tightening torque could be applied without inducing local stress concentrations that led to fracture. From this iteration, an optimal thread depth and preliminary grip location were identified that provided sufficient tightness without structural failure.

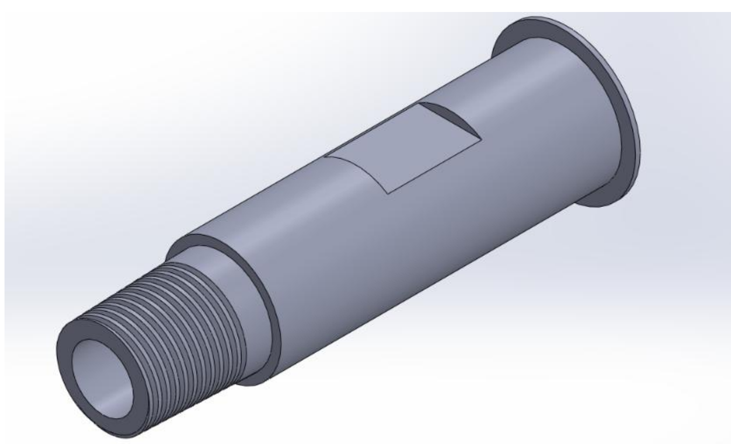

Figure 9-Iteration 1

Iteration 2

The second iteration incorporated the optimized thread depth and grip placement identified in Iteration 1. This configuration improved mechanical stability during tightening and reduced the likelihood of part breakage.

However, the internal cavity terminated in a flat base. During pressure testing, this geometry produced higher observed decay rates relative to later iterations. While the flat base provided a uniform internal surface, it created a sharp transition at the wall–base junction that increased stress concentration and may have facilitated localized leakage pathways at the bottom interface. This observation motivated further refinement of internal geometry.

Figure 10-Iteration 2

Iteration 3 (Final Configuration)

The hemispherical base eliminated the sharp corner at the wall–base junction present in earlier designs. From a design perspective, this modification reduced stress concentration and improved continuity of the internal surface. The smoother geometric transition reduced localized structural discontinuities that could act as leakage sites.

Additionally, the revised grip geometry improved torque distribution during installation, reducing the likelihood of crack initiation near the threaded interface.

The final geometry, shown in the attached drawings and sectional view, demonstrated improved mechanical durability and more consistent pressure retention during validation testing. This configuration was therefore adopted for all subsequent experimental trials.

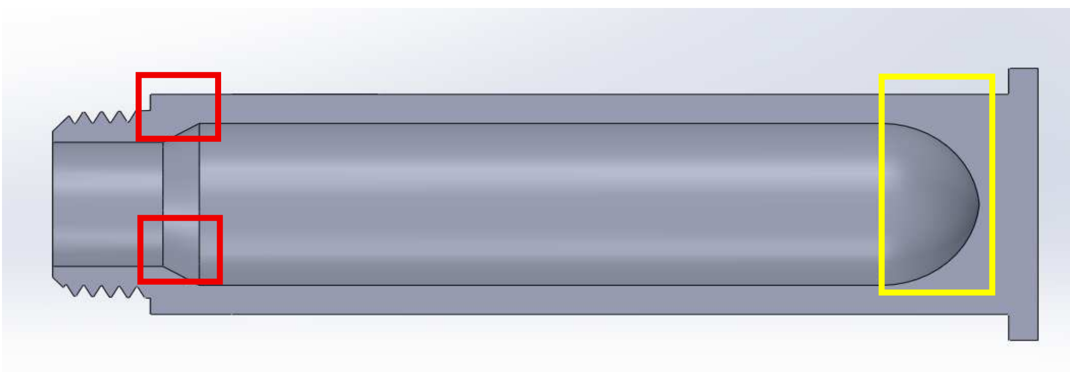

Figure 11-Iteration 3

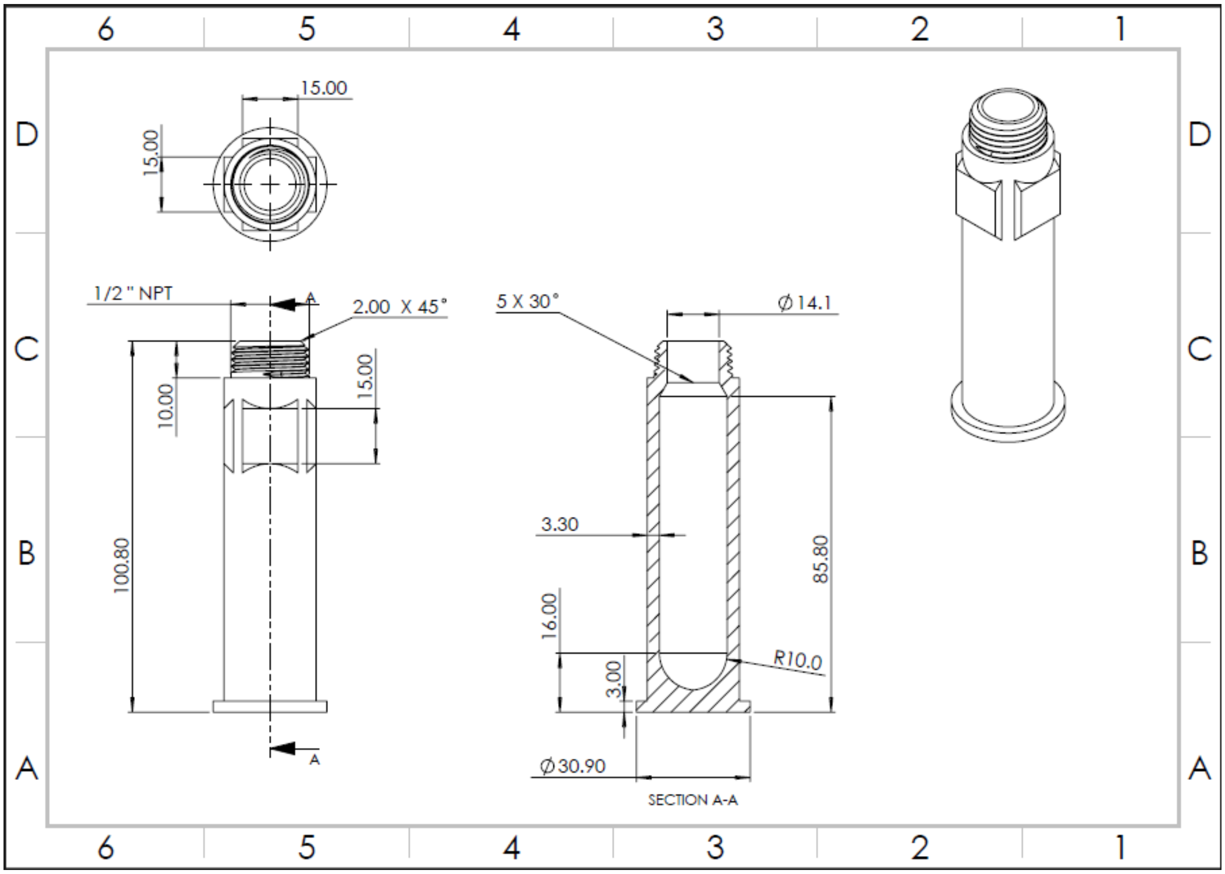

Figure 12- Pressure tube final iteration

1.3.5.3 Leak Detection and Validation Procedures

Two independent methods were used to verify that pressure decay originated from the printed tube walls rather than from the apparatus interface.

Fixture Validation

Method 1: Soap Solution Leak Check

The first leak-checking method was a qualitative soap-solution test used to identify leakage at threaded interfaces and other external connections in the pressure testing apparatus. A soap solution was drawn into a syringe and applied to all locations with thread engagement while the system was pressurized.

The compressor was initially charged to approximately 35 psi, and the downstream regulator was used to reduce the test pressure to 1 psi. Once the system reached 1 psi, the air supply was shut off, and all joints were observed for bubble formation. The appearance of bubbles indicated the presence of leakage at the corresponding interface.

If leakage was detected, the threaded connection was tightened further, and additional Teflon tape was applied as needed. The procedure was then repeated until no visible bubbles formed. This method provided a rapid and effective means of identifying gross external leaks before conducting quantitative pressure decay measurements.

Method 2: Brass Plug Test

The second leak-checking method involved using a standard brass plug of matching thread specification. This configuration allowed the threaded interface and associated fittings to be evaluated independently of the printed tube geometry.

With the brass plug installed, the system was pressurized to 1 psi using the regulated air supply and then isolated in the same manner as during tube testing. Pressure was monitored over time to assess any decay attributable solely to the fixture and threaded connections.

Because the brass plug does not contain an internal cavity and provides a rigid, machined sealing surface, any measurable pressure loss under this condition would indicate leakage within the apparatus rather than through a printed tube. Observed decay under the brass-plug configuration was negligible compared to decay measured in printed tubes, confirming that fixture leakage was not a dominant contributor to experimental results.

Pressure tubes threaded Interface Investigation

After 45 pressure tube tests had been conducted, consistent pressure decay raised concern that a portion of the measured leakage might be attributable to threaded interface imperfections rather than exclusively to wall defects within the printed tube. Although preliminary soap-solution testing and brass-plug validation suggested minimal fixture leakage, the possibility of thread-induced microleakage under extended test durations warranted further investigation.

To evaluate the influence of thread sealing conditions on pressure retention, four alternative printed plug configurations were fabricated (Figures 13–16). Each configuration maintained the same nominal thread geometry but varied the location and application of lubricant intended to improve sealing performance.

- Plug 1- Hollow Plug with External Thread Lubrication
- Plug 2- Solid Plug with External Thread Lubrication
- Plug 3- Hollow Plug with Internal Bore Lubrication
- Plug 4- Hollow Plug with Dual Surface Lubrication

All tests were conducted at 1 psi internal pressure using the standard decay protocol described previously. In the plots shown in Figures 13–16, the horizontal axis labeled "X_Value" represents time as recorded by LabVIEW during data acquisition.

For Plug 1 (Figure 13), measurable variability in decay behavior was observed across the five trial runs. Although all trials reached similar peak pressures, the subsequent decay slopes diverged significantly. Four runs exhibited relatively rapid exponential decay, while one run demonstrated substantially slower decay extending over a longer duration.

Plug 2 (Figure 14) demonstrated tightly clustered decay curves across all five trials. The decay slopes were shallow and closely aligned, indicating improved pressure retention and strong repeatability under standardized tightening conditions. No catastrophic early pressure loss was observed, and divergence between runs was minimal.

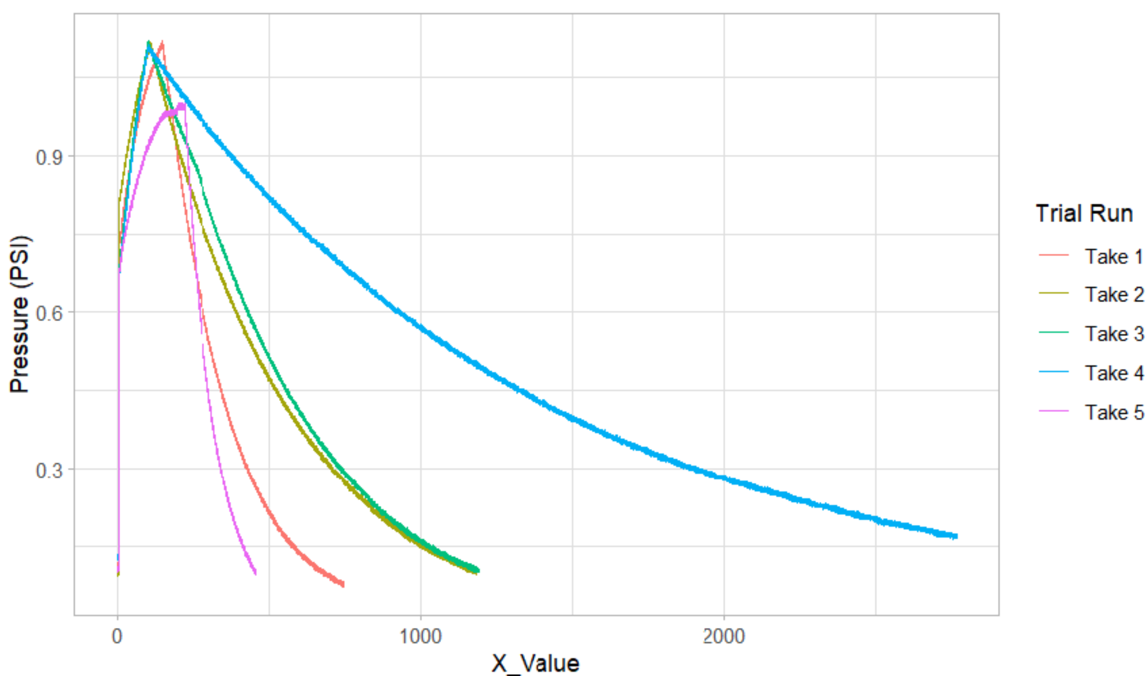

Figure 13-Plug 1

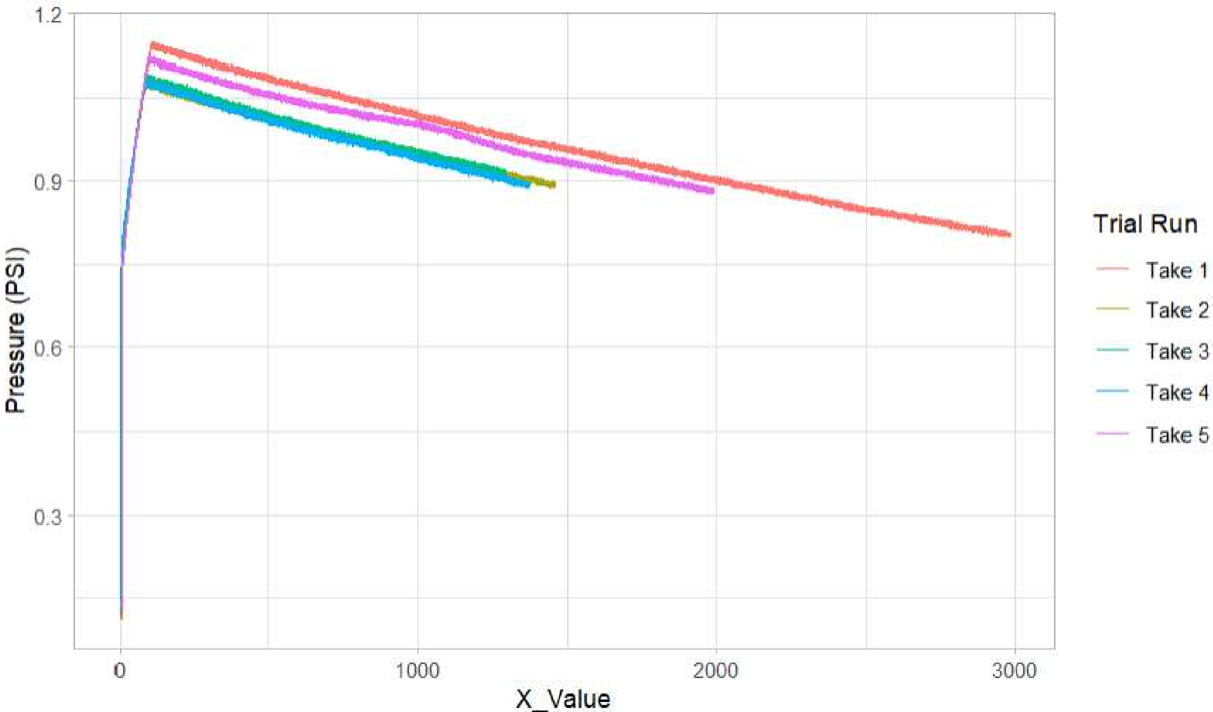

Figure 14-Plug 2

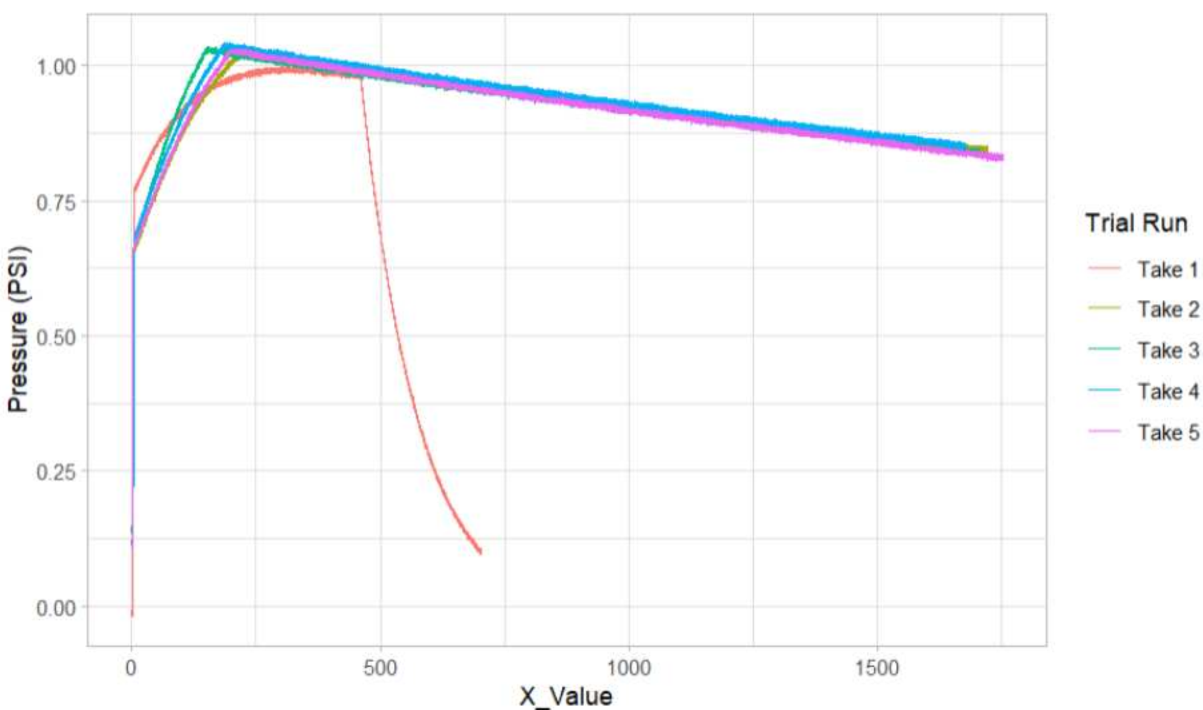

Figure 15-Plug 3

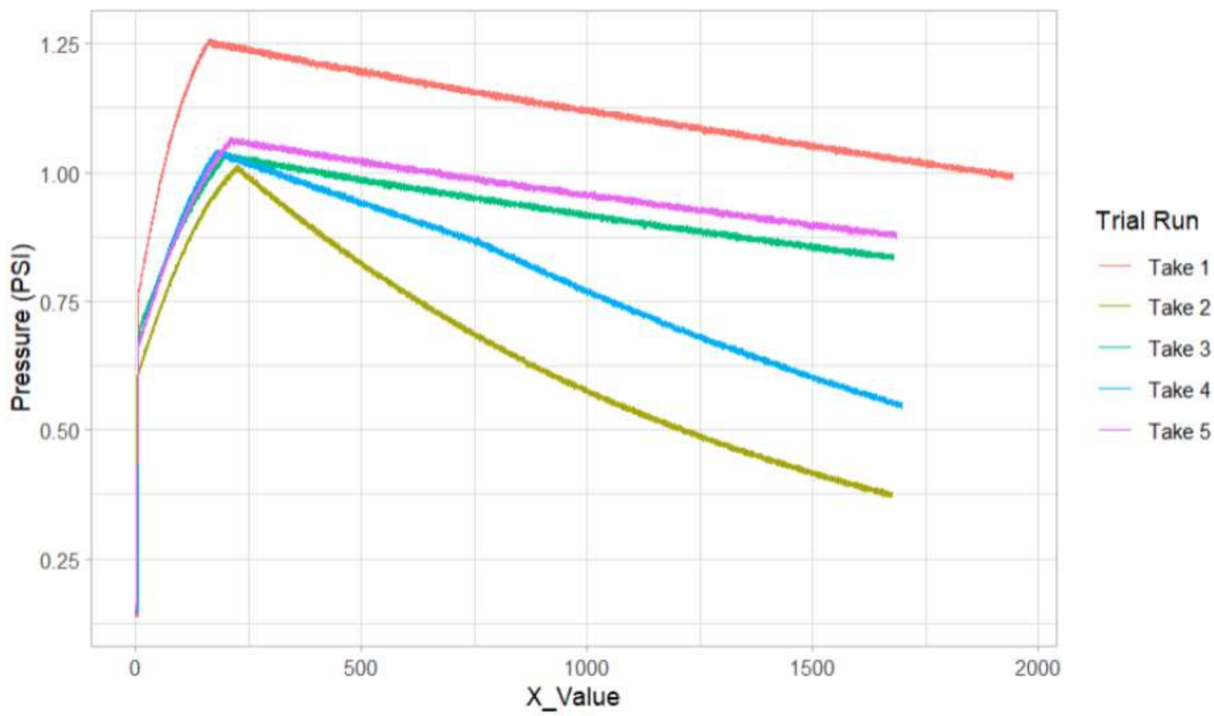

Figure 16-Plug 4

Plug 3 (Figure 15) exhibited consistent decay behavior in four of the five trials, with closely clustered and gradual pressure reduction over time. However, one trial showed abrupt pressure loss, indicating of incomplete sealing or installation variability. Excluding this anomalous run, plug 3 demonstrated stable and repeatable sealing performance.

Plug 4 (Figure 16) displayed noticeable variability in decay slopes among trials. While catastrophic failure was not observed, the spread in decay magnitude suggests sensitivity to tightening conditions and interface contact variability. One trial exhibited relatively strong retention, whereas others decayed more rapidly, indicating reduced repeatability compared to Plug 2.

Overall, the comparison confirmed that threaded sealing condition influences low-pressure retention behavior. Although certain configurations demonstrated marginal improvements in isolated trials, plug 1 was retained for continued use in the study. At the time of this investigation, a substantial portion of the experimental dataset had already been collected using Plug 1. Introducing a different plug configuration mid-study would have introduced a confounding variable into the dataset.

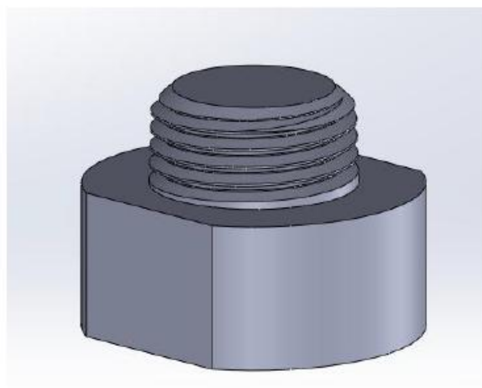

Figure 17-Solid Plug

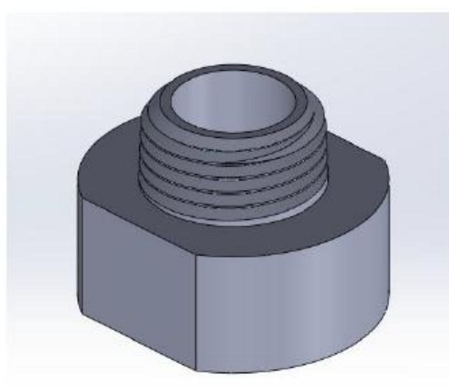

Figure 18-Hollow plug

1.4 Printing the Pressure tube:

Each printing session began with filament loading after cutting at a 45° angle. The extruder and bed were preheated to 230 °C and 85 °C, respectively. The FFC setting was toggled under Mainsail Macros depending on the test configuration. Data logging was initiated using ./data_logger.sh in Termius, with metadata entered including printer number, vendor, print type (Tube or Coupon), closed-loop status, and trial number. For pressure tubes, the Pressure_Tube_Final.gcode file was selected.

After printing, the tubes were weighed to the nearest milligram, recorded, individually bagged, labeled, and stored in a dry box.

1.5 Downloading Print Data

Print logs were downloaded from the printer via File Explorer (This PC > Klipper_Logs > complete) and uploaded to Microsoft Teams for archival.

1.6 Pressure Testing

The pressure testing procedure was aimed at quantifying pressure decay in the printed tubes. Testing was performed using a custom-built pressure decay apparatus regulated to reach 1.0 Psi. This pressure was controlled by a regulator with ±0.03 psi accuracy, while the input pressure from the compressor was adjusted to 25–50 psi.

Prior to mounting, a liberal amount of Molykote 111 lubricant (also referred to as “mocolyte 441”) was applied to the male NPT threads—especially the flat face—to ensure proper sealing. The tube was threaded into a matching female fitting until the flat face was flush and some lubricant oozed out. The valve was then opened slowly while data logging was initiated in LabVIEW, with a specified file path for saving output (tube_###.csv).

Once pressure reached 1 Psi, the valve was closed, and the pressure decay was monitored until it dropped to approximately 0.05–0.1 psi. Afterward, the tube was unscrewed, cleaned, packed in a zip bag, and labelled accordingly.

1.7 Tensile Coupons and Testing

To meet the objectives of this study, a Prusa i3 MK3S+ 3D printer was utilized, operated via Klipper firmware. The printer was controlled through the Mainsail web interface under a custom Chrome profile.

Tensile testing was performed using an Instron 68TM-10 Mechanical Tester [21], equipped with 5 kN manual wedge grips featuring wide V-jaw faces, mounted on a 10 kN load cell. The available grips could not clamp the standard ASTM D638[22] Type IV dog-bone tensile coupons as it kept slipping, even though the coupon dimensions were within the allowable size range. Consequently, a custom cylindrical tensile coupon was designed to ensure reliable gripping and consistent load transfer during testing.

To accommodate this, the custom coupon featured a 12 mm outer diameter (OD) clamping section and an 8 mm OD reduced section (Figure X). The coupons were printed vertically to evaluate interlayer bonding strength. A 100% infill density with a randomized Z-concentric infill pattern was used, while rectilinear patterns were avoided due to their tendency to produce lower tensile strength.

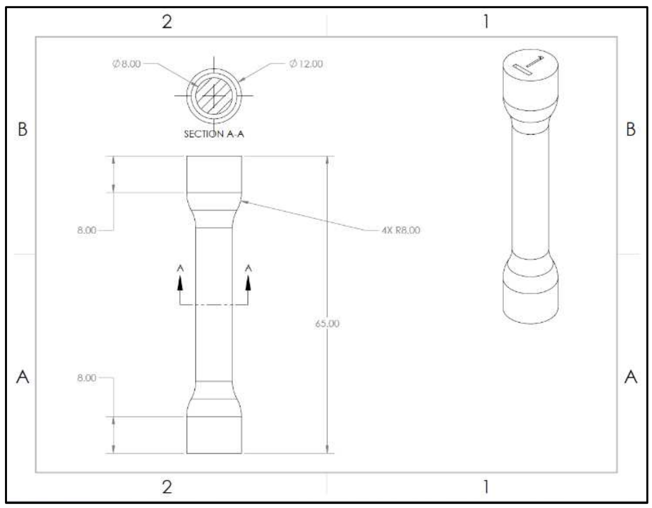

Figure 19-Tensile coupon Part Drawing

The coupon printing was not automated; it was decided to be printed manually as pushing out a coupon with a ram head may damage the coupon. Since printing 240 coupons manually would be a very time-consuming process, it was decided to print coupons in batches of 2 or 3 or 4 or 6. Printing of the coupons was conducted manually, as automated ejection using a ram mechanism risked damaging the printed parts. Given the need to fabricate 240 coupons, printing was performed in batches of 2, 3, 4, or 6 to improve efficiency.

Coupons were produced in varying batch sizes and positions on the build platform to determine the optimal configuration that minimizes print failures. The primary sources of failure were nozzle oozing during extruder travel between parts and filament drooling onto adjacent coupons, which caused collisions between the nozzle and printed components. The most reliable configuration yielding a 1 in 22 print failure rate consisted of a batch size of 4, arranged in a 100 × 100 mm square pattern, as illustrated below.

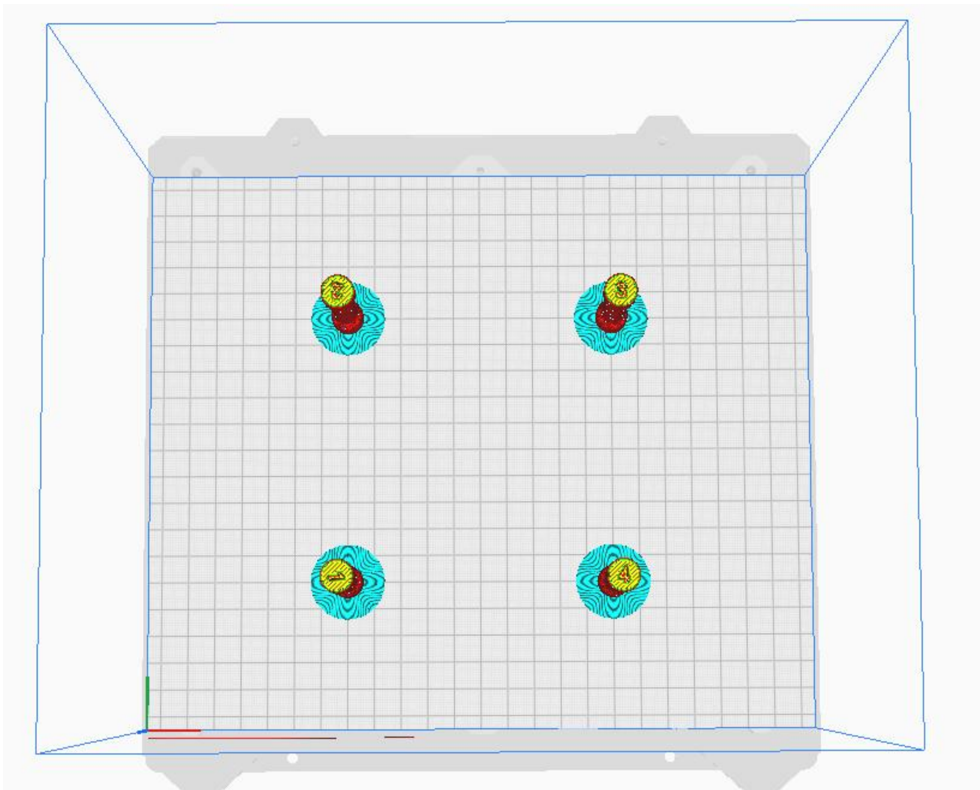

Figure 20-Tensile coupon print layout

1.8 Differential Scanning Calorimetry (DSC) Analysis

To investigate whether differences in bulk polymer thermal behavior could contribute to the observed variation in tensile performance between filament vendors, Differential Scanning Calorimetry (DSC) analysis was performed on a subset of filament models. DSC is a thermal analysis technique that measures the heat flow into or out of a material as it is subjected to a controlled temperature program, allowing identification of thermal transitions such as glass transition, crystallization, and melting events. These transitions can reveal differences in polymer composition, crystallinity, and the presence of additives or processing aids that may influence mechanical behavior during printing.

Prior to DSC analysis, complementary characterization methods including X-ray diffraction (XRD) and Fourier-transform infrared spectroscopy (FTIR) were also explored to assess polymeric composition differences between filament models. However, neither method yielded meaningful differentiation between the tested PETG filaments within the range of compositional variations expected across commercial vendors. DSC was therefore retained as the primary thermal characterization method for this study.

DSC measurements were conducted at the Analytical Resources Core (ARC) at Colorado State University [23] on filament samples taken directly from a subset of spoils prior to printing, following the facility's standard operating procedure for polymer characterization.

2 CHAPTER 2-RESULTS

2.1 Pressure tube printing and testing

Pressure decay rate and tube weight were selected as complementary performance indicators to evaluate the impact of filament geometry on printed part integrity. The pressure decay rate serves as a non-destructive measure of internal structural quality, reflecting the presence of micro voids, inter-layer bonding defects, and extrusion inconsistencies that permit air leakage under low internal pressure. A lower decay rate corresponds to improved airtightness and structural continuity.

Tube weight was analyzed as a measure of cumulative volumetric deposition. Because filament diameter directly affects volumetric flow rate during melt extrusion, deviations from nominal diameter result in systematic over- or under-extrusion. Together, these two metrics enable evaluation of whether FFC reduces geometry induced performance variability.

This section presents a comparative analysis of the filament models based on recorded filament diameter during pressure tube printing and relates these measurements to tube decay rate and tube weight. In addition to geometric measurements, key process parameters including extruder temperature, heater duty cycle, and ambient humidity were analyzed to ensure that observed differences in decay behavior were attributable to filament characteristics rather than uncontrolled thermal or environmental variation. These parameters were monitored to confirm process stability and to identify potential confounding influences on extrusion consistency.

For each filament model, 24 pressure tubes were printed and tested, with 12 produced on Printer 2 and 12 on Printer 3 to evaluate printer-level variation. Ranges of key printer parameters, including extruder temperature and heater duty cycle, are also presented.

Ambient temperature and humidity conditions during automated tube production are included in documenting the environmental conditions under which the prints were fabricated. All the results from the plots will be discussed in the "Discussion" chapter.

The following subsection summarizes the diameter data for each filament model:

2.1.1 Filament Diameter Distributions

Figure 21 presents statistical density estimates of filament diameter measurements for each filament model within the range of 1.65–1.85 mm. Each panel corresponds to a single filament model. The x-axis represents filament diameter (mm), and the y-axis represents statistical density. The curves illustrate the relative frequency distribution of diameter measurements collected during printing. The range of 1.65–1.85 mm was selected to encompass the full observed variation across all filament models while centering around the nominal diameter of 1.75 mm ± 0.05 mm. This range captures deviations exceeding typical manufacturing tolerance limits and ensures consistent scaling across all models for direct visual comparison.

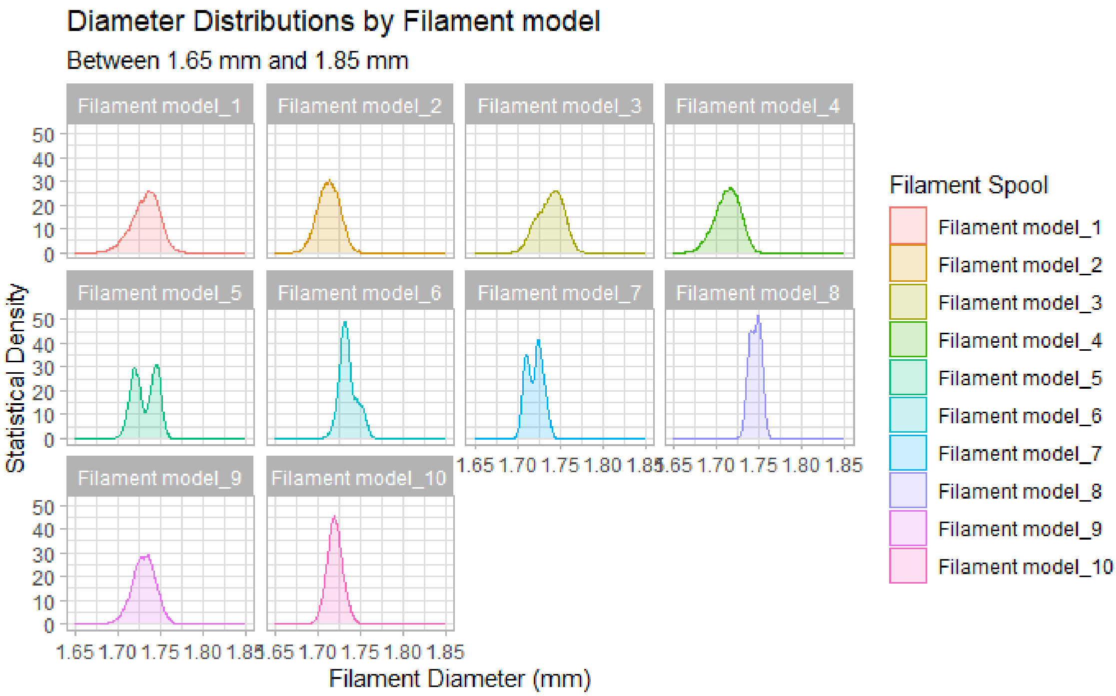

Figure 21-Diameter recordings in the 1.65 to 1.85mm range, by filament model

2.1.2 Diameter Distributions by Filament Model (Separated by Printer)

This figure below displays diameter distributions for each filament model, separated by printer. Within each panel, density curves from Printer 2 and Printer 3 are overlaid for comparison. The

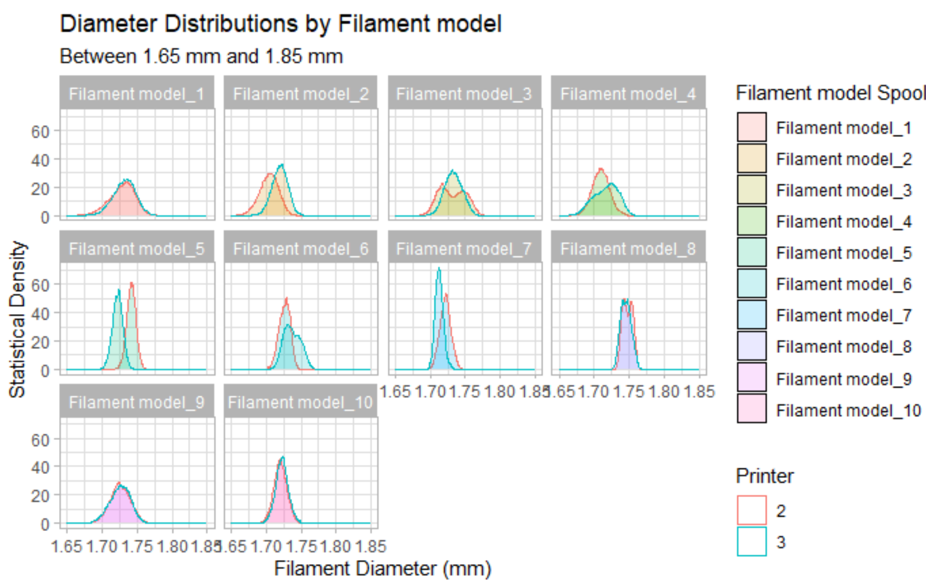

Figure 22-Diameter recordings in the 1.65 to 1.85mm range, by filament model and printer

x-axis represents filament diameter (mm), and the y-axis represents statistical density. The plot visualizes how diameter measurements are distributed for each filament model across printers.

2.2 Pressure tube decay results

The following subsection summarizes the decay rate of each filament model when its pressure tubes were subjected to 1 Psi, and the decay was measured via LabVIEW. The analysis also evaluates the influence of printer variability and Feed Forward Control (FFC) status (ON vs. OFF) on decay performance using box plots grouped by filament model. These box plots illustrate the distribution of pressure decay slopes for each filament model, highlighting both the median decay rate and the variability of the data. Variability is represented by the interquartile range (IQR) and the overall range of the measured slopes, allowing comparison of consistency between filament models, printers, and FFC conditions.

A scatter plot of tube weight versus pressure decay rate was developed to investigate whether tube weight correlates with pressure decay rate.

Finally, heat maps are presented to compare filament diameter distributions with both pressure decay rate and tube weight.

2.2.1 Pressure Decay Slope by Filament Model & FFC status

Figure 23 presents boxplots of pressure decay rate (slope of ln ()) for each filament model. The box represents the interquartile range (IQR), the center line indicates the median, whiskers extend to non-outlier limits, circular markers represent individual measurements, and diamond markers denote statistical outliers. The x-axis lists filament models, and the y-axis represents pressure decay rate.

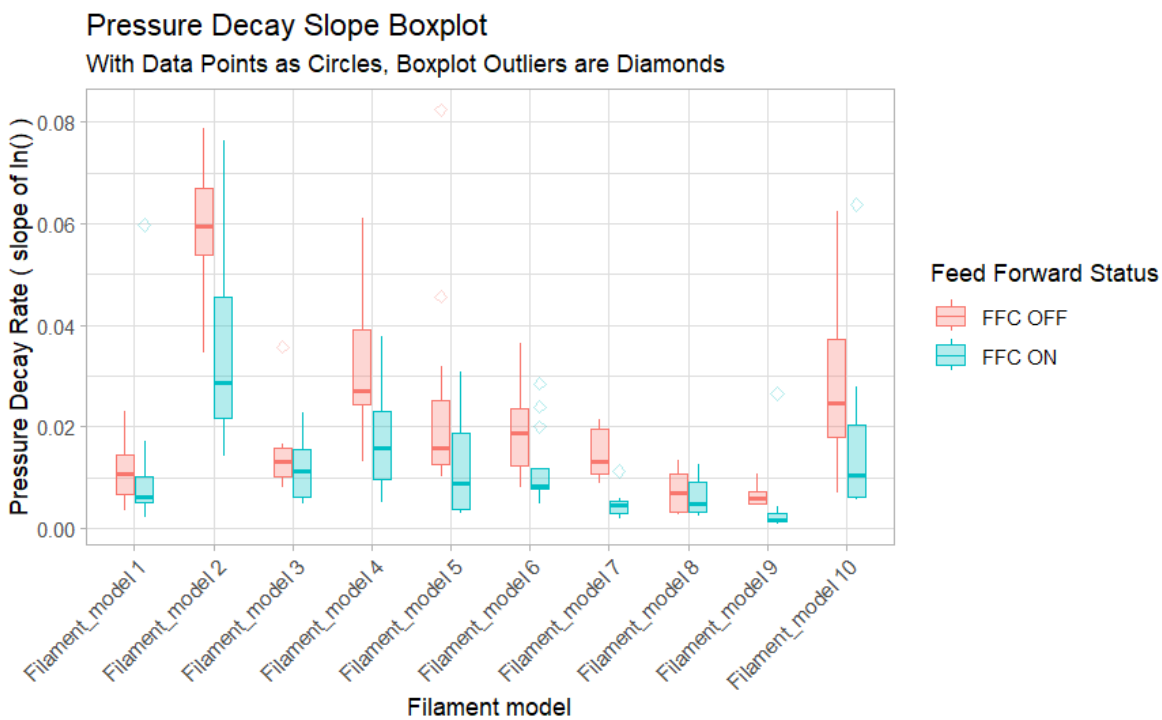

Figure 23-Decay rate vs filament models

Table 1- Decay rate of tubes by FFC & filament model

Filament model	FFC OFF Median (s^{-1})	FFC ON Median (s^{-1})
1	0.0108	0.00624
2	0.0595	0.0287
3	0.0131	0.0113
4	0.0269	0.0157
5	0.0159	0.00897
6	0.0187	0.00845
7	0.0131	0.00457
8	0.00709	0.00474
9	0.00590	0.00172
10	0.0246	0.0104

Table 2- p values from Wilcoxon test

Filament model	p value
1	0.10
2	0.001
3	0.40
4	0.01
5	0.03
6	0.01
7	0.00
8	0.26
9	0.000
10	0.02

Table 3- p values from ANOVA test

Filament model	p value
1	0.95
2	0.001
3	0.34
4	0.01
5	0.07
6	0.04
7	0.000
8	0.48
9	0.30
10	0.09

To statistically evaluate the effect of feed forward control (FFC) on pressure decay rate, both parametric (ANOVA) and non-parametric (Wilcoxon rank-sum) tests were performed for each filament model. The ANOVA results indicate that FFC has a statistically significant effect on pressure decay rate for filament models 2, 4, 6, and 7 ($p < 0.05$). The remaining filament models do not show statistically significant differences under the assumptions of normality. The Wilcoxon rank-sum test shows statistically significant improvements in pressure decay for filament models 2, 4, 5, 6, 7, 9, and 10. This test, which does not assume normality, identifies additional filament models where FFC improves performance.

Several filament models exhibited extreme outliers in pressure decay slope. For example, Filament 5 (FFC OFF) showed decay rates approaching 0.082 s^{-1}, nearly five times its median value. These high-slope events represent significantly accelerated leakage, suggesting localized structural defects or insufficient interlayer fusion[8], [24]. The presence of such outliers indicates that variability in filament geometry can occasionally produce catastrophic leakage behavior, even when median performance appears acceptable.

2.2.2 Tube Weight by Filament Model & FFC Status

Figure 24 presents tube weight distributions for each filament model, separated by FFC condition and printer. Boxplots summarize weight variation, and individual measurements are shown as points. The x-axis represents filament model, and the y-axis represents tube weight (g).

Table 4- Weight of tubes by FFC & filament model

Filament Model	FFC OFF Median(g)	FFC ON Median(g)
1	32.9	33.7
2	31.4	32.8
3	32.8	33.5
4	32.3	33.7
5	32.8	33.5
6	32.6	33.4
7	32.7	33.9
8	33.5	33.7
9	33.0	33.9
10	32.4	33.5

Table 5-p values from Wilcoxon test

Filament Model	p values
1	0.00
2	0.00
3	0.00
4	0.00
5	0.00
6	0.00
7	0.00
8	0.006
9	0.00
10	0.00

Table 6-p values from Anova test

Filament Model	p values
1	0.00
2	0.00
3	0.00
4	0.00
5	0.00
6	0.00
7	0.00
8	0.002
9	0.00
10	0.00

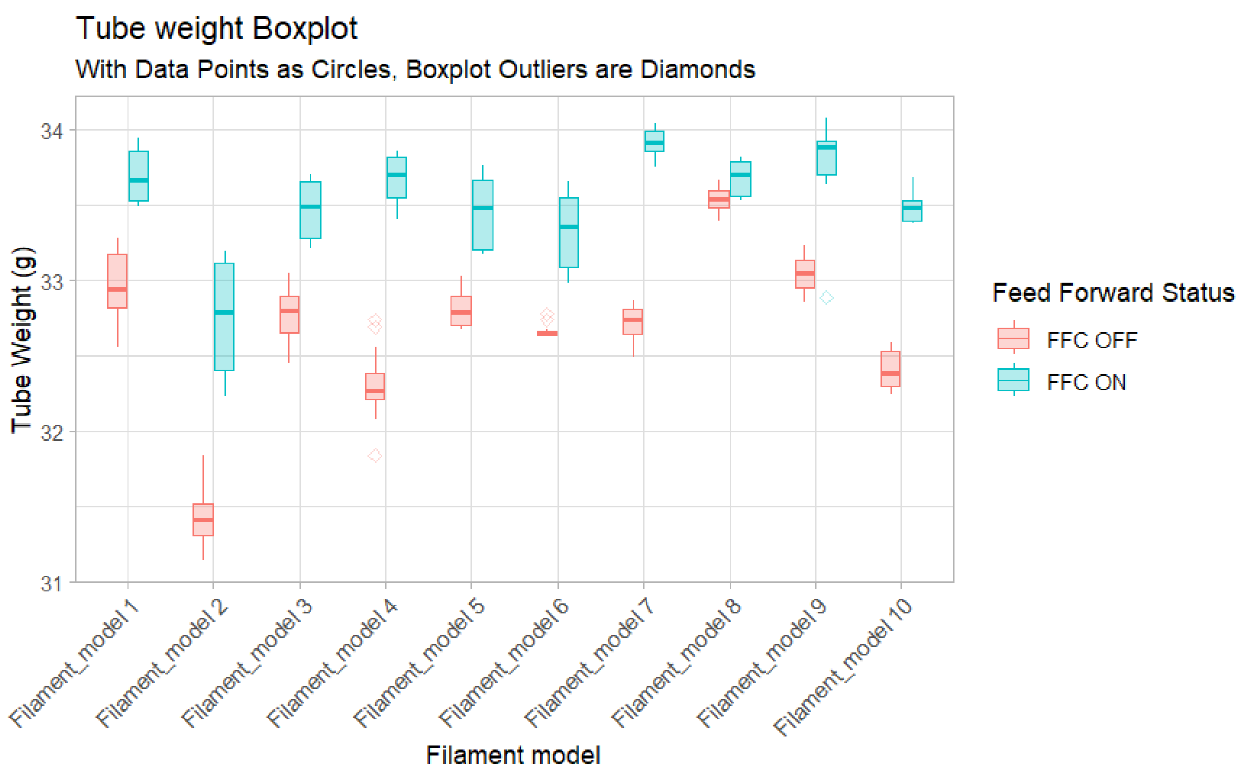

Figure 24-Tube Weight vs Filament models

The consistent weight increase under FFC ON conditions as seen from table 2 and figure 24 provides quantitative evidence that feed-forward correction improves mass delivery accuracy, thereby stabilizing wall thickness and reducing structural variability.

The effect of feed forward control (FFC) on pressure tube weight was evaluated across all filament models, as shown in Figure X. The results indicate a consistent increase in tube weight when FFC is enabled. This trend is observed across all filament models, with FFC ON samples showing higher median weights compared to FFC OFF. Statistical analysis further supports this observation, with both Wilcoxon rank-sum and ANOVA tests indicating statistically significant differences ($p < 0.05$) for all filament models. The increase in tube weight suggests that FFC compensates for under-extrusion caused by filament diameter variability, resulting in more consistent and complete material deposition.

2.2.3 Tube Weight vs Pressure decay rate

Figure 25 displays the relationship between tube weight (x-axis) and pressure decay rate (y-axis). Each point represents an individual tube, colored by filament model. The plot visualizes the distribution of observations across weight and decay rate values. The R value for the linear regression is -0.64 which shows there is a good correlation between tube weight and slope of pressure decay.

More about this will be discussed in the discussion chapter.

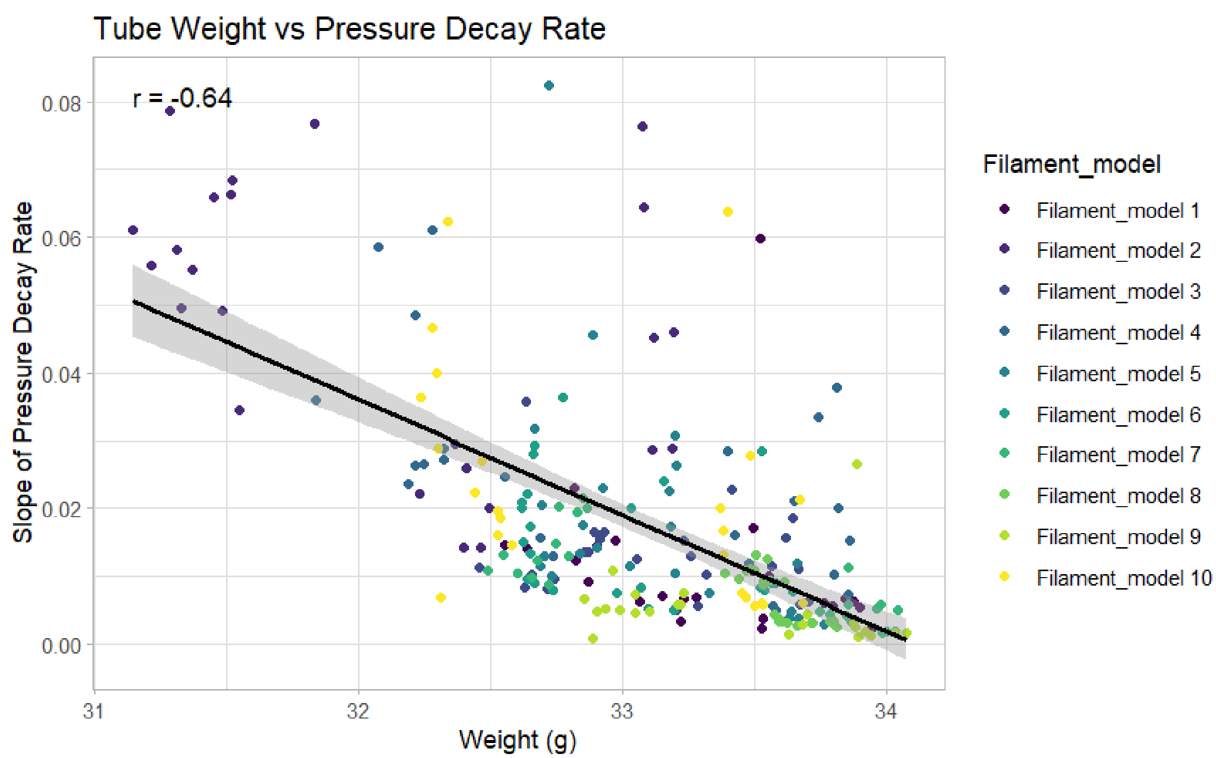

Figure 25- Scatter Plot depicting relationship between Decay rate and weight of tubes

2.2.4 Diameter binned by filament model ordered by pressure decay

The D1& D2 in the plots below mean “Diameter sensor 1” & “Diameter sensor 2” respectively. The heat map–style percentage matrix was used to present the distribution of filament diameter measurements across predefined diameter bins for each filament model. Six diameter bins were selected to provide sufficient resolution to identify clustering of measurements relative to the nominal 1.75 mm target while maintaining stable percentage representation within each bin. The primary objective to have 6 bins was to determine how measurements were distributed around the mean diameter and whether certain filament models exhibited systematic bias above or below nominal. This binning structure allows clear visualization of percentage concentration near the central bins while preserving consistency across all filament models for comparison. Color intensity represents the percentage of observations within a bin, allowing the distribution of measurements to be visualized compactly across all filament models. This format enables side-by-side comparison of binned diameter distributions for both diameter sensors (D1 and D2) while preserving the quantitative proportion of measurements in each range.

A working hypothesis of this analysis was that filament models with a higher percentage of measurements concentrated within the central bin(s) around 1.75 mm would exhibit improved part quality, reflected in higher tube weight consistency and reduced pressure decay rates. Since volumetric extrusion rate scales with the square of filament diameter, tighter clustering around nominal diameter was expected to reduce volumetric variability and improve structural integrity of printed tubes.

Figure 26 shows the percentage of diameter measurements falling within predefined diameter bins for each filament model. The left half represents Diameter Sensor 1 (D1), and the right half represents Diameter Sensor 2 (D2). Filament models are ordered by decay rate. Color intensity indicates the percentage of measurements within each diameter bin.

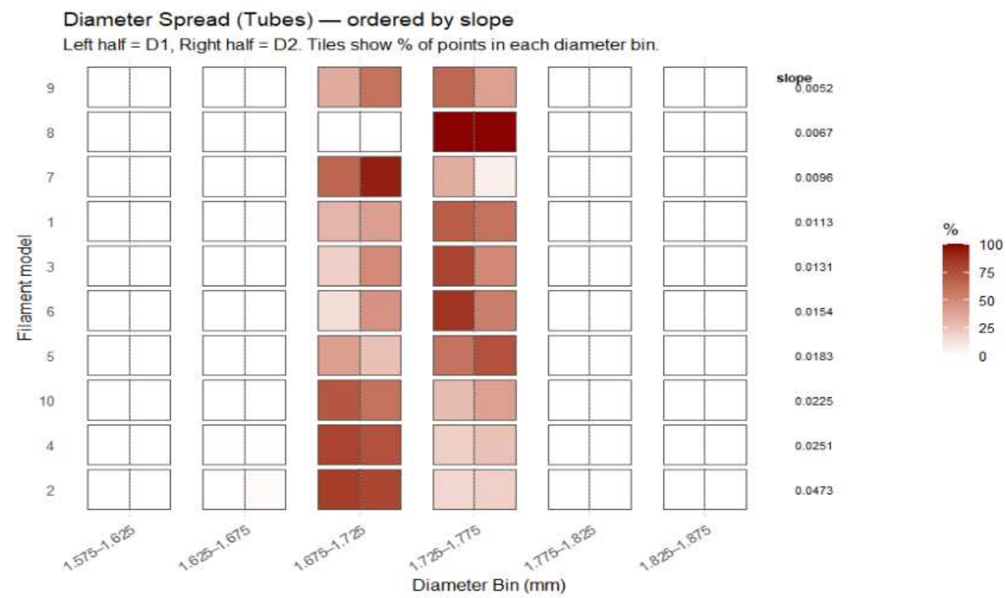

Figure 26-Heatmap of diameters by filament model ordered by mean decay rate

2.2.5 Diameter binned by filament model ordered by tube weight

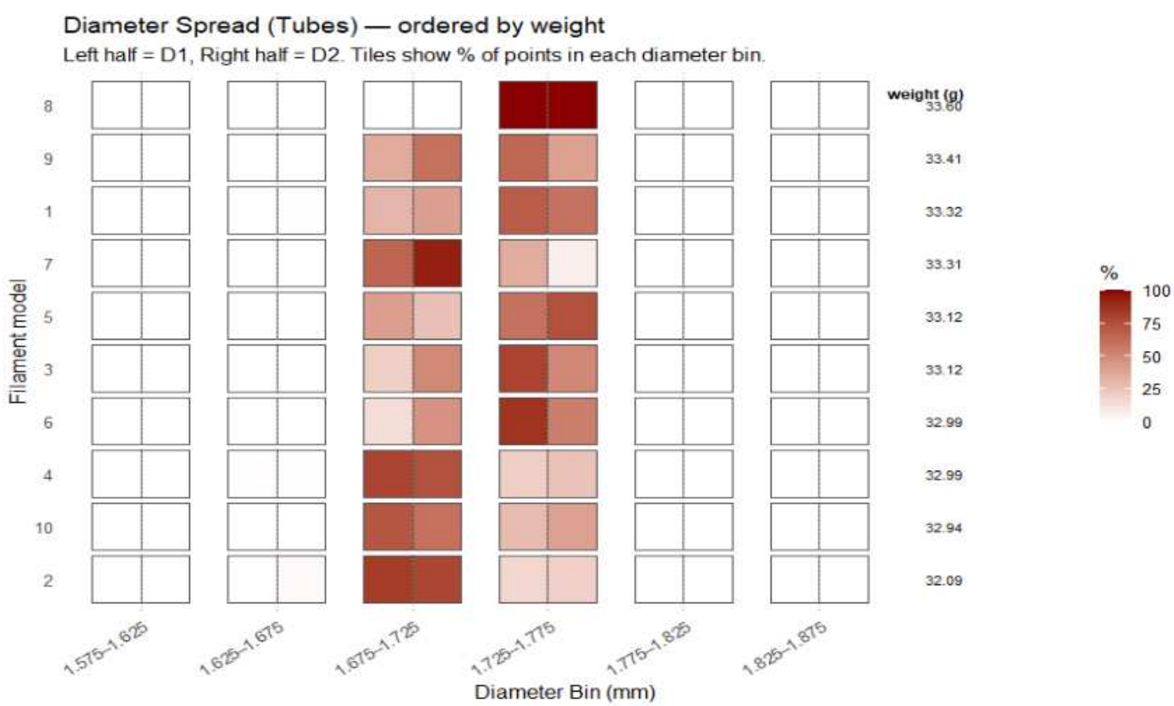

Figure 27-Heatmap of diameters by filament model ordered by mean Tube weight

Figure 27 presents the percentage distribution of diameter measurements within predefined bins for each filament model, separated into D1 and D2 sensor readings. Filament models are ordered by tube weight. Color shading represents the proportion of measurements within each bin.
The D1& D2 in the plots above mean “Diameter sensor 1” & “Diameter sensor 2” respectively.

2.3 Variation between printers, humidity, and temperature

The pressure tubes were printed using two different printers. While the primary motivation was to increase production throughput, this setup also provided an opportunity to evaluate inter-printer variability and its potential impact on print quality. Comparing outputs from both machines allows assessment of whether systematic differences in hardware contributed to variations in pressure decay performance.

Extruder temperature distributions are shown for each filament model and by printer. The plots include both FFC ON and FFC OFF conditions, illustrating the spread and central tendency of the recorded extrusion temperatures during printing. Heater duty cycle (extruder power) distributions are also presented by filament model and printer. These density plots summarize the operational range and frequency of heater output during tube fabrication.

Ambient temperature and humidity distributions during pressure tube printing are provided for each filament model. These plots document the environmental conditions under which the tubes were produced.

Environmental conditions were analyzed to determine whether ambient temperature and humidity contributed to variability in pressure decay performance. Because PETG is hygroscopic and cooling rate influences interlayer bonding, environmental fluctuations could potentially affect leakage behavior[25], [26]. Environmental data were collected and analyzed only for the pressure tube experiments, as tube production was performed in an automated sequence with continuous logging across two different printers and continuously. Tensile coupon batches were initiated manually and are therefore not included in the ambient condition analysis.

2.3.1 Pressure Decay Slope by Printer and FFC Status

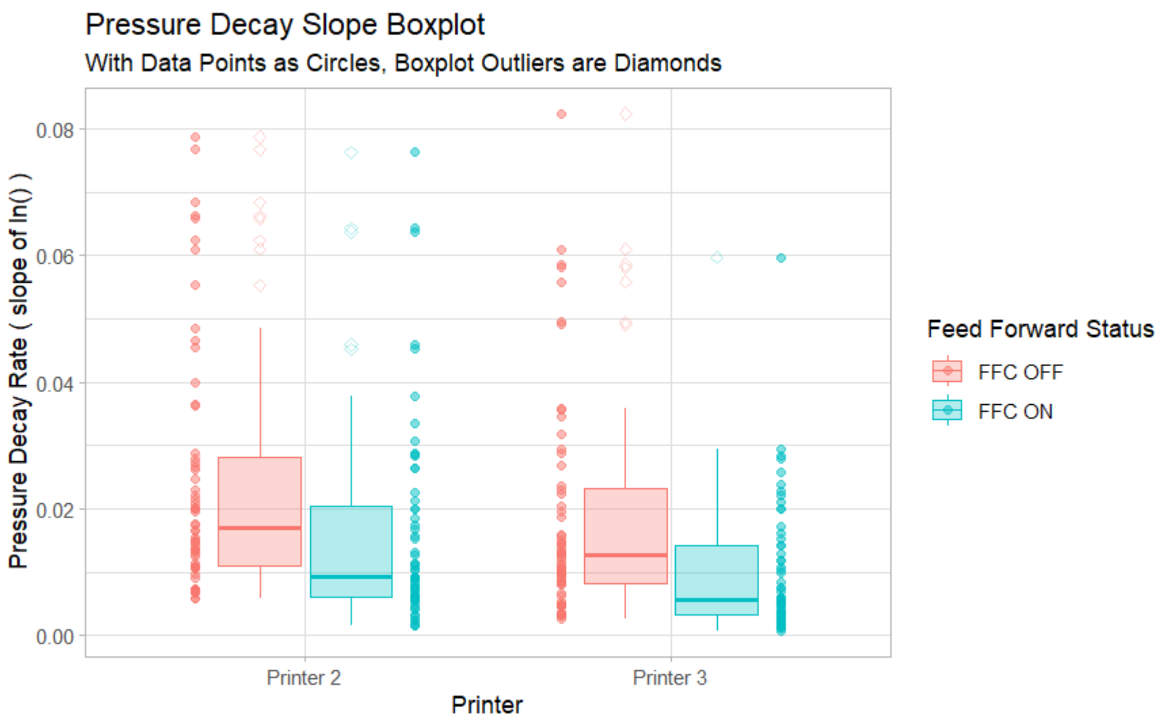

Figure 28-Variation in Printer for decay rate of tubes

Figure 28 shows pressure decay rate distributions grouped by printer and feed forward control condition. Boxplots summarize the distribution of slope values for FFC ON and FFC OFF within each printer. Individual data points and outliers are displayed.

Table 7-Printer vs FFC for decay rate of tubes

Printer	FFC OFF Median(slope)	FFC ON Median(slope)
2	0.0170	0.00929
3	0.0127	0.00572

Printer 2

- Outliers extend up to approximately 0.078

Printer 3

- Outliers extend up to approximately 0.083

For both printers, the median slope under FFC ON appears lower than under FFC OFF. Outliers are visible in both printers, with individual points extending above the upper whiskers, indicating occasional higher slope measurements.

2.3.2 Tube Weight by Printer and FFC Status:

Figure 29 presents tube weight distributions separated by printer and FFC condition. Boxplots display central tendency and variability, with individual observations plotted as points.

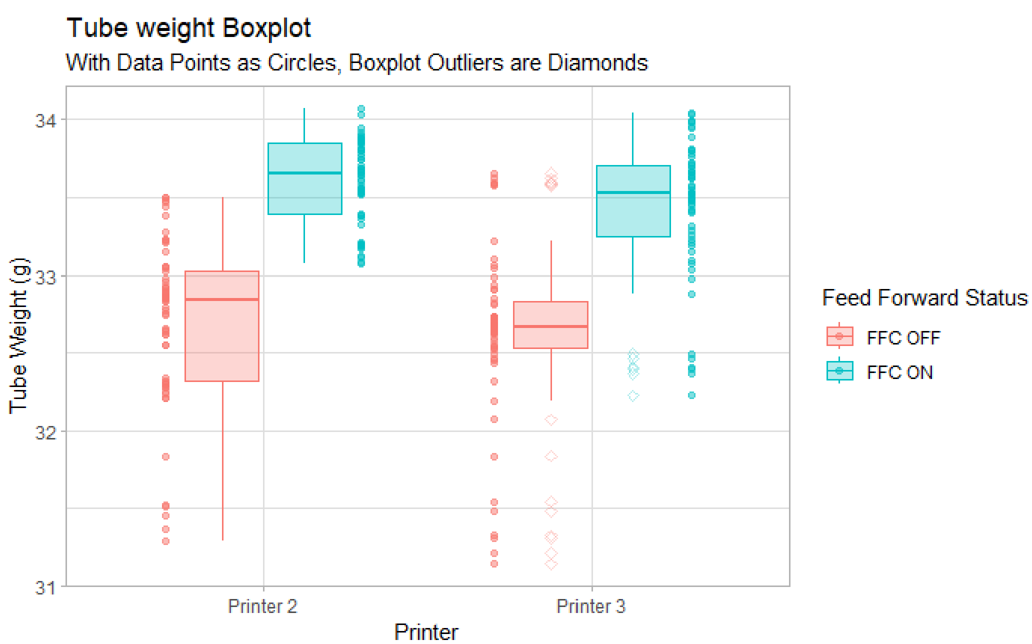

Figure 29- Variation in Printer for weight of pressure tubes

Table 8-Printer vs FFC for weight of tubes

Printer	FFC OFF Median(g)	FFC ON Median(g)
2	32.8	33.7
3	32.7	33.5

Printer 2

- Lower outliers near 31.3 g

Printer 3

- Lower outliers near 31.2 g

For both printers, the median tube weight under FFC ON appears higher than under FFC OFF. Outliers are present in both printers, as shown by data points extending beyond the whiskers in the lower and upper ranges of tube weight.

2.3.3 Extruder Power by Printer Distributions

Figure 30 shows the distribution of heater duty cycle (%) for both printers and FFC conditions. The x-axis represents heater duty cycle, and the y-axis represents statistical density. The highest density for all groups occurs approximately in the mid-range of duty cycle values (around 35–50%), where most measurements are concentrated.

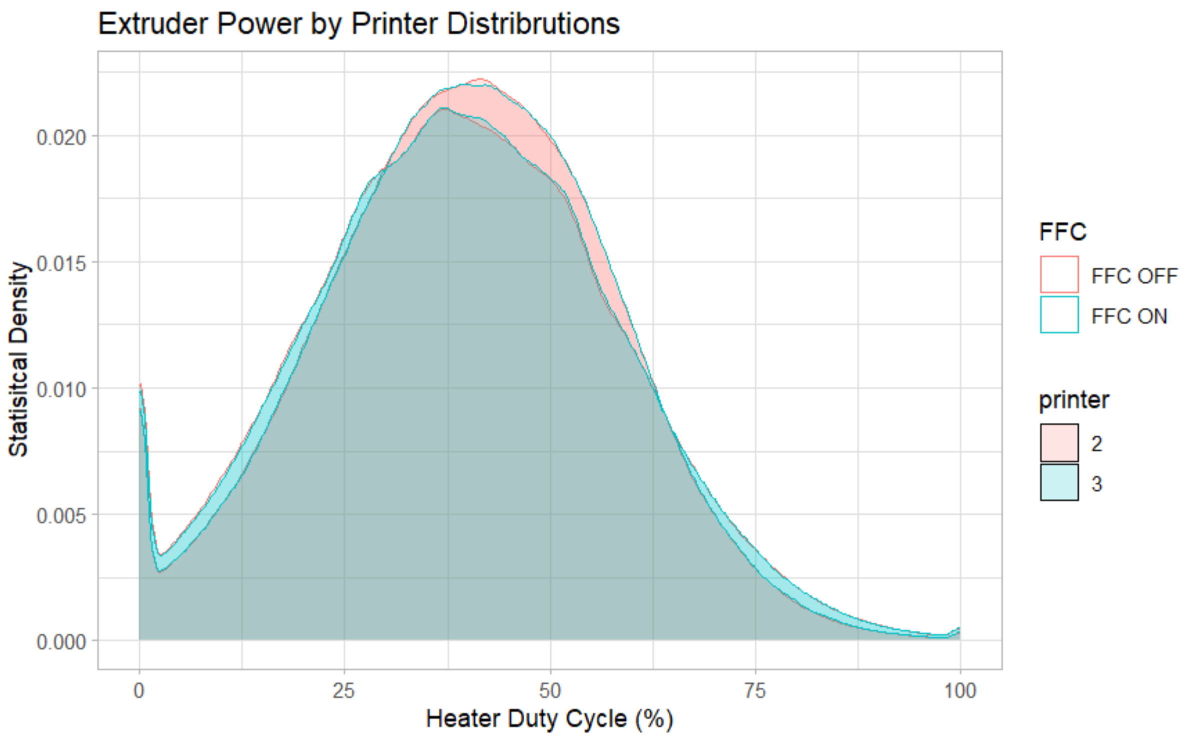

Figure 30- Duty cycle vs Printer for different FFC conditions

2.3.4 Extruder Temperature by Printer

Figure 31 presents the distribution of extruder temperature measurements (°C) for each printer and FFC condition. The density curves show a sharp peak centered near 240°C, indicating that most temperature measurements are concentrated around this value.

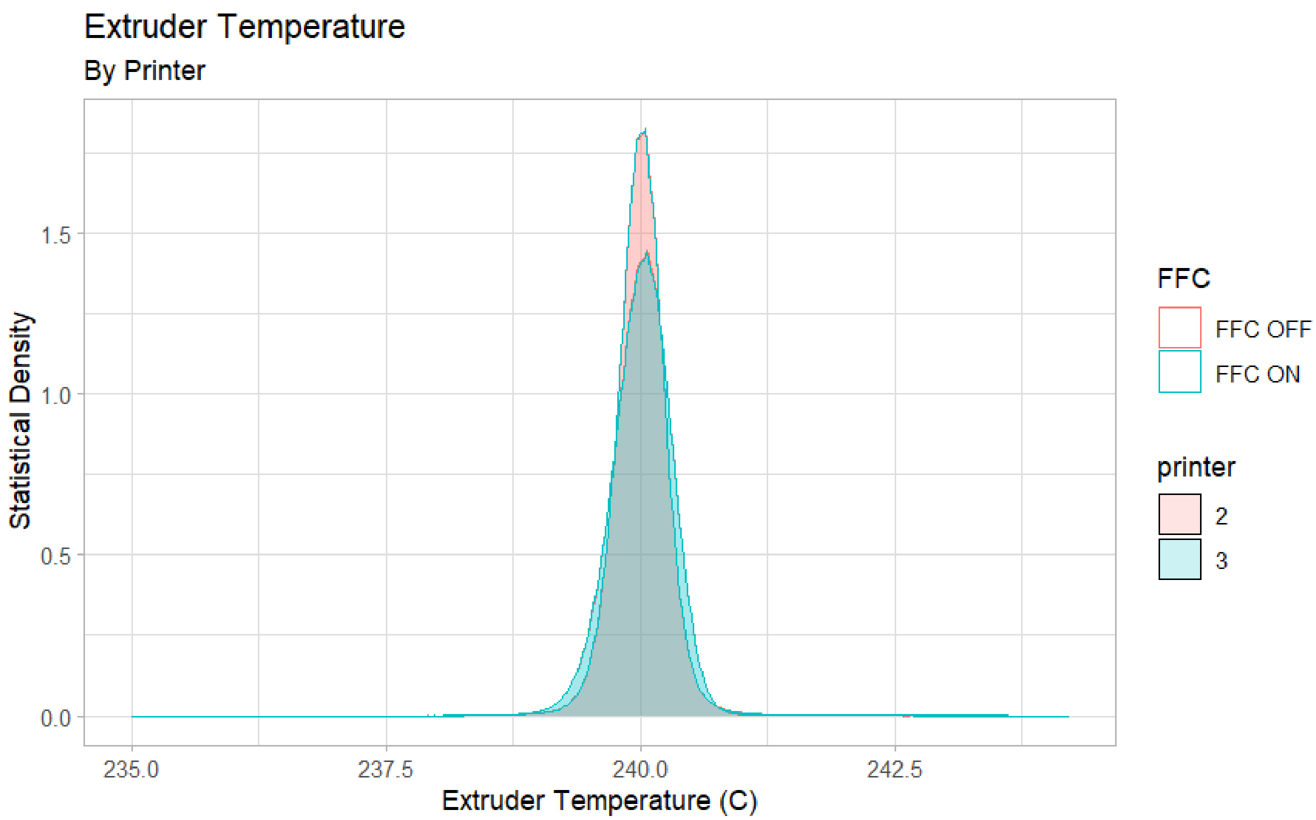

Figure 31-Extruder temperature vs Printer for different FFC conditions

2.3.5 Ambient Print Humidity by Filament Model

Figure 32 shows ambient humidity distribution for each filament model. The x-axis represents humidity (%), and the y-axis represents statistical density. For most filament models, the highest density occurs within the mid-range humidity values (approximately 25–40%), where most measurements are concentrated.

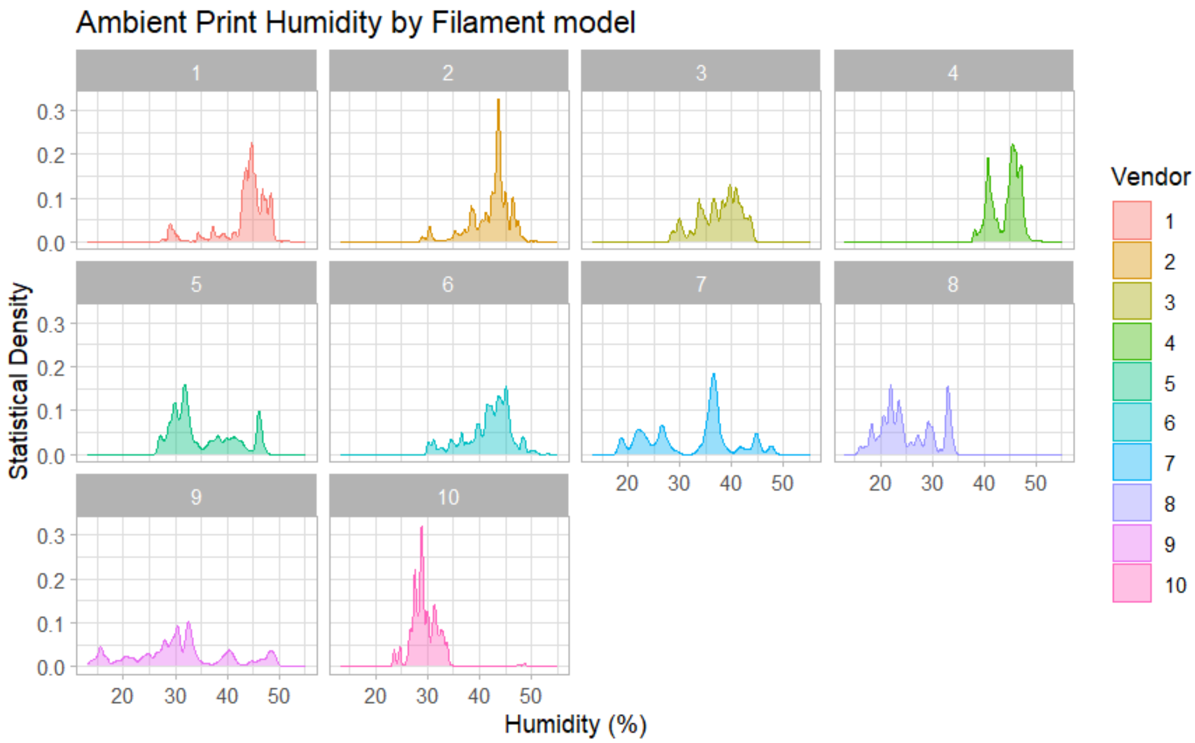

Figure 32-Ambient print humidity during printing of each filament model

2.3.6 Ambient Print Temperature by Filament Model

Figure 33 presents ambient temperature distributions recorded during printing for each filament model. The x-axis represents temperature (°C), and the y-axis represents statistical density. For most filament models, the highest density occurs near approximately 24–26°C, indicating that the majority of ambient temperature measurements fall within this range. The distributions appear relatively narrow, with most observations confined between approximately 23°C and 27°C. Minor variations in spread and peak sharpness are visible between filament models, but the overall temperature range remains consistent across panels. Each subplot provides a model-specific view while maintaining a common temperature scale for direct visual comparison.

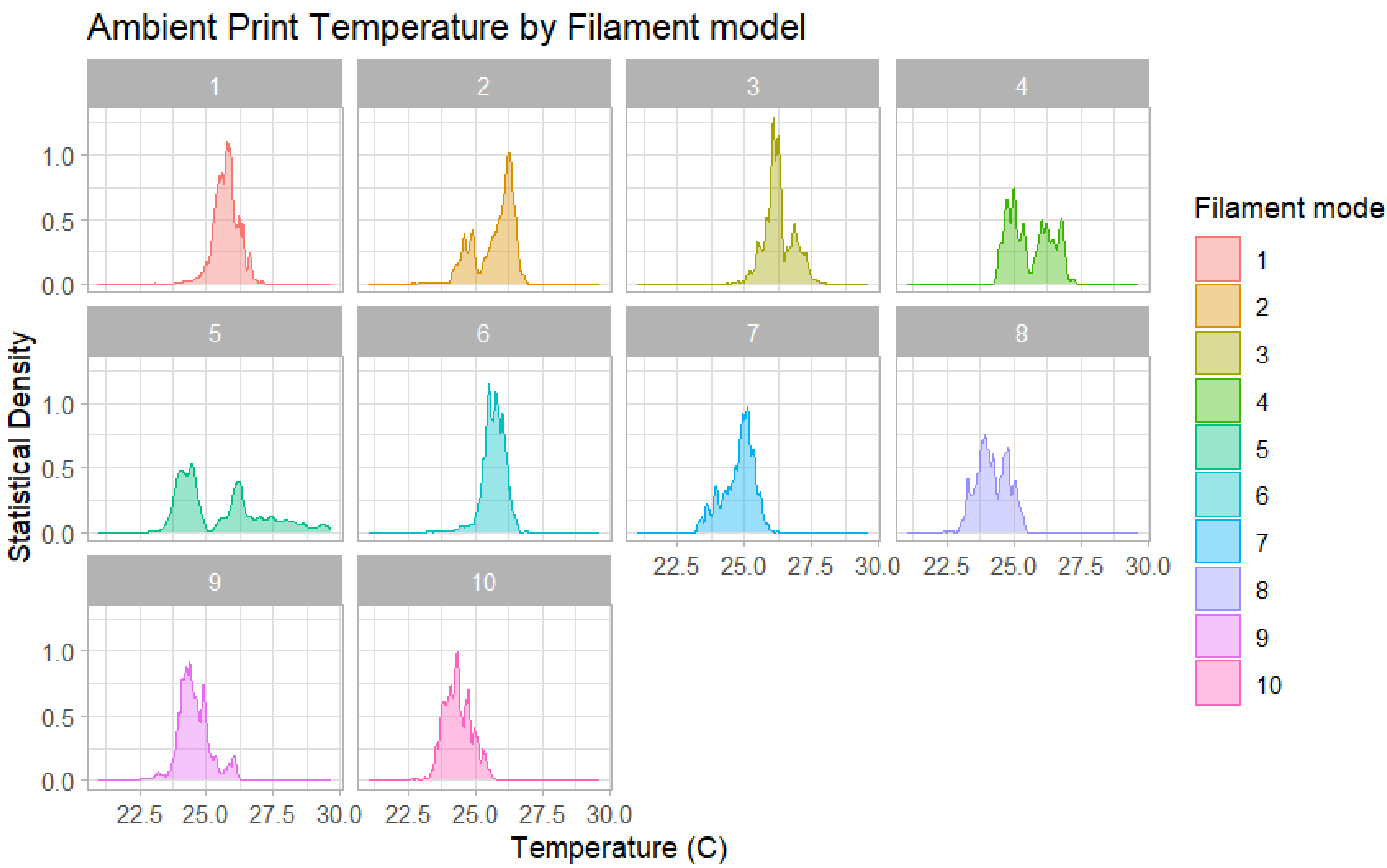

Figure 33-Ambient print temperature during printing of each filament model

2.4 Tensile Coupon printing and testing

Automation was not used in the production of tensile coupons to prevent potential mechanical damage during part removal from the build plate.

All 24 tensile coupons for each filament model were printed on Printer 1. As a result, printer-to-printer variation was not evaluated for the tensile dataset. The coupons were fabricated over multiple days; however, ambient temperature and humidity were not analyzed for these prints.

Force at failure (N) was recorded and reported instead of calculated tensile stress to avoid introducing uncertainty associated with cross-sectional area variation. Although the nominal gauge area of the coupons is 8 mm^2, small dimensional deviations may occur during printing due to filament diameter variability and extrusion dynamics. When such deviations are present, calculating stress using a nominal area may introduce systematic error. Because the primary objective of this study was comparative evaluation of filament models and FFC conditions rather than extraction of intrinsic material properties, applied force was selected as the reported metric. This approach avoids propagating geometric uncertainty into the mechanical comparison. Additionally, fracture surface observations (Fig.41 & Fig.42) indicated the failure characteristics across coupons. Therefore, applied force at fracture was used as the reported mechanical metric. This section presents the tensile test results for all filament models under FFC OFF and FFC ON conditions. The force-at-failure distributions are shown by filament model, FFC status, build number, and print location[27]. These results are presented alongside the corresponding filament diameter distributions for each filament model.

2.4.1 Diameter Distributions by Filament Model (Tensile Coupon Prints)

Figure 34 presents statistical density distributions of filament diameter measurements collected during tensile coupon printing for each filament model. The x-axis represents filament diameter (mm), and the y-axis represents statistical density. Each panel shows overlaid distributions from Diameter Sensor 1 (D1) and Diameter Sensor 2 (D2).

The purpose of this analysis is to evaluate how closely each filament model adheres to its nominal 1.75 mm specification and to assess differences in distribution width and symmetry across vendors. Most commercial filaments are marketed within a tolerance range (e.g., ±0.02

mm), and therefore the expected outcome would be tight clustering around 1.75 mm with minimal spread.

By visualizing the full density distributions for both Diameter Sensor 1 (D1) and Diameter Sensor 2 (D2), this figure allows identification of systematic bias (under- or over-diameter), distribution broadening, and potential ovality effects. Preliminary observation suggests that while most filaments cluster near nominal, noticeable variation in spread and slight shifts from 1.75 mm are present for certain models. The implications of these deviations on mechanical performance are discussed in the subsequent section.

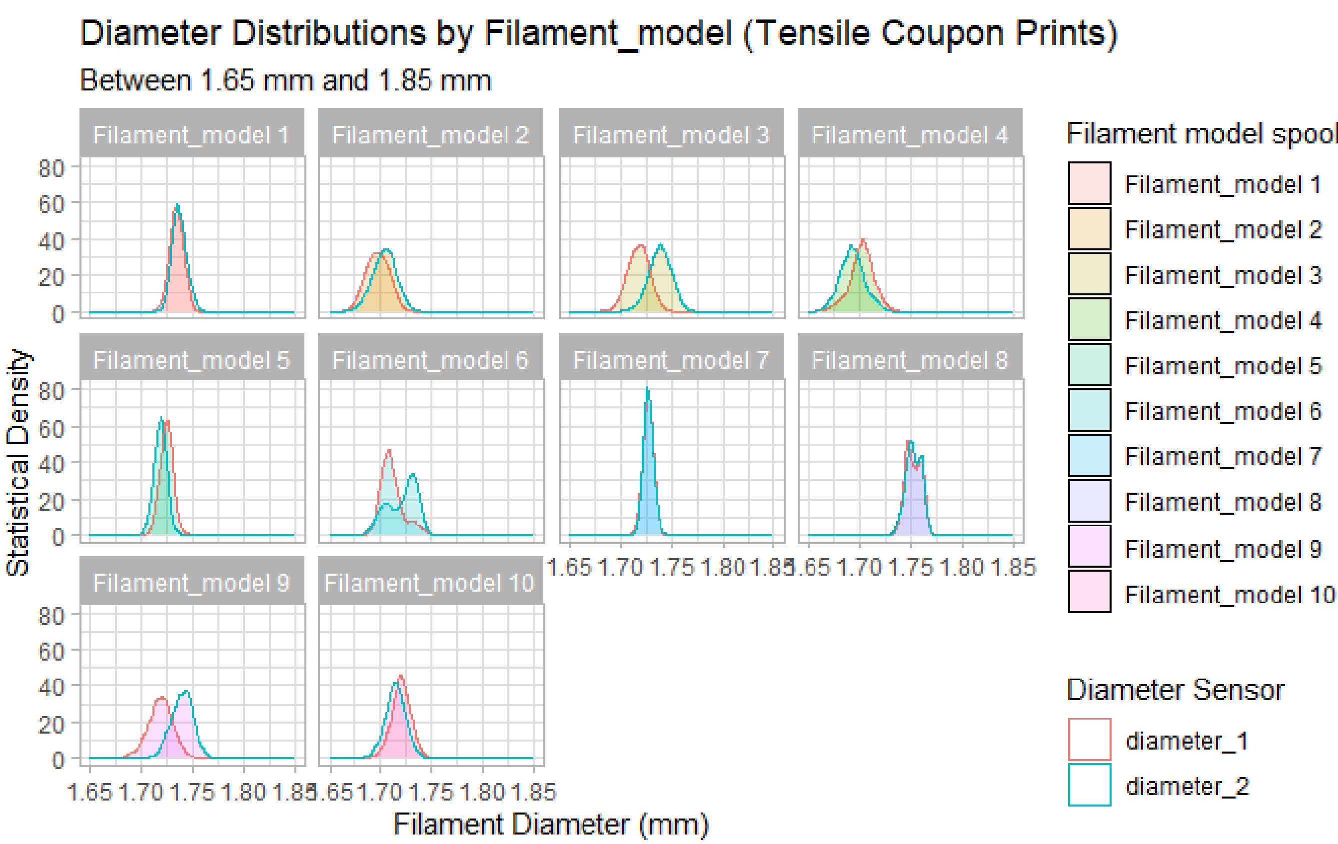

Figure 34-Diameter recordings in the 1.65 to 1.85mm range, by filament model

2.4.2 Diameter Binned Ordered by Mean Tensile Failure Force

Figure 35 presents the percentage of diameter measurements falling within predefined diameter bins for each filament model during tensile coupon printing. The left half of each row represents Diameter Sensor 1 (D1), and the right half represents Diameter Sensor 2 (D2). Filament models are ordered by mean tensile failure force.

Color intensity corresponds to the percentage of measurements within each bin. The majority of measurements for most filament models fall within the central bins (approximately 1.675–1.775 mm), while the outer bins contain minimal percentages.

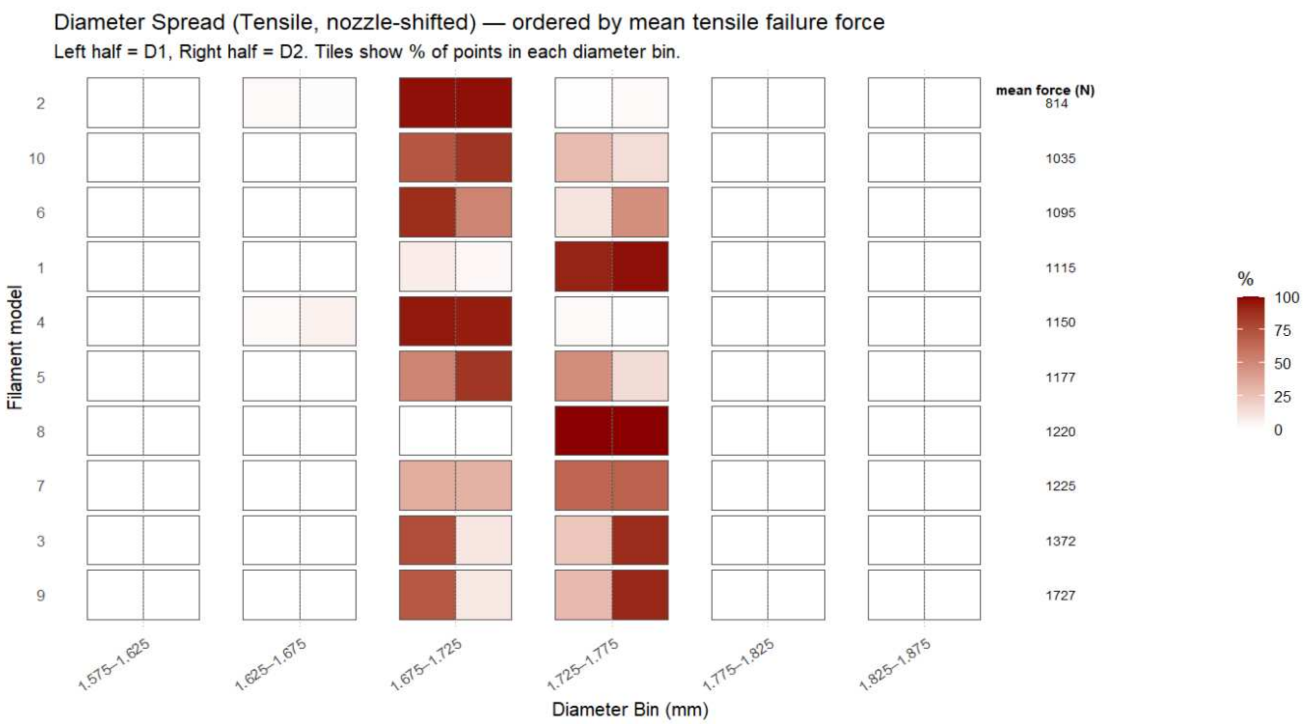

Figure 35-Heatmap of diameters by filament model ordered by mean tensile force

2.4.3 Force at Failure by Filament Model and FFC Status

Figure 36 presents tensile force at failure distributions for each filament model under FFC OFF and FFC ON conditions. The box represents the interquartile range (IQR), the horizontal line within each box indicates the median, whiskers extend to non-outlier limits, and individual points represent measured values.

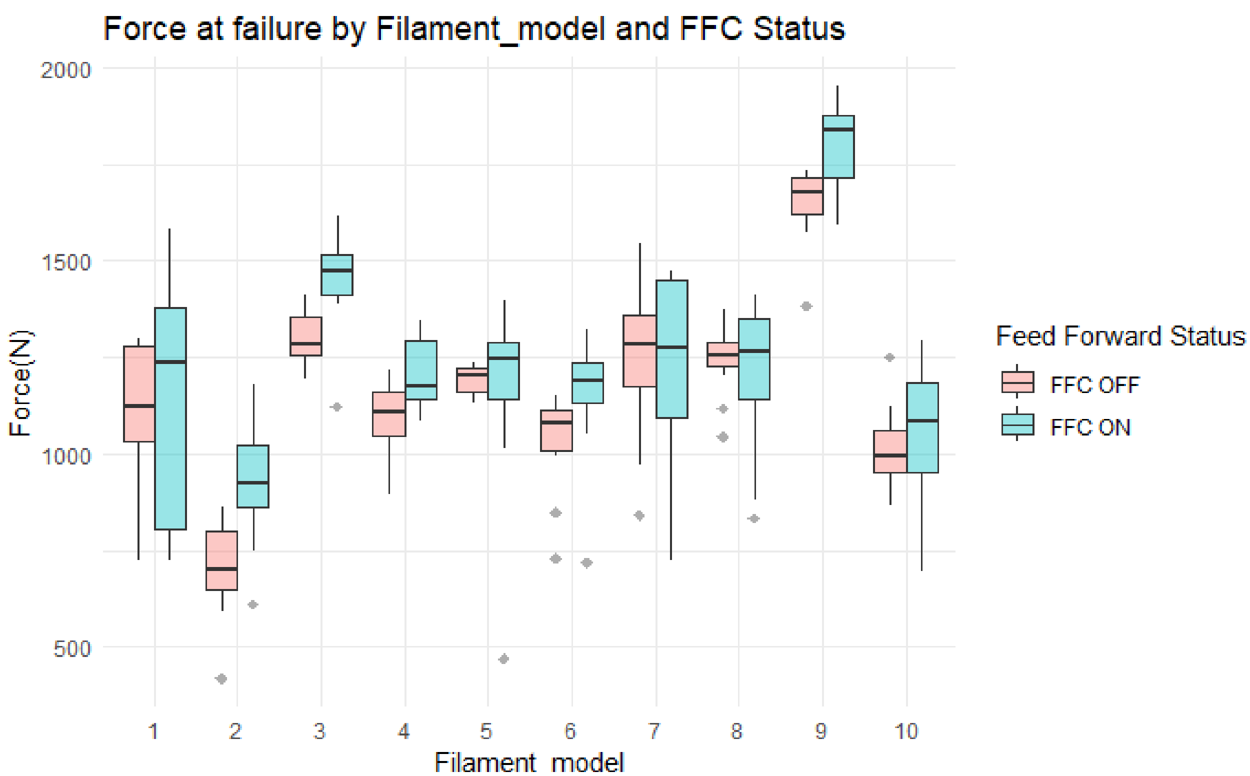

Figure 36- Tensile force at failure by filament model for both FFC conditions

Table 9-Tensile force at failure by filament model for both FFC conditions

Filament Model	FFC OFF Median Force (N)	FFC ON Median Force(N)
1	1106	1123
2	701	926
3	1295	1448
4	1093	1207
5	1191	1164
6	1034	1155
7	1237	1212
8	1238	1202
9	1649	1805
10	1021	1050

Table 10- p value from a Wilcoxon rank-sum test

Filament Model	p value
1	0.23
2	0.0004
3	0.0001
4	0.0102
5	0.159
6	0.001
7	0.48
8	0.42
9	0.0011
10	0.1888

Table 11- p value from Anova

Filament Model	p value
1	0.87
2	0.0008
3	0.0010
4	0.0083
5	0.7081
6	0.047
7	0.794
8	0.584
9	0.0013
10	0.634

To evaluate the effect of Feed Forward Control (FFC) on tensile force at failure, both non-parametric and parametric statistical tests were conducted for each filament model. The Wilcoxon rank-sum test was used as a non-parametric method that compares the relative ordering of values between groups, making it robust to non-normality and outliers. A one-sided hypothesis was employed to evaluate whether FFC ON resulted in higher force at failure than FFC OFF.

The Wilcoxon test results indicated statistically significant improvements in tensile force for filament models 2 ($p = 0.00043$), 3 ($p = 0.00019$), 4 ($p = 0.0102$), 6 ($p = 0.00182$), and 9 ($p = 0.00116$). No significant differences were observed for filament models 1, 5, 7, 8, and 10 ($p > 0.05$).

To complement the non-parametric analysis, a one-way ANOVA was conducted for each filament model to compare mean force values between FFC conditions. The ANOVA results showed statistically significant differences for filament models 2, 3, 4, and 9 ($p < 0.01$), with filament model 6 showing marginal significance ($p \approx 0.048$).

The agreement between the Wilcoxon and ANOVA results indicates that the observed improvements are consistent across both rank-based and mean-based statistical methods. Minor differences in significance, particularly for filament model 6, can be attributed to the sensitivity of ANOVA to mean shifts and the influence of variability within the data.

Overall, these results demonstrate that the effect of FFC on tensile force is not uniform across all filament models. Instead, FFC provides statistically significant improvements for a subset of materials, suggesting that its effectiveness is dependent on filament-specific characteristics such as diameter variability and extrusion consistency.

2.4.4 Force at Failure by FFC Status (Entire Population)

Figure 37 shows the distribution of tensile force at failure for the entire coupon population separated by FFC OFF and FFC ON conditions. The median of the data is represented by the horizontal line within each box.

The median force under FFC ON appears higher than under FFC OFF. Outliers are visible in both conditions, with lower outlier values extending below approximately 600 N and higher outlier values approaching approximately 1900–2000 N.

To evaluate the overall effect of Feed Forward Control (FFC) on tensile force at failure, both a non-parametric Wilcoxon rank-sum test and a one-way analysis of variance (ANOVA) were conducted using the full dataset. The Wilcoxon test was implemented as a one-sided comparison to evaluate the hypothesis that FFC ON produces higher force at failure than FFC OFF. The results indicate a statistically significant increase in tensile force under FFC ON conditions ($W = 6021$, $p = 0.0142$).

To complement the non-parametric analysis, a one-way ANOVA was performed to compare mean force values between FFC conditions. The ANOVA results also indicate a statistically significant effect of FFC on tensile force ($F(1,238) = 4.056$, $p = 0.0451$).

The agreement between the Wilcoxon and ANOVA results demonstrates that the observed improvement in tensile force under FFC is consistent across both distribution-based and mean-based statistical methods. However, the small magnitude of the p-values and the presence of substantial variability in the dataset suggest that the effect of FFC is modest.

These findings indicate that while FFC provides a statistically significant improvement in tensile force at failure across the full population, the effect is not dominant and varies across filament models.

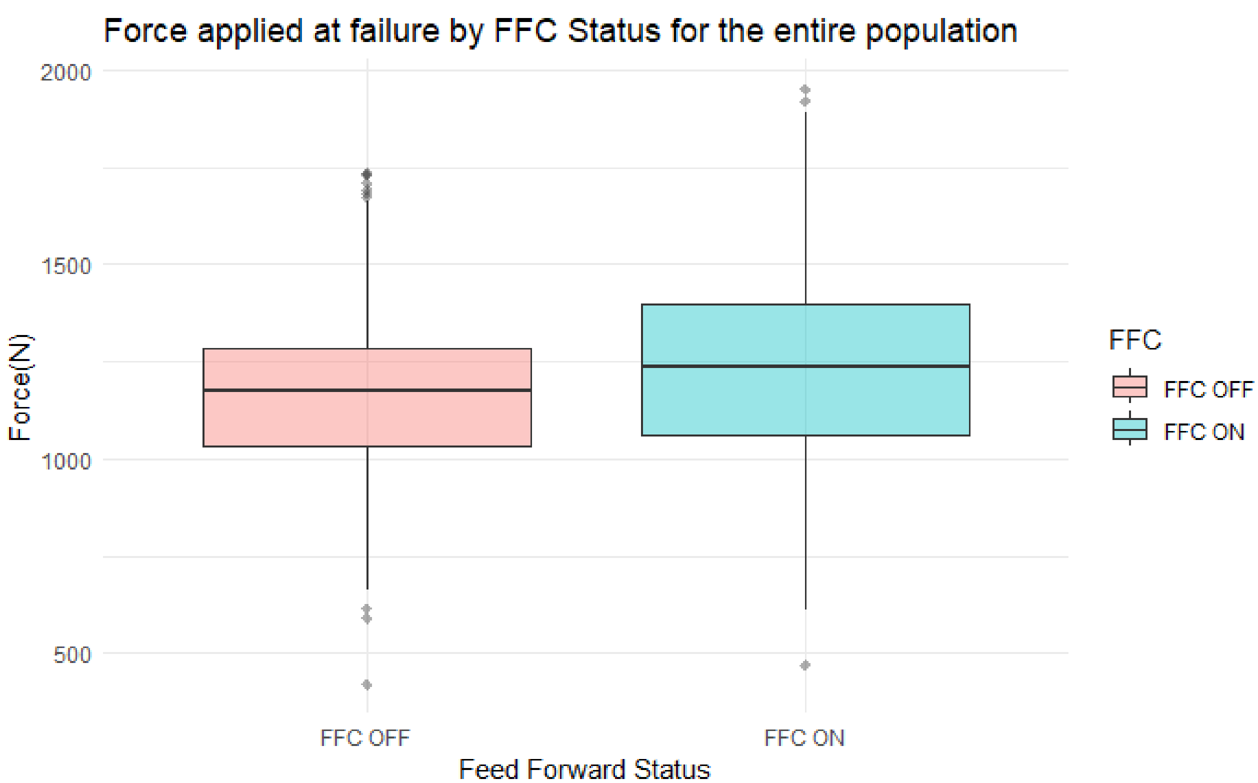

Figure 37- Tensile Force vs FFC

Table 12-Tensile Force vs FFC

FFC OFF Median Force (N)	FFC ON Median Force (N)
1157	1229

2.4.5 Force at Failure by Print Location and FFC Status (Entire Population)

Figure 38 presents the distributions of tensile force at failure grouped by print location (A–D) and FFC condition. Since coupons were printed at different regions of the build plate, variations in location may influence tensile performance, particularly due to differences in inter-layer bonding conditions with a slight change in temperature of the build platform. To investigate this, tensile force at failure was analyzed with respect to both print location and FFC status. Within each location, two boxplots are shown corresponding to FFC OFF and FFC ON conditions, with the median indicated by the horizontal line in each box.

Across locations, the median under FFC ON appears slightly higher than the corresponding FFC OFF median. Outliers are visible in multiple locations, with several data points extending above 1700–1900 N and some lower values near approximately 400–600 N. To evaluate the effects of both FFC and location on tensile force, a two-factor ANOVA was conducted. The results indicate that FFC has a statistically significant effect on tensile force ($F(1,235) = 4.051$, $p = 0.0453$), while location does not have a statistically significant effect ($p = 0.753$).

These results indicate that fracture location does not influence tensile strength, and that the observed differences in force are not dependent on where failure occurs within the coupons.

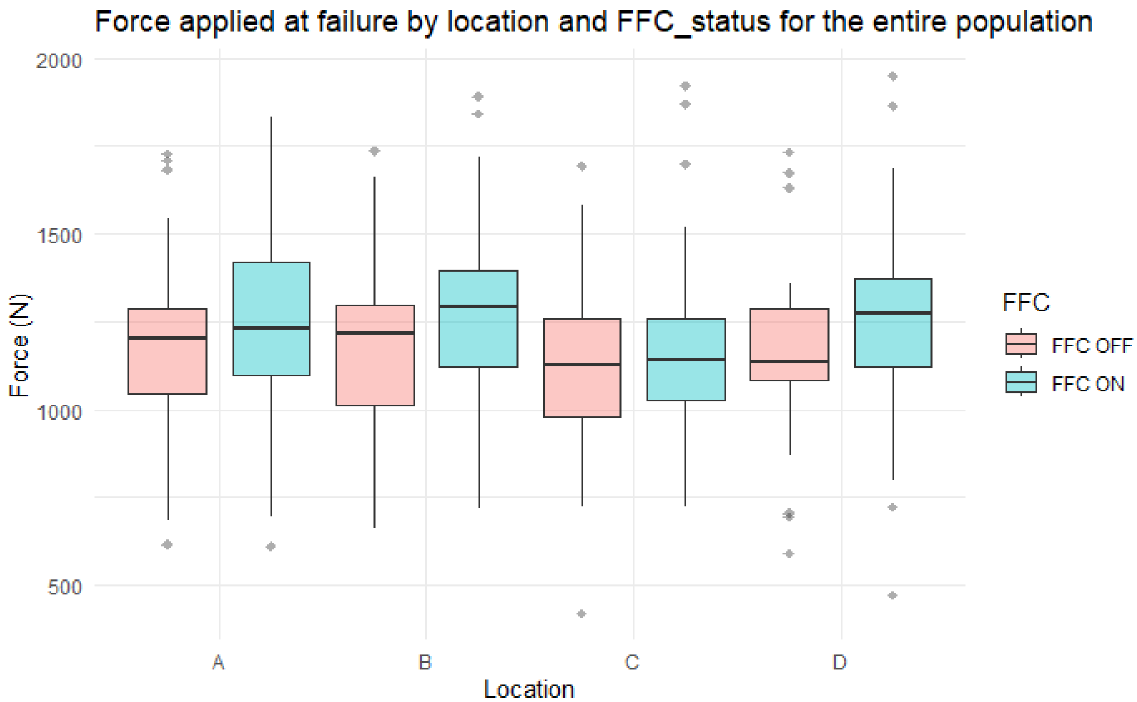

Figure 38-Tensile Force by location of coupon on build platform & FFC

Location	FFC OFF Median (N)	FFC ON Median(N)
A	1194	1228
B	1159	1283
C	1295	1448
D	1116	1172

Table 13-Tensile Force by location of coupon on build platform & FFC

2.4.6 Force at Failure by Build Number and FFC Status (Entire Population)

Each build number represents a distinct print run under nominally identical conditions. To evaluate whether variations between print batches influence tensile force at failure a one- way ANOVA was conducted with build number included as a factor alongside Feed Forward Control (FFC).

The results indicate that build number does not have a statistically significant effect on tensile force ($p = 0.444$), while FFC remains statistically significant ($p = 0.0453$). This shows that variations between builds do not meaningfully influence mechanical performance.

Figure 39 displays tensile failure force distributions grouped by build number and FFC condition. For each build number, two boxplots represent FFC OFF and FFC ON. The median is indicated by the horizontal line within each box.

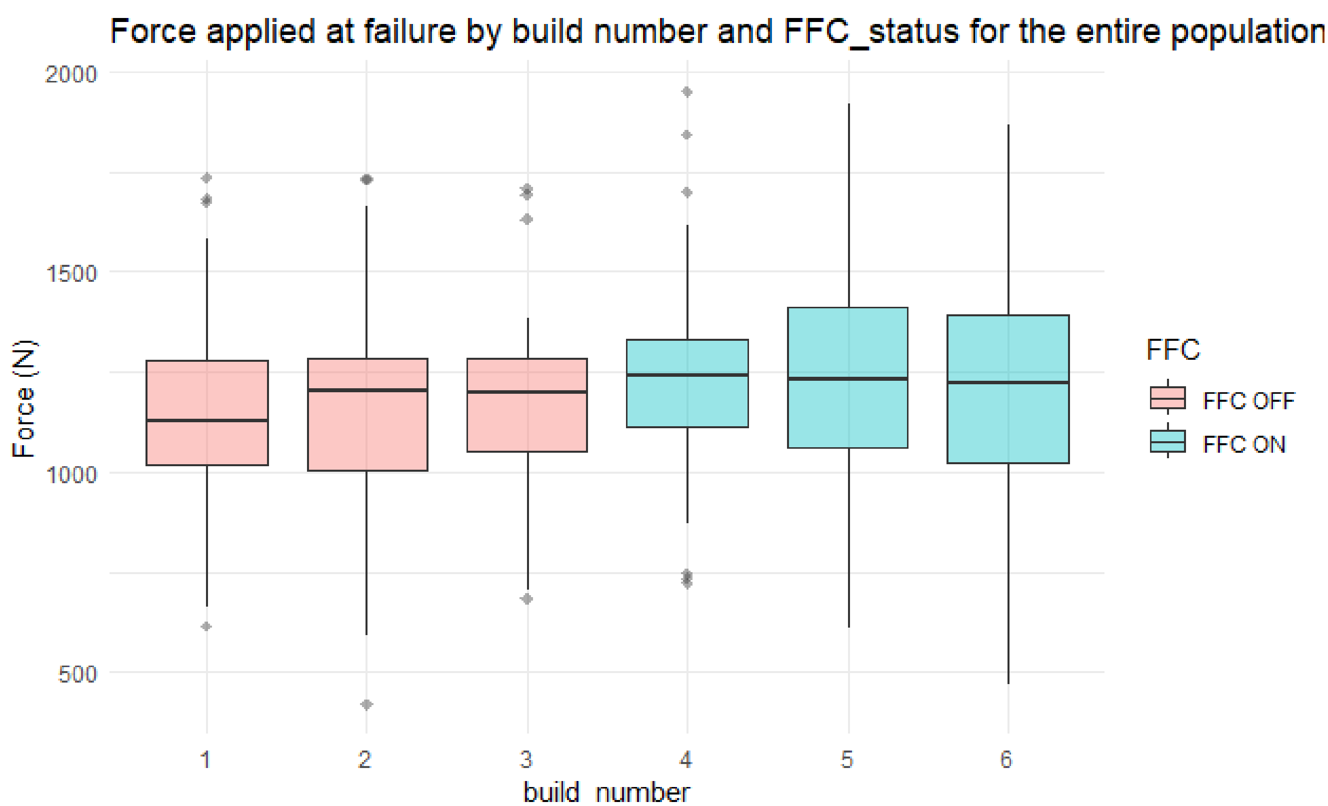

Figure 39- Tensile force vs Build number & FFC

An important experimental limitation should be noted here: because FFC was disabled for builds 1–3 and enabled for builds 4–6, FFC status is fully confounded with build number in the tensile dataset. This means that any systematic difference between the first and second half of the build sequence such as gradual changes in ambient conditions, or printer thermal drift over the course of the experiment could in principle contribute to the observed difference in tensile force between FFC OFF and FFC ON builds. However, the ANOVA results indicate that build number alone does not have a statistically significant effect on tensile force ($p = 0.444$), suggesting that build sequence effects are small relative to the FFC effect. The improvement in tensile performance attributed to FFC is therefore considered real, while acknowledging that the experimental design does not allow complete separation of these two variables.

Table 14-Tensile force vs Build number & FFC

Location	FFC State	Median(N)
1	OFF	1151
2	OFF	1152
3	OFF	1167
4	ON	1246
5	ON	1239
6	ON	1203

2.4.7 Fracture Height & location from Bottom by FFC Status

While all coupons are tested at ambient conditions after complete cooling, the influence of thermal effects arises from the thermal history during printing rather than ongoing heat transfer during testing. Lower layers experience longer cooling times and solidify earlier, while upper layers are deposited onto relatively warmer material. This results in variations in interlayer bonding quality and residual thermal stresses along the build direction. These differences persist after cooling and can influence fracture location, even though no significant convective heat transfer occurs during mechanical testing.

Fracture height was measured from the bottom of the coupon to maintain a consistent reference frame aligned with the build direction of the printed part. Since the coupons are fabricated layer-by-layer starting from the bottom surface, this reference allows fracture location to be interpreted relative to the thermal and bonding history experienced during printing.

To further understand the nature of failure, visual inspection of fractured coupons (Figure 41 & 42) shows that all coupons exhibit relatively flat fracture surfaces, with no evidence of shear failure. This indicates that failure occurs primarily through tensile separation between layers, rather than through localized shear failure

Under FFC OFF, fracture locations appear more widely distributed across the coupon height, with multiple peaks observed throughout the gauge section. Under FFC ON, fracture heights remain broadly distributed but show slight shifts towards the middle of the gauge section. However, fracture events are not confined to a single dominant location in either FFC on or FFC off condition. The absence of a dominant fracture location, together with consistent fracture morphology, indicates that variations in tensile strength are not driven by where failure occurs, but by the overall quality of bonding between deposited layers.

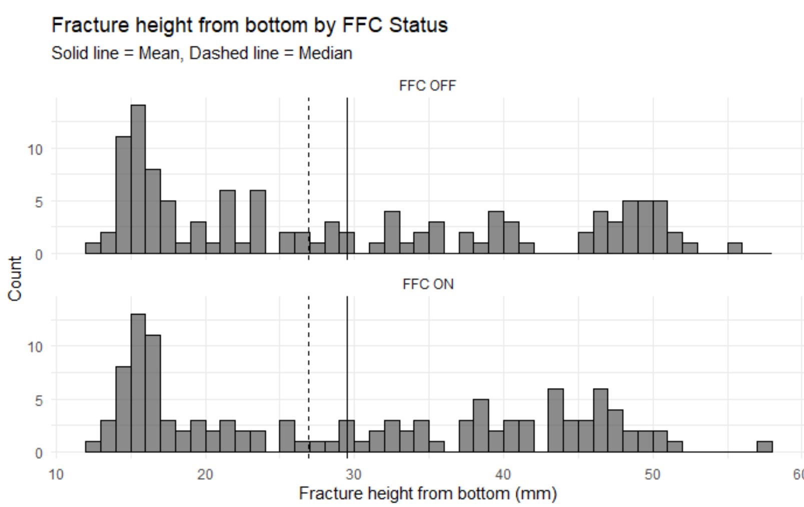

Figure 40-Fracture height by FFC

Figure 41- Zoomed up view of area of failure

Figure 42- Multiple coupons

2.5 Differential Scanning Calorimetry (DSC) Analysis

Differential Scanning Calorimetry is a thermal analysis technique used to measure heat flow into or out of a material as it is subjected to a controlled temperature program. As the temperature increases, thermal transitions such as glass transition, crystallization, or melting events appear as changes in heat flow. These transitions can provide information about the thermal properties and phase behavior of polymer materials.

To investigate whether differences in thermal behavior could explain variations observed in tensile performance between filament models, Differential Scanning Calorimetry (DSC) analysis was performed on a subset of filaments. Selected filaments included models that exhibited notably different tensile failure forces during mechanical testing. The goal was to determine whether measurable thermal transitions or differences in heat flow behavior were present between these materials [28].

The DSC measurements were used to compare the thermal behavior of selected filament samples and to determine whether observable thermal transitions differed between materials.

DSC Heating Curve

Figure 43 shows the DSC heating scan for the selected filament samples. The x-axis represents temperature (°C), while the y-axis represents heat flow. Each curve corresponds to a different filament vendor.

Across all samples, the heat flow changes gradually as temperature increases from room temperature to approximately 250°C. A noticeable transition region appears around approximately 70–90°C, where a change in slope in the heat flow curve is visible for most samples. Beyond this region, the heat flow continues to vary gradually with increasing temperature until the end of the scan.

Differences in heat flow magnitude are visible between filament samples, but the overall shape of the curves remains similar across vendors, indicating that all materials undergo similar thermal transitions, with very small differences primarily in the magnitude of heat flow rather than the transition behavior itself.

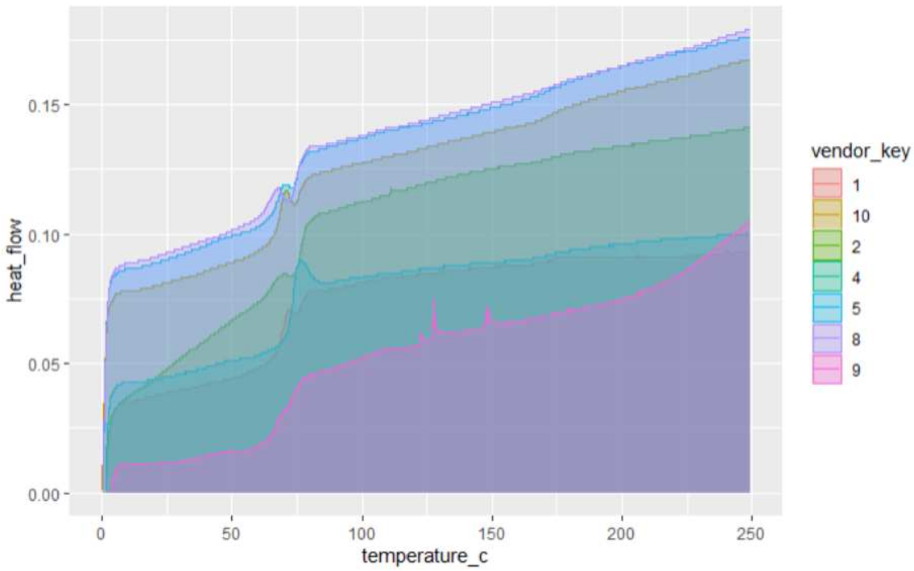

Figure 43- Heating curve during DSC tests for selective filaments

DSC Cooling Curve

Figure 44 presents the DSC cooling scan for the same filament samples. The x-axis represents temperature (°C), and the y-axis represents heat flow during the cooling process.

During cooling from approximately 250°C to room temperature, the heat flow decreases gradually for most samples. A transition region is visible near approximately 70–90°C, where a change in heat flow slope occurs across multiple filaments. This indicates that the cooling behavior and associated thermal transitions are largely consistent across filament models, suggesting similar crystallization or solidification characteristics despite differences in heat flow magnitude.

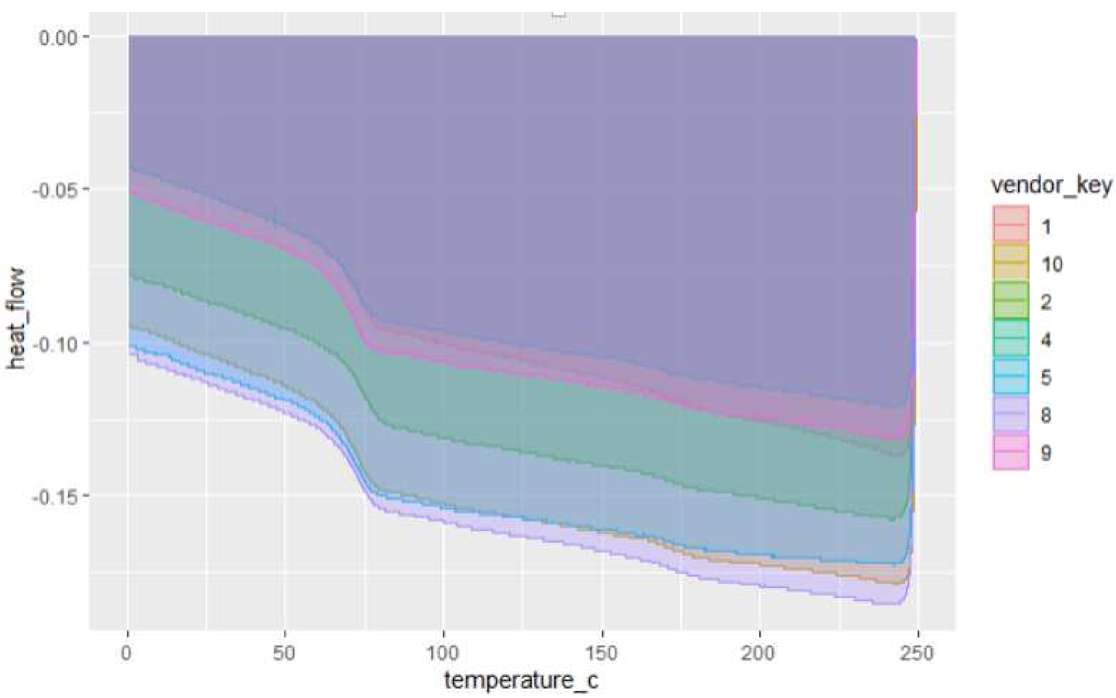

Figure 44-Cooling curve during DSC tests for selective filaments

2.6 Filament Cross-Sectional Geometry and Volumetric Consistency

To evaluate the dimensional consistency of the filament, ovality, cross-sectional area, and rolling volumetric variation were derived in real-time from dual, orthogonal measurements of filament diameter. These geometric metrics provide a quantitative description of filament geometry and its potential influence on extrusion and road bonding behavior during printing.

For analysis of ovality vs decay rate, only diameter measurements form pressure tube prints were used. Pressure tubes required substantially longer filament lengths compared to tensile coupons, resulting in a larger number of diameter measurements along the filament path. Approximately 10 meters of filament were used to print each pressure tube, whereas approximately 2 meters of filament were used per tensile coupon. The longer filament length associated with pressure tube printing therefore provided a larger sampling window of filament geometry, enabling more representative characterization of cross-sectional variation along the filament.

From the orthogonal diameter measurements, cross-sectional areas were calculated to estimate the instantaneous filament area relative to the nominal filament diameter. Ovality was calculated from the difference between the orthogonal diameter measurements and represents deviation from a circular filament cross-section.

2.6.1 Pressure Decay Rate by Dominant Area Band

For each printed tube, the filament diameter measurements from the orthogonal sensors used during the print were converted to cross-sectional area values. These values were then compared to the nominal filament cross-sectional area. The dominant area band represents the percentage range in which the majority of cross-sectional area measurements for that tube fall. A 100% band indicates that most of the measured filament cross-sectional areas were close to the nominal area, whereas 95% and 90% bands indicate that the dominant portion of the filament cross-section fell within approximately 95% or 90% of the nominal filament area, respectively. This grouping therefore reflects the degree to which the filament cross-section during a print deviates from the nominal value.

Figure 45 shows the distribution of pressure decay rate values grouped by dominant cross-sectional area band expressed as a percentage of the nominal filament cross-sectional area (2.40

mm²). The x-axis represents the dominant area band category (90%, 95%, and 100%), while the y-axis represents the pressure decay rate (slope of ln ()).

Each violin plot represents the distribution of measurements within that area band, with the embedded boxplot indicating the interquartile range and the horizontal line representing the median value.

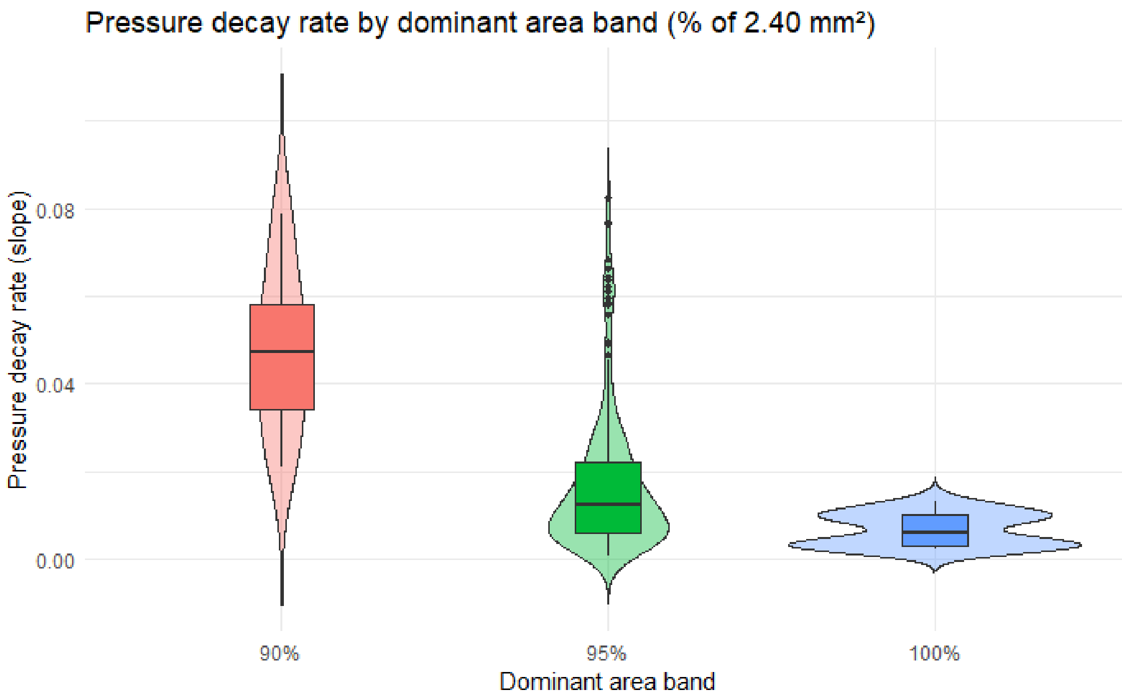

Figure 45- Dominant area band vs Pressure Decay rate

Table 15-Dominant Area band vs Slope of Pressure decay

Dominant Band	Median(slope)
90%	0.0476
95%	0.0175
100%	0.00685

2.7 Filament Models: Ovality vs Price

Figure 46 shows the relationship between mean filament ovality measured from pressure tube data and the mean price of each filament model. The x-axis represents the mean ovality from pressure tubes (mm) and the y-axis represents the mean price ($/kg). Each point corresponds to a filament model and is labelled by model number.

A dashed regression line is shown with the calculated correlation coefficient r = 0.409. The ovality values span approximately 0.006 mm to 0.023 mm, while the mean price ranges approximately $22/kg to $80/kg. This indicates a weak relationship between filament price and ovality

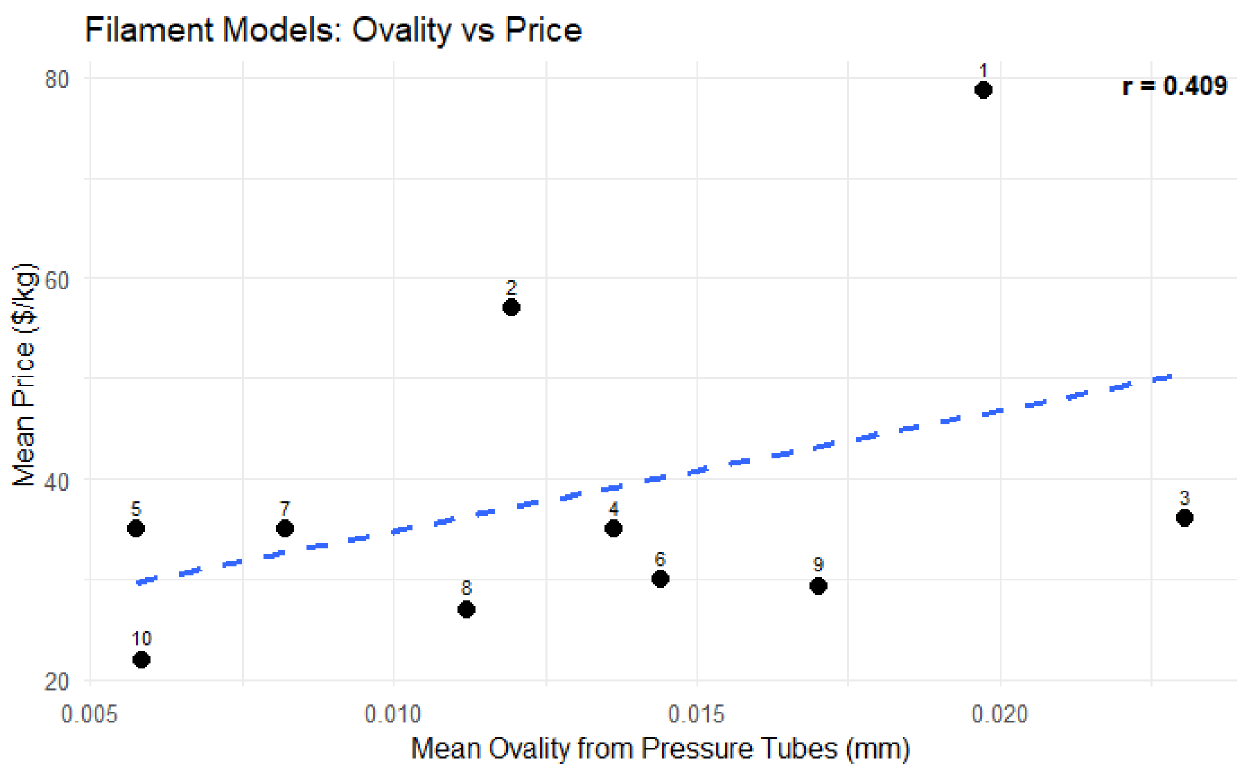

Figure 46- Ovality vs Price

2.8 Rolling Volume Loss Definition

To quantify localized volumetric variation in the filament, a rolling volume window was computed along the measured filament length. Rather than evaluating filament volume at individual points, the rolling window approach evaluates the cumulative filament volume contained within a fixed-length segment of filament. This allows localized reductions in cross-sectional areas to be captured within the window length used during printing.

At each sampled position along the filament, the instantaneous filament cross-sectional area was calculated using the two orthogonal diameter measurements obtained from the dual sensor system:

$$A_i = \frac{\pi}{4} d_{1,i} d_{2,i} \tag{1}$$

where $d_{1,i}$and $d_{2,i}$are the orthogonal filament diameter measurements at sample i.

During printing, the logging system records the incremental extrusion distance between successive samples, denoted as Δx_i. Using these measurements, the rolling filament volume beginning at sample i was calculated by summing the filament volume contributions over a 230 mm moving window:

$$V_{\text{roll}}(i) = \sum_{k=i}^{j(i)} A_k \, \Delta x_k \tag{2}$$

where $j(i)$ is the final sample index included such that the cumulative extrusion distance within the window satisfies

$$\sum_{k=i}^{j(i)} \Delta \, x_k \leq 230$$

This rolling calculation represents the total filament volume contained within a 230 mm segment of filament beginning at sample i. The window is then advanced along the filament length, producing a rolling sequence of volume values that capture localized volumetric variation.

The nominal filament volume corresponding to the same 230 mm window was calculated using the nominal filament diameter $d_{nom} = 1.75$mm:

$$A_{nom} = \frac{\pi}{4} d_{nom}^2 \tag{3}$$

$$V_{nom} = A_{nom} \times 230 \tag{4}$$

With the diameters recorded earlier from both tensile coupons and pressure tube prints (Fig.21 & Fig.34), we can infer that the rolling volume calculated will be less than the nominal filament volume, the rolling volume loss was then defined as the difference between the nominal filament volume and the measured rolling filament volume:

$$V_{\text{loss}}(i) = V_{nom} - V_{\text{roll}}(i) \tag{5}$$

This metric represents the reduction in available filament material relative to the nominal filament volume within any 230 mm segment of filament.

For each printed part, the minimum rolling volume (or equivalently the maximum rolling volume loss) observed along the filament segment used during the print was used as the representative metric for subsequent analysis.

Following the calculation of rolling volume loss, the relationship between localized filament volumetric variation and pressure retention performance was examined for all pressure tubes and tensile coupons.

2.8.1 Selection of Rolling Window Length

The rolling window length used for the volumetric analysis differed between the pressure-tube and tensile-coupon datasets. As mentioned in section 2.8, for the pressure tube analysis, a rolling window length of 230 mm was used. This value was selected to remain consistent with an earlier study in which filament segments were intentionally stretched over a 230 mm length to introduce localized geometric deformation and evaluate whether printed parts would fail at that location. While the present work did not intentionally introduce filament deformation prior to printing, the same window length was retained for consistency with that earlier experimental framework.

For the tensile coupon analysis, the same 230 mm window length could not be used because the total filament length used to print an individual coupon was significantly shorter (approximately 2 m per coupon). Using a 230 mm rolling window would therefore span a relatively large portion of the filament used to produce a single coupon and reduce the ability to observe localized volumetric variation. Instead, a 65 mm rolling window was used, corresponding approximately to the height of the printed tensile coupon.

The specific window lengths themselves are not intended to represent a physically critical dimension. Rather, the rolling window serves as a means of capturing localized volumetric variation in the filament over a defined segment length. The metric of interest is therefore the volume loss observed within the rolling window, which reflects localized deviations in filament cross-sectional area relative to the nominal filament geometry.

2.8.2 Effect of FFC on Rolling 230 mm Volume Loss vs Pressure Slope

Figure 47 shows the relationship between rolling window volume loss and pressure decay rate. The x-axis represents rolling window volume loss (mm^3), and the y-axis represents pressure decay rate (slope). Points are colored according to feed forward control status (FFC OFF and FFC ON).

Solid lines represent regression fit with shaded 90% confidence intervals, while dashed lines represent 90% prediction intervals. Rolling window volume loss values range approximately from 8 mm³ to 50 mm³, with pressure decay rates spanning approximately 0 to 0.08.

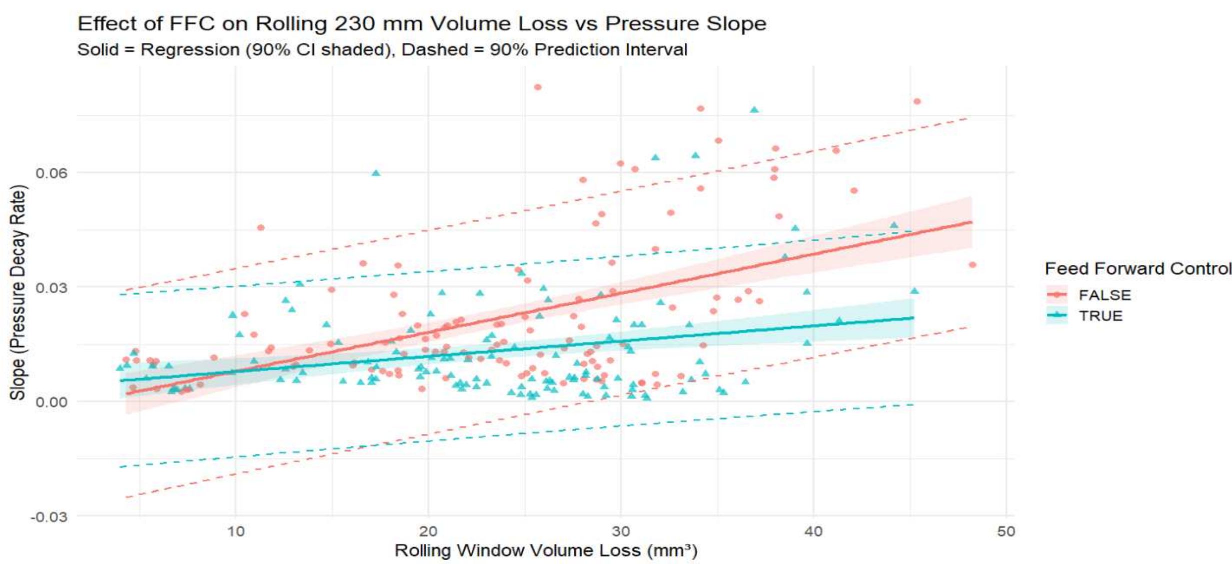

Figure 47-Rolling Volume loss vs Slope of Decay rate

To further examine whether this relationship varied between materials, the relationship between rolling volume loss and pressure decay rate was also evaluated separately for each filament model. Figure 48 presents the rolling volume loss versus pressure decay slope for each of the ten filament models individually, with regression trends shown for prints performed with and without feed forward control. Because each filament model exhibits a different range of rolling volume variation, the horizontal axis scale differs slightly between panels. For example, filament model 8 exhibits a comparatively narrower range of rolling volume loss values, indicating smaller variations in filament cross-sectional area when compared to the nominal area of cross section along the sampled filament segments.

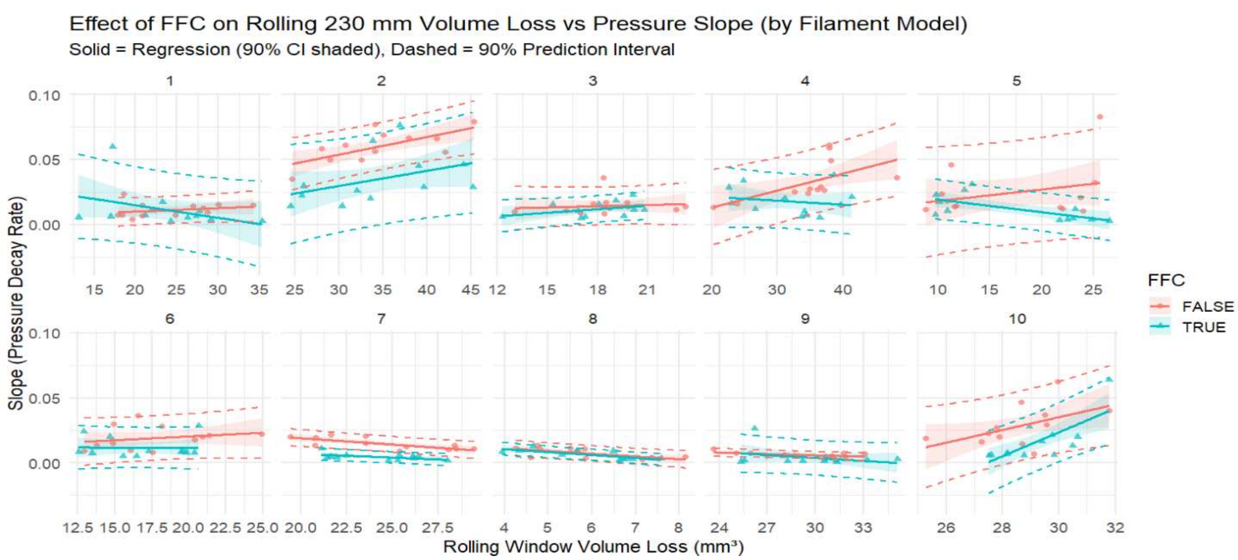

Figure 48- Rolling Volume loss vs Decay rate by filament model

In addition to pressure decay behavior, the relationship between filament volumetric variation and mechanical performance was also evaluated. Figure 49 presents the relationship between minimum rolling volume and tensile force at failure for printed tensile coupons. For this analysis, the rolling volume metric was computed using diameter measurements recorded during tensile coupon printing only, ensuring that the volumetric measurements corresponded directly to the filament segments used to produce each tensile coupon. This allowed localized filament volume variation to be compared directly with the measured tensile failure force of the corresponding printed coupons.

2.8.3 Effect of FFC on Minimum Rolling Volume vs Tensile Force at Failure

Figure 49 shows the relationship between minimum rolling volume and tensile force at failure for the entire population of tensile coupons. The x-axis represents minimum rolling volume, while the y-axis represents tensile force at failure (N). Points are colored by FFC ON or OFF condition.

Regression lines are shown for both FFC conditions with shaded 90% confidence intervals and dashed 90% prediction intervals. Minimum rolling volume values span approximately 143 to 156 mm³, while tensile failure forces range approximately from 400 N to nearly 2000 N.

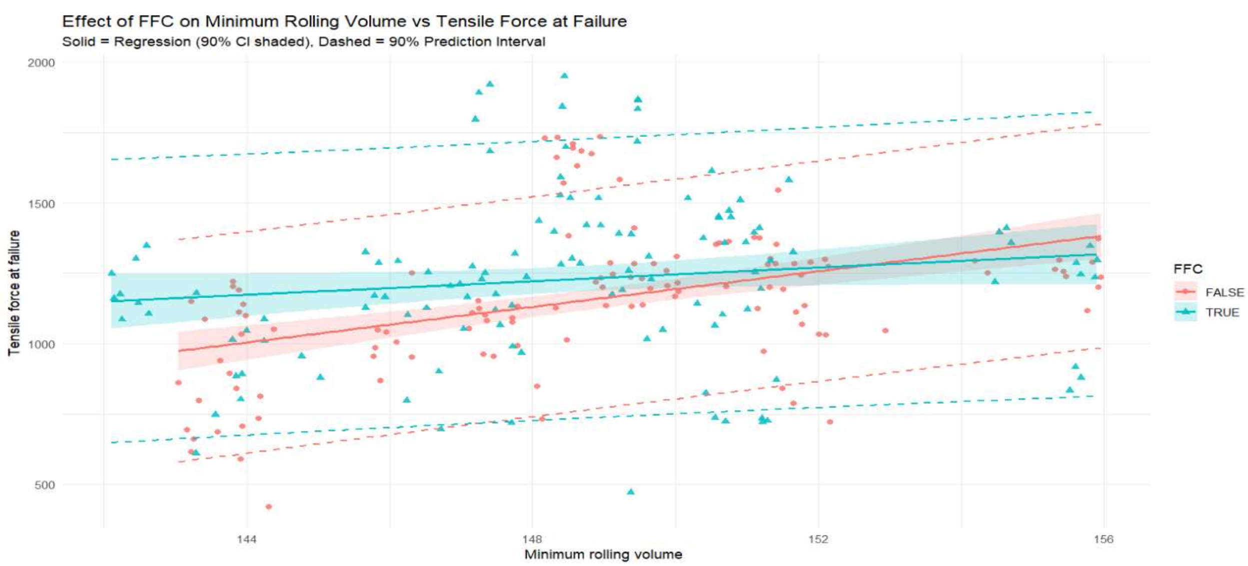

Figure 49-Rolling Volume loss vs Tensile force

To further examine whether the relationship between filament volumetric consistency and mechanical performance varied between materials, the relationship between minimum rolling volume and tensile force at failure was also evaluated separately for each filament model. Figure 50 presents minimum rolling volume versus tensile failure force for each of the ten filament models individually, with separate regression trends shown for FFC OFF and FFC ON conditions. The horizontal axis range differs between panels because each filament model exhibits a different spread in minimum rolling volume values based on the diameter measurements recorded during tensile coupon printing.

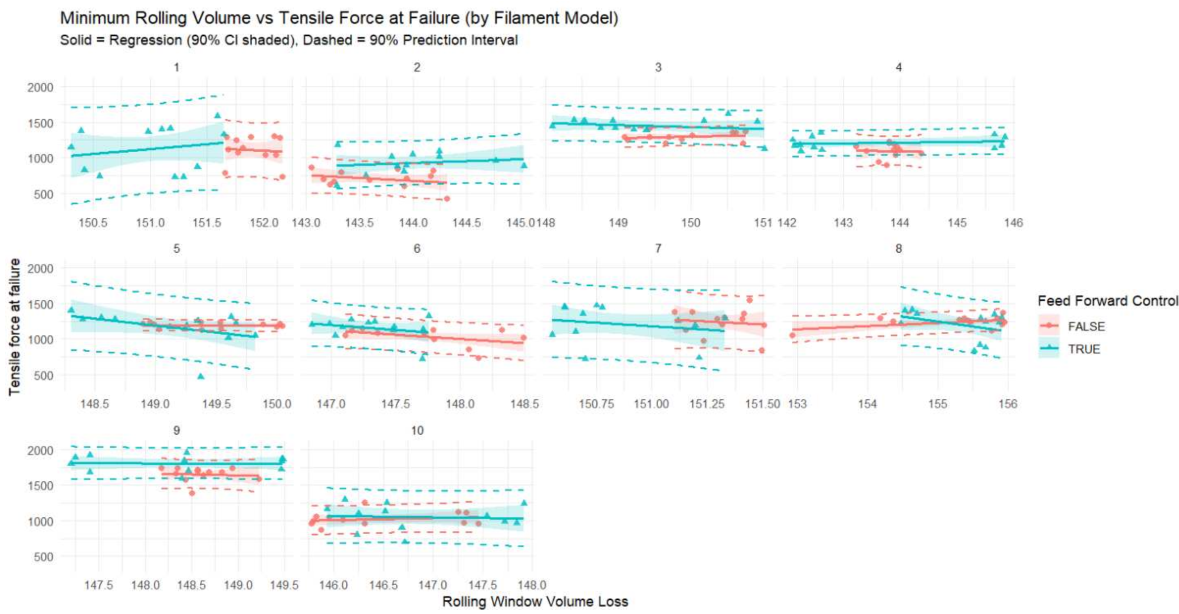

Figure 50-Rolling Volume loss vs Tensile force by filament model

2.8.4 Relationship Between Fracture Location and Minimum Rolling Volume

Figure 51 presents the percentage of tensile coupons, grouped by filament model, for which the measured fracture height corresponds (within ±2%) to the height at which minimum rolling volume occurred during printing. This analysis evaluates whether localized reductions in filament volume directly correspond to the location of tensile failure.

The y-axis represents the percentage of coupons per filament model that exhibit this positional match. Most filament models show low correspondence (0–4.2%), while two models exhibit higher correspondence (~12.5%).

Overall, the percentage of coupons where fracture location aligns with the minimum rolling volume position is relatively low across the dataset.

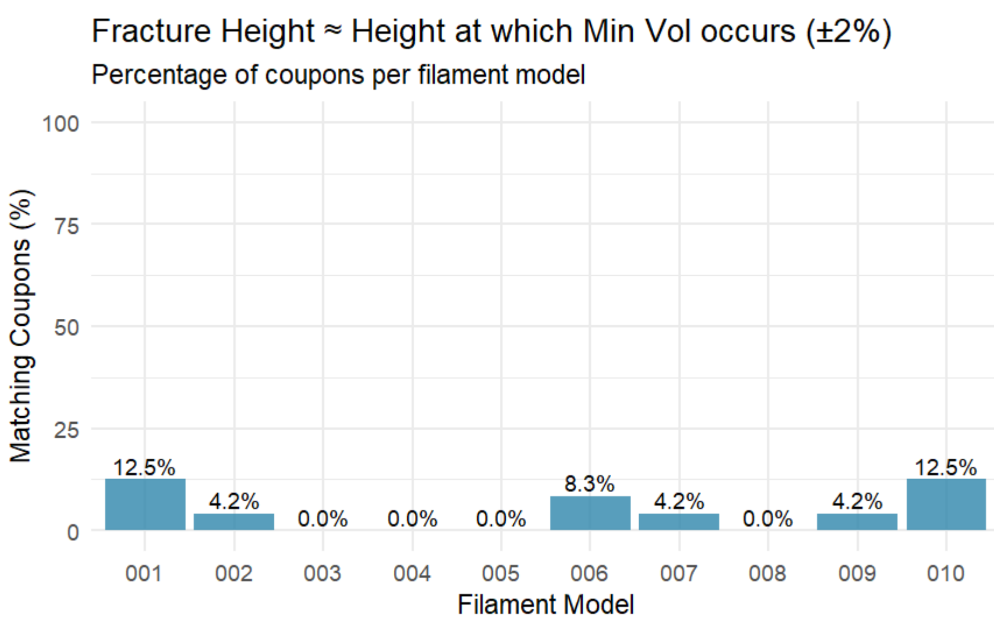

Figure 51- Actual Fracture height matched with layer height that had minimum volume

Cross-Metric Relationships (Colored by FFC Condition)

Figure 52 presents the pairwise relationships between three key metrics used in this study: rolling window volume loss, pressure decay slope, and tube weight, with the data colored by FFC condition. The plot is arranged as a correlation matrix, where each panel represents the relationship between two variables.

The diagonal panels display statistical density distributions for each individual variable, showing the overall distribution of volume loss, pressure decay slope, and tube weight within the dataset.

The density curves are colored according to the FFC condition to visualize differences in the distribution of measurements between prints performed with FFC OFF and FFC ON.

The lower triangular panels show scatter plots representing pairwise relationships between the variables. Each point corresponds to an individual printed tube. The horizontal and vertical axes represent the two variables being compared, while the point color indicates whether the tube was printed with FFC enabled or disabled.

The upper triangular panels display Pearson correlation coefficients summarizing the strength of the relationships between each pair of variables. Correlation values are reported for the entire dataset, as well as separately for FFC OFF and ON conditions. The correlation between rolling volume loss and pressure decay slope is approximately 0.404 for the full dataset, while the correlation between rolling volume loss and tube weight is approximately −0.328. The relationship between pressure decay slope and tube weight shows a correlation of approximately −0.640. Corresponding correlation values are also shown separately for FFC OFF and FFC ON subsets within the matrix.

Together, this matrix provides a compact visualization of the relationships among the three primary metrics used to evaluate printed tube performance and filament volumetric variation.

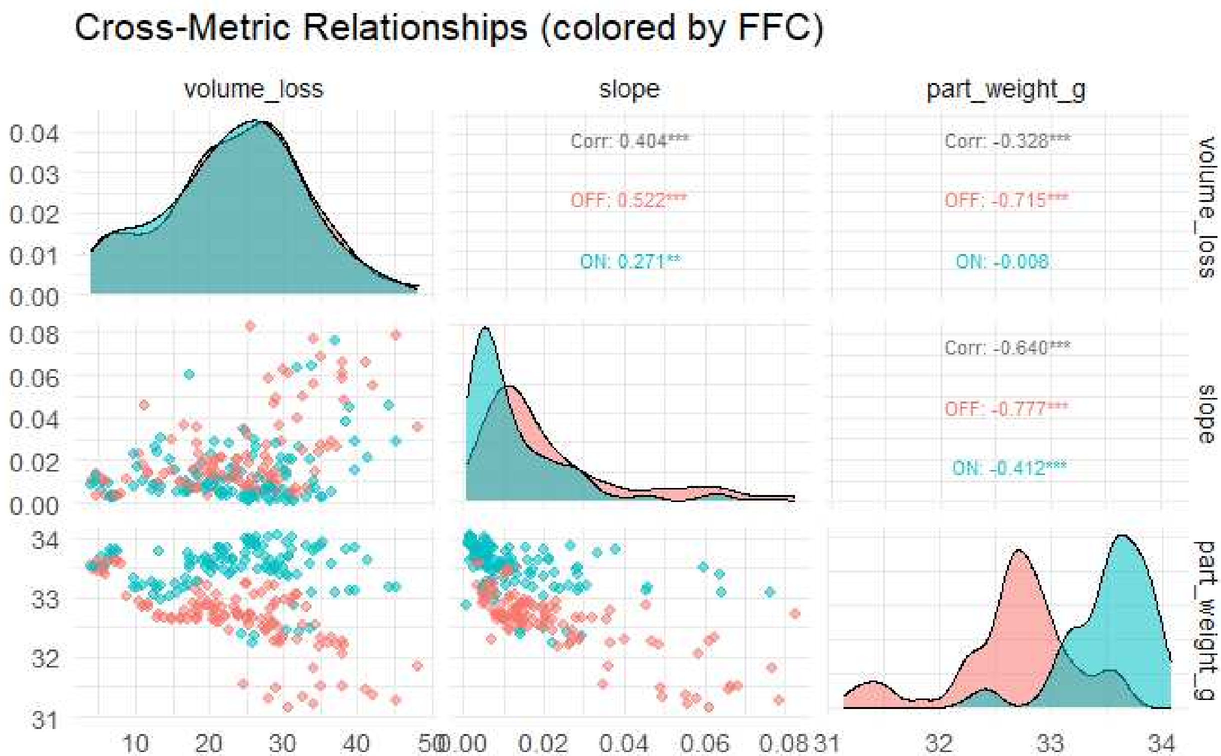

Figure 52- Cross Metric Relationships to evaluate pressure tube performance

3 CHAPTER 3- DISCUSSION

3.1 Influence of Filament Geometry on Print Quality

One of the primary objectives of this study was to investigate the influence of filament dimensional variability on the structural integrity of parts produced through melt extrusion additive manufacturing. The results presented in Chapter 2 demonstrate that measurable differences in filament geometry exist between commercial filament models and that these differences have a direct influence on both pressure retention, as a surrogate for interlayer bonding strength, and tensile performance of printed parts.

The diameter distribution plots (Fig. 21 & Fig. 34) reveal that although most filaments are centered near the nominal diameter of 1.75 mm, the spread and shape of the distributions vary considerably between vendors. Some filament models exhibit narrow distributions tightly clustered around the nominal diameter, while others display broader distributions or multi-modal behavior with mostly below 1.75mm. These differences indicate variation in manufacturing consistency between filament suppliers.

Filament diameter variability has a direct influence on volumetric extrusion during printing which affects road bonding and structural integrity. In conventional fused deposition modeling systems, extrusion is typically controlled by commanding a fixed filament feed rate based on the assumption of a constant filament diameter. Volumetric flow of material entering the melt zone is proportional to the filament cross-sectional area, which varies with the square of the radius. Even relatively small deviations in diameter therefore produce significant changes in volumetric flow.

For example, a deviation of ±0.05 mm around the nominal 1.75 mm diameter produces approximately a ±6 % change in cross-sectional area. Such variations lead to localized under- or over-extrusion events during printing. Under-extrusion is particularly detrimental because insufficient material deposition reduces the bonding area between adjacent roads and layers, creating voids within the printed structure. These voids reduce the mechanical strength of the printed part.

The observed differences in diameter distributions therefore represent an important source of variability in melt-extrusion printing and help explain the variation in part performance observed across the filament models tested in this study.

3.2 Effect of Feed forward Control on Volumetric Deposition

One of the central goals of this research was to evaluate the effectiveness of a feed forward control (FFC) system designed to compensate for filament diameter variations in real time. The results show that enabling the FFC system consistently improves print quality metrics across nearly all filament models tested.

The pressure decay results (Fig. 23 & Fig. 28) demonstrate that parts printed with feed forward control exhibit lower decay slopes compared to parts printed without FFC. Lower decay slopes indicate improved pressure retention, which suggests improved interlayer road bonding and/or a reduction in internal porosity within the walls of printed test tubes. Since pressure decay in this experimental setup primarily occurs through microscopic leakage pathways within the printed structure, improved pressure retention implies that the printed parts are denser and contain fewer internal voids.

The improvement in pressure retention observed with feed forward control can be explained by the system’s ability to compensate for diameter fluctuations before the filament enters the extruder. By measuring filament diameter in real time and adjusting the extruder feed rate accordingly, the system maintains a more consistent volumetric flow into the melt zone. This compensation reduces the formation of porosity and gaps between deposited roads caused by inconsistent filament diameter, which would otherwise lead to leakage paths.

While interlayer bonding is also influenced by thermal history during deposition, the improvements observed for pressure tubes are more directly associated with the reduction in geometry related defects, rather than changes in thermal bonding behavior. This is supported by the observed statistical reduction in pressure decay rates with FFC, which directly reflects decreased leakage through voids and gaps.

Interestingly, the magnitude of improvement provided by FFC varies between filament models (Fig. 23). Filaments exhibiting greater diameter variability tend to show larger improvements when feed forward control is enabled. There was larger variation to correct, and it was indeed corrected. In contrast, filaments with relatively consistent diameter distributions show smaller differences between controlled and uncontrolled prints. This observation suggests that the primary benefit of feed forward control arises from its ability to mitigate the effects of filament variability rather than from altering the baseline printing conditions.

These findings indicate that feed forward control significantly reduces the effect filament manufacturing consistency has on print quality. In practical terms, this means that printers equipped with such a system may achieve more reliable performance across a wider range of commercially available filaments.

3.3 Relationship Between Material Deposition and Pressure Retention

The relationship between tube weight and pressure decay rate provides further insight into the mechanisms governing part performance. The scatter plot (Fig. 25) comparing these two metrics reveals a strong negative correlation between tube weight and pressure decay slope. Tubes with higher mass tend to exhibit lower decay rates, indicating improved pressure retention. The observed increase in pressure tube weight with FFC highlights the role of feed forward control in improving volumetric consistency during extrusion. In the absence of FFC, variations in filament diameter led to fluctuations in deposited material, often resulting in under-extrusion and reduced part mass. The implementation of FFC mitigates these effects by dynamically adjusting the extruder feed rate, ensuring that the intended material volume is deposited.

Notably, the statistically significant increase (Table 5 & 6) in tube weight is observed across all filament models, including those that already exhibit relatively consistent pressure decay behavior. This indicates that FFC not only corrects large volumetric deviations in lower-quality filaments but also reduces subtle inconsistencies in higher-quality filaments. As a result, FFC improves overall deposition uniformity across the entire dataset.

Additionally, the relationship between tube weight and pressure decay suggests that increased material deposition contributes to improved sealing performance by reducing internal voids and enhancing interlayer bonding.

This relationship can be interpreted in terms of material deposition during printing. Tube weight serves as a proxy for the total amount of material extruded during fabrication. If under-extrusion occurs due to reduced filament diameter, the printed tube will contain less material than intended, resulting in a lower overall weight. Reduced material deposition leads to increased porosity and weaker bonding between adjacent roads, creating pathways for air leakage during pressure testing.

The correlation (r = -0.64) observed between tube weight and pressure decay slope therefore reinforces the conclusion that volumetric extrusion consistency is a key determinant of print quality in melt-extrusion processes.

Feed forward control contributes to this effect by increasing the effective material deposition when filament diameter falls below nominal. The weight measurements presented in the results section (Fig. 24 & Fig. 29) show that tubes printed with feed forward control exhibit slightly higher mass than those printed without control. Although the absolute increase in mass is relatively small, even modest increases in deposited material can significantly reduce internal porosity.

3.4 Influence of Filament Diameter Distribution on Part Performance

The heatmap style visualizations (Fig. 26, Fig. 27, Fig. 35) of diameter distributions provide a compact representation of how filament geometry differs between vendors and how these differences relate to print performance metrics. When filament models are ordered according to tube weight or pressure decay rate, patterns emerge in the distribution of diameter measurements. Higher performing filament models (i.e., those exhibiting lower pressure decay rates and higher tensile force at failure, example: filament models 1, 8, & 9) tend to exhibit a large proportion of diameter measurements concentrated within the bins near the nominal diameter (1.75 mm). These filaments show relatively narrow distributions and minimal occurrence of extreme diameter values. In contrast, lower-performing filament models often display wider distributions with a greater percentage of measurements falling into bins corresponding to smaller diameters.

The presence of lower diameter regions within the filament spool is particularly significant because these regions produce localized reductions in volumetric extrusion during printing. Even if the average filament diameter is close to the nominal value, localized thinner sections can lead to transient under-extrusion events that create defects within the printed part. These defects may propagate through multiple layers, probably affecting the overall density and of the component. The heatmap visualizations therefore highlight the importance of not only the mean filament diameter but also the distribution and frequency of diameter deviations. Filaments with diameters nearer to 1.75mm are more likely to produce reliable print outcomes, while filaments with larger variability introduce greater uncertainty into the extrusion process.

An additional observation from the statistical analysis (Table 2 & 3) is that the improvement due to feed forward control is not limited to filament models with poor baseline performance. While filament models with higher pressure decay rates, such as models 2 and 4, show expected improvements with FFC ON, statistically significant improvements are also observed in filament models that already exhibit low decay rates, such as models 7 and 9. This suggests that FFC does not merely correct large volumetric errors, but also enhances deposition consistency by mitigating smaller diameter fluctuations. As a result, FFC improves both defect-prone and already high-performing filaments, indicating a broader impact on overall process stability rather than a targeted correction mechanism.

Figure 45 shows pressure decay rate as a function of dominant area band, expressed as a percentage of the nominal cross-sectional area (2.40 mm^2 corresponding to a 1.75 mm diameter filament). A clear trend showing tubes whose dominant deposited area is closer to 100% of the nominal value exhibit substantially lower pressure decay rates. Tubes with a dominant area band near 90% demonstrate the highest median decay and the largest spread, indicating greater structural variability and increased leakage. At 95%, both the median decay rate and variability decrease, while the 100% band shows the lowest decay values and the most compact distribution. This trend suggests that sustained deposition near the ideal cross-sectional area reduces internal void formation, thereby enhancing airtightness. The result provides strong evidence that volumetric consistency plays a p role in governing pressure retention, motivating the subsequent rolling volume loss analysis.

3.5 Localized Volumetric Variation and Pressure Decay

A key aspect of this study was the use of a rolling volumetric window to quantify localized filament volume variation along the filament length. This approach differs from traditional diameter analysis because it captures the cumulative effect of cross-sectional variations over a defined segment of filament rather than evaluating individual diameter measurements in isolation.

The results (Fig. 47 & Fig. 48) show a clear relationship between rolling volume loss and pressure decay rate. As the magnitude of volume loss within the rolling window increases, the pressure decay slope also increases, indicating reduced pressure retention. This finding supports the hypothesis that localized filament defects can produce structural weaknesses in the printed part.

The rolling window method effectively captures the presence of thinner filament segments, which reduces the amount of material available for extrusion within a particular portion of the build. If such a defect occurs while printing a critical region of the part, it may introduce a localized volume of reduced density that later can be a leakage pathway during pressure testing. Importantly, this relationship persists across different filament models and printing conditions, suggesting that rolling volume loss may serve as a useful predictive metric for identifying potential build defects. Compared with instantaneous diameter measurements, the rolling volume metric provides a more physically meaningful representation of how filament variability influences material deposition during printing.

3.6 Tensile Failure Location, Rolling Volume Effects, and Mechanical Implications

While feed forward control (FFC) demonstrated consistent improvements in median tensile force at failure across most filament models, the fracture location analysis provides additional insight into the mechanisms governing tensile behavior.

3.7 Fracture Height Distribution and Effect of FFC

The histogram of fracture height from the bottom of the coupon (Fig.40) shows that fractures occur throughout the gauge length in both FFC OFF and FFC ON conditions. Although slight differences in mean and median fracture height are visible between the two groups, the overall distribution remains broad in both cases. No dominant fracture height is observed in either condition.

This indicates that feed forward control has little to no systematic effect on where a tensile coupon fractures. While FFC improves overall tensile strength, it does not appear to localize or redistribute failure to a specific region within the gauge section. This behavior was not initially expected, as it was hypothesized that tensile failure would preferentially occur near the mid-gauge region, where reductions in cross-sectional area would lead to higher local stresses. This observation suggests that tensile failure is not governed by a single predictable geometric defect location but rather by distributed structural characteristics throughout the printed gauge length. Visual inspection (Fig.41 & Fig.42) of fractured coupons further supports this conclusion. All coupons exhibited relatively flat fracture surfaces with no evidence of shear-dominated failure. If failure were dominated by geometric defects, fracture surfaces would be expected to exhibit more irregular features, such as shear-dominated fracture planes, localized necking at distinct defect sites. The absence of such features in the observed coupons supports the conclusion that failure is governed primarily by interlayer bonding rather than localized geometric defects.

3.7.1 Fracture Height vs Minimum Rolling Volume

To investigate whether localized filament volume reduction directly determines fracture initiation, fracture height was compared with the height at which minimum rolling filament volume occurred during printing (within ±2% tolerance) (Fig. 49 & Fig.51).

The percentage of coupons per filament model exhibiting this positional match is relatively low (0–12.5% across models). Most filament models show little to no alignment between fracture height and minimum rolling volume location. This result indicates that localized thin filament segments, while important for pressure retention performance, do not consistently dictate tensile fracture location.

This distinction is important because pressure decay testing and tensile testing show different sensitivities:

- Pressure tubes are highly sensitive to localized porosity. Even a small segment with thinner filament can produce a leakage pathway.
- Tensile coupons experience distributed axial stress across the cross-section. Failure initiation depends on the lowest stress concentration, which may arise from multiple interacting microstructural features rather than a single volumetric defect.

Thus, while rolling volume loss strongly correlates with pressure decay slope, tensile fracture is influenced by more complex and distributed bonding behavior.

3.7.2 Influence of Tensile Test Jaw Preload and Fracture

It must also be noted that tensile coupons were gripped using mechanical wedge jaws that required preload forces of approximately 30–40 N to prevent slippage during testing.

In some coupons, fracture occurred outside the nominal gauge section. Such failures may be attributed to:

- Local stress concentrations introduced by jaw clamping pressure
- Micro-cracking induced during tightening
- Slight misalignment during gripping
- Surface indentation from jaw teeth

Although care was taken to maintain consistent gripping procedures, the preload necessary to prevent slippage could have influenced the fracture location in some tests. Therefore, not all fracture positions should be interpreted purely as material-driven phenomena.

This mechanical boundary condition is an important experimental consideration when analyzing fracture height distribution.

3.8 Effect of Build Number and Print Location on Tensile Performance

In addition to evaluating the influence of feed forward control and filament geometry, tensile performance was analyzed as a function of build number and coupon location on the build platform (Fig. 38 & Fig.39). Each build number represents a distinct print run under nominally identical conditions.

The grouped boxplots of tensile force failure by build number show minimal variation between successive builds. Median forces remain relatively stable across builds, and no systematic drift in tensile strength was observed over time.

Similarly, analysis of tensile force by bed location (A–D) reveals limited variation between build positions on the platform. While minor differences in median force are present between locations, these differences are small relative to the overall spread of tensile values and do not follow a consistent directional trend. Statistical analysis confirms that neither build number ($p = 0.753$) nor build platform location ($p = 0.444$) has a significant effect on tensile force. This indicates that the observed variability in tensile performance cannot be attributed to build to build differences or spatial variation on the build platform.

In other words, tensile variability observed between filament models cannot be attributed to build sequence or build platform location.

3.9 Why FFC Has a Limited Effect on Fracture Location

Although FFC improves overall tensile strength, it has limited observable influence on the vertical distribution of fracture locations. This suggests that filament diameter–induced volumetric variation is not the sole governing factor determining where failure initiates during tensile loading. While FFC reduces under- and over-extrusion events, fracture height appears to be influenced by additional process-dependent mechanisms that operate independently of instantaneous volumetric correction.

One dominant factor is the role of heat transfer in interlayer bonding quality. Bond formation in melt extrusion depends strongly on extrusion temperature, cooling rate, thermal diffusion between adjacent roads, and the duration for which deposited material remains above the glass transition temperature[29], [30], [31]. Even when volumetric deposition is corrected through FFC, insufficient thermal diffusion can limit interlayer fusion strength. As printing progresses, localized temperature variations can arise due to differences in time between successive layer depositions. For example, a region may experience slightly longer cooling before the next layer is deposited due to toolpath sequencing or pauses in motion, resulting in reduced thermal diffusion and weaker interlayer bonding at that location. These gradients can produce variations in bonding quality with height and may contribute to localized mechanical weakness independent of diameter fluctuations.

In addition, microstructural factors such as road alignment, overlap consistency, and minor toolpath deviations influence local stress concentration. Although a randomized Z-concentric infill strategy was employed to maximize strength and reduce directional bias, small variations in road overlap and extrusion stability may still create localized stress intensification zones. Thermal contraction during cooling also induces residual stress that may not spatially correlate with rolling-volume defects. Consequently, fracture location reflects a complex interaction between thermal history, stress evolution, and bonding kinetics rather than solely diameter-driven volumetric inconsistency.

Although FFC does not significantly alter fracture height distribution, it consistently increases the median tensile force at failure across most filament models (Fig. 36). This improvement is likely due to fewer under-extrusion events, more consistent road width, improved contact area between adjacent roads thereby enhancing interlayer fusion.

Taken together, these results indicate that tensile performance in melt-extruded parts is governed primarily by material-dependent interlayer bonding behavior and global extrusion consistency, rather than geometric position, batch variation, or isolated volumetric defects.

3.10 Absence of Significant Thermal Differences (DSC Results)

Differential Scanning Calorimetry (DSC) analysis (Fig. 43 & Fig.44) revealed similar heat flow behavior across the filament models examined. No distinct thermal transitions or crystallization differences were observed that could explain major variations in tensile performance between materials.

While the overall heat flow curve shapes are consistent across filament models, small, localized peaks are observed in certain materials, particularly in filament model 9 (Fig.43). These features may arise from material-specific artifacts, such as additives introduced during manufacturing (e.g., colorants, fillers, or processing stabilizers), which can introduce secondary thermal events. Additionally, moisture absorption prior to testing may contribute to these irregularities, as absorbed moisture can lead to minor endothermic peaks associated with evaporation or plasticization effects. This observation suggests that:

- The primary tensile performance differences between filament models are not due to intrinsic bulk polymer thermal behavior.
- Geometric consistency and processing conditions likely play a more significant role than material chemistry differences within the tested range.

Thus, tensile variability appears to be governed more by process dependent road bonding quality than by inherent polymer thermal transitions.

The fracture location analysis highlights an important conceptual distinction:

- Pressure decay is highly sensitive to localized porosity.
- Tensile strength reflects interlayer bonding strength.

Rolling volume loss is therefore a strong predictor of leakage performance but cannot predict the fracture initiation location.

This distinction strengthens the overall conclusions of this study by demonstrating that volumetric consistency influences multiple performance metrics differently depending on the loading mode.

3.11 Influence of Printer and Environmental Conditions

The use of two printers for pressure tube fabrication provided an opportunity to evaluate potential machine to machine variability (Fig.30 & Fig.31). The results indicate that while slight differences exist between printers, the overall trends remain consistent across both machines. Feed forward control reduces pressure decay slopes on both printers, suggesting that the effectiveness of the control system is not strongly dependent on the specific hardware configuration.

Environmental conditions such as ambient temperature and humidity were monitored during printing (Fig. 32 & Fig. 33). The recorded temperature ranged from approximately 23–27 °C, while humidity remained between 25% and 40%. Although these ranges may appear broad in absolute terms, they are relatively narrow compared to the thermal conditions experienced during melt extrusion, where material temperatures exceed 200 °C. Literature has shown that filaments stored in high humidity zone (>75% RH) has led to a decline in mechanical performance of the printed part[32]. These observations suggest that the variations in pressure decay and tensile strength are primarily driven by filament geometry and extrusion behavior rather than by external environmental conditions.

3.12 Relationship Between Filament Price and Geometric Quality

An additional analysis examined the relationship between filament ovality and market price (Fig. 46). The results show only a moderate correlation between these two variables ($r = 0.409$), indicating that higher filament cost does not necessarily correspond to improved geometric consistency.

This finding has important practical implications for users of melt extrusion printers. While premium filaments are marketed as offering superior quality, the data suggests that price alone is not a reliable indicator of filament dimensional stability. Some lower-cost filaments demonstrate geometric consistency comparable to that of more expensive materials, while certain higher-priced filaments exhibit relatively large diameter variability.

Consequently, direct measurement of filament geometry may provide a more reliable assessment of material quality than price or vendor reputation alone.

4 CHAPTER 4 - CONCLUSION

4.1 Overview

This thesis investigated the influence of filament geometric variability on part performance in melt-extrusion additive manufacturing and evaluated the effectiveness of a real-time feed forward control (FFC) system designed to compensate for filament diameter variations.
Across ten commercial filament models, 240 pressure tubes and 240 tensile coupons were fabricated and evaluated using pressure decay testing, tensile testing, dual-sensor diameter monitoring, rolling volumetric analysis, and thermal characterization. The results collectively provide insight into how filament geometry affects print quality and how real-time volumetric compensation improves structural reliability.

4.2 Influence of Feed forward Control on Extrusion Uniformity and Leakage

The first objective of this work was to quantify how feed forward control influences extrusion uniformity and pressure tube leakage.
The implementation of dual orthogonal diameter sensing allowed real-time adjustment of extruder feed rate to compensate for filament diameter fluctuations. This compensation reduced under-extrusion events caused by localized thin filament segments and produced denser printed structures with fewer internal leakage pathways.
The results demonstrate that enabling FFC consistently increases deposited material mass and reduces pressure decay slope across nearly all filament models and across both printers used in the study. Reduced pressure decay slope represented improved interlayer bonding quality, with pressure retention serving as our measurable surrogate for this mechanical characteristic.
Improved interlayer road bonding quality directly reduces the formation of internal leakage

pathways, as stronger bonds between adjacent roads leave fewer voids through which pressurized air can escape. Tube weight exhibited a strong negative correlation with pressure decay slope, confirming that improved volumetric deposition directly enhances pressure retention performance.

Thus, feed forward control measurably improves extrusion uniformity and significantly reduces pressure tube leakage. Since no alternative mechanism was identified that could improve pressure retention independently of interlayer road bonding quality in this experimental context, the two are treated as directly linked throughout this work.

4.3 Sensitivity of Pressure Decay to Geometric Variability

The second objective was to determine whether FFC reduces the sensitivity of pressure decay behavior to geometric variability.

Rolling volume loss, calculated using a moving window along the filament path, emerged as a strong predictor of pressure decay slope. Larger localized volumetric deficits were associated with higher leakage rates, confirming that transient filament thin sections can propagate into structural defects.

However, when FFC was enabled, the magnitude of performance degradation associated with volumetric variation was reduced. Filament models exhibiting greater diameter variability showed the largest improvements under FFC. This indicates that the control system effectively reduces the impact of geometric inconsistency on part performance.

Therefore, FFC decreases the dependence of pressure retention on filament dimensional stability and increases part quality against material variability.

4.4 Effect of FFC on Tensile Performance Across Filament Models

third objective was to evaluate the extent to which FFC affects tensile performance. Following the rationale that increased pressure retention represented increased interlayer road bonding quality, we hypothesized that this would in turn increase tensile strength.

Across most filament models, feed forward control increased median tensile force at failure. The global tensile population exhibited a higher median tensile force at failure under FFC ON (1229 N) compared to FFC OFF (1157 N) conditions. This improvement reflects enhanced volumetric consistency, which reduces under-extrusion events and increases the contact area between adjacent roads, thereby improving interlayer bonding quality and raising the force required to cause tensile failure.

In other words, more consistent volumetric deposition leads to improved interlayer bonding, and improved interlayer bonding raises the tensile force at failure.

However, fracture height analysis revealed that FFC had minimal influence on where tensile coupons fractured. Fractures were distributed throughout the gauge section in both [DP89.1]FFC on and FFC off states. Furthermore, fracture height rarely aligned with the position of minimum rolling volume along the filament path.

These findings indicate that tensile failure is governed by distributed bonding characteristics rather than isolated localized dimensional or volumetric defects. While FFC improves global structural integrity, tensile fracture remains influenced by additional factors including:

- **Thermal interlayer diffusion** - insufficient thermal energy transfer between newly deposited and previously solidified layers limits polymer chain interdiffusion, reducing bond strength at those interfaces regardless of volumetric consistency.

- **Cooling rate variations along build height** - as part height increases, the time between successive layer depositions changes, altering how long material remains above the glass transition temperature and therefore how effectively adjacent layers fuse.
- **Residual stress** - differential thermal contraction during cooling introduces internal stresses distributed throughout the gauge length, which can act as initiation sites for fracture independently of where filament diameter variations occurred.
- **Road to road bonding variability** - minor deviations in road overlap, toolpath sequencing, and extrusion stability create localized differences in contact area and bonding quality between adjacent roads that are not captured by the rolling volume metric alone.

Additionally, tensile coupons were gripped using wedge jaws requiring 30–40 N preload to prevent slippage. This preload may have introduced local stress concentrations near the grip interface, contributing to occasional fractures outside the nominal gauge length.

Therefore, FFC enhances tensile strength but does not fundamentally alter fracture localization behavior.

4.5 Correlation of Filament Properties with Part Quality

The fourth objective was to assess whether filament dimensional properties (diameter, ovality, volume), and cost correlate with pressure decay or tensile outcomes.

Diameter stability showed strong correlation with pressure decay behavior. Rolling volumetric loss proved to be a more meaningful predictor of leakage performance than instantaneous diameter measurements alone. This confirms that cumulative volumetric consistency over a defined filament length is critical for good road binding, especially in pressure-sensitive applications.

Filament price did not reliably predict geometric stability or mechanical performance. Some lower cost filaments demonstrated comparable or better performance than higher-priced materials, indicating that cost alone is not a reliable indicator of quality.

Differential Scanning Calorimetry (DSC) analysis revealed no significant differences in thermal transition behavior between selected filament models. This suggests that variations in tensile performance are not driven by intrinsic polymer thermal properties but rather by geometric and process related factors.

It should also be noted that DSC may lack the sensitivity required to detect subtle compositional differences between PETG formulations from different vendors, particularly when variations arise from minor additive concentrations such as colorants or processing stabilizers rather than differences in bulk polymer structure. The absence of observable thermal differences should therefore be interpreted as a limitation of the characterization method as much as evidence of material homogeneity.

Taken together, these findings suggest that geometric consistency is the dominant controllable variable influencing print quality within the range of commercially available PETG filaments tested, and that feed forward control is an effective means of compensating for its variability at the point of deposition

factors.

4.6 Key Contributions

This work makes several important contributions to the field of melt-extrusion additive manufacturing:

1. Comprehensive Large-Scale Validation

   A dataset of 480 printed specimens across ten filament models provides robust experimental evidence linking filament geometry to structural performance.

2. Real-Time Dual-Sensor Feed forward Compensation

   A deployable feed forward control architecture integrated with open-source firmware demonstrates a practical solution to filament diameter variability.

3. Rolling Volumetric Defect Metric

   The introduction of rolling volume loss as a predictive metric provides mechanistic understanding of how localized geometric variation affects leakage performance.

4. Differentiation Between Pressure and Tensile Mechanisms

   The distinction between localized defect sensitivity (pressure decay) and distributed bonding behavior (tensile failure) advances understanding of performance metrics in extrusion-based printing.

5 REFERENCES

[1] T. T. Wohlers, I. Campbell, O. Diegel, R. Huff, J. Kowan, and Wohlers Associates (firm), “Wohlers Report: 3D Printing and Additive Manufacturing Global State of the Industry,” Wohlers Associates, Fort Collins, Colorado, USA, Additive Manufacturing Industry Report 2022, 2022. [Online]. Available: https://wohlersassociates.com/2022report.htm

[2] I. Gibson, D. Rosen, and B. Stucker, *Additive Manufacturing Technologies: 3D Printing, Rapid Prototyping, and Direct Digital Manufacturing*, 2nd ed. 2015. in SpringerLink Bücher. New York, NY: Springer, 2015. doi: 10.1007/978-1-4939-2113-3.

[3] T. D. Ngo, A. Kashani, G. Imbalzano, K. T. Q. Nguyen, and D. Hui, “Additive manufacturing (3D printing): A review of materials, methods, applications and challenges,” *Composites Part B: Engineering*, vol. 143, pp. 172–196, Jun. 2018, doi: 10.1016/j.compositesb.2018.02.012.

[4] B. Turner, R. Strong, and S. A. Gold, “A review of melt extrusion additive manufacturing processes: I. Process design and modeling,” *Rapid Prototyping Journal*, vol. 20, no. 3, pp. 192–204, Apr. 2014, doi: 10.1108/RPJ-01-2013-0012.

[5] “ISO/ASTM 52900:2021,” ISO. Accessed: Mar. 20, 2026. [Online]. Available: https://www.iso.org/standard/74514.html

[6] S. Ahn, M. Montero, D. Odell, S. Roundy, and P. K. Wright, “Anisotropic material properties of fused deposition modeling ABS,” *Rapid Prototyping Journal*, vol. 8, no. 4, pp. 248–257, Oct. 2002, doi: 10.1108/13552540210441166.

[7] A. K. Sood, R. K. Ohdar, and S. S. Mahapatra, “Parametric appraisal of mechanical property of fused deposition modelling processed parts,” *Materials & Design*, vol. 31, no. 1, pp. 287–295, Jan. 2010, doi: 10.1016/j.matdes.2009.06.016.

[8] B. Rankouhi, S. Javadpour, F. Delfanian, and T. Letcher, “Failure Analysis and Mechanical Characterization of 3D Printed ABS With Respect to Layer Thickness and Orientation,” *J Fail. Anal. and Preven.*, vol. 16, no. 3, pp. 467–481, Jun. 2016, doi: 10.1007/s11668-016-0113-2.

[9] J. Ghorbani, P. Koirala, Y.-L. Shen, and M. Tehrani, “Eliminating voids and reducing mechanical anisotropy in fused filament fabrication parts by adjusting the filament extrusion rate,” *Journal of Manufacturing Processes*, vol. 80, pp. 651–658, Aug. 2022, doi: 10.1016/j.jmapro.2022.06.026.

[10] B. T. Wittbrodt *et al.*, “Life-cycle economic analysis of distributed manufacturing with open-source 3-D printers,” *Mechatronics*, vol. 23, no. 6, pp. 713–726, Sep. 2013, doi: 10.1016/j.mechatronics.2013.06.002.

[11] M. Grasso and B. M. Colosimo, “Process defects and *in situ* monitoring methods in metal powder bed fusion: a review,” *Meas. Sci. Technol.*, vol. 28, no. 4, p. 044005, Apr. 2017, doi: 10.1088/1361-6501/aa5c4f.

[12] S. K. Everton, M. Hirsch, P. Stravroulakis, R. K. Leach, and A. T. Clare, “Review of in-situ process monitoring and in-situ metrology for metal additive manufacturing,” *Materials & Design*, vol. 95, pp. 431–445, Apr. 2016, doi: 10.1016/j.matdes.2016.01.099.
[13] L. Scime and J. Beuth, “Using machine learning to identify in-situ melt pool signatures indicative of flaw formation in a laser powder bed fusion additive manufacturing process,” *Additive Manufacturing*, vol. 25, pp. 151–165, Jan. 2019, doi: 10.1016/j.addma.2018.11.010.
[14] M. Bustos Seibert, G. A. Mazzei Capote, M. Gruber, W. Volk, and T. A. Osswald, “Manufacturing of a PET Filament from Recycled Material for Material Extrusion (MEX),” *Recycling*, vol. 7, no. 5, p. 69, Sep. 2022, doi: 10.3390/recycling7050069.
[15] A. Boschetto and L. Bottini, “Roughness prediction in coupled operations of fused deposition modeling and barrel finishing,” *Journal of Materials Processing Technology*, vol. 219, pp. 181–192, May 2015, doi: 10.1016/j.jmatprotec.2014.12.021.
[16] G. Nyiranzeyimana, J. M. Mutua, B. R. Mose, and T. O. Mbuya, “Optimization of process parameters in fused deposition modelling of thermoplastics: A review,” *Materialwiss. Werkstofftech.*, vol. 52, no. 6, pp. 682–694, Jun. 2021, doi: 10.1002/mawe.202000193.
[17] O. A. Mohamed, S. H. Masood, and J. L. Bhowmik, “Optimization of fused deposition modeling process parameters: a review of current research and future prospects,” *Adv. Manuf.*, vol. 3, no. 1, pp. 42–53, Mar. 2015, doi: 10.1007/s40436-014-0097-7.
[18] V. H. V. Jilludimudi *et al.*, “Non-destructive evaluation of melt-extruded part quality using in situ data,” *Rapid Prototyping Journal*, vol. 30, no. 1, pp. 124–133, Sep. 2023, doi: 10.1108/RPJ-04-2023-0122.
[19] T. A. Sanladerer, “InFiDEL - Inline Filament Diameter Estimator,” https://github.com/drspangle/infidel-sensor. [Online]. Available: https://github.com/drspangle/infidel-sensor
[20] M. Spoerk, J. Gonzalez-Gutierrez, J. Sapkota, S. Schuschnigg, and C. Holzer, “Effect of the printing bed temperature on the adhesion of parts produced by fused filament fabrication,” *Plastics, Rubber and Composites*, vol. 47, no. 1, pp. 17–24, Jan. 2018, doi: 10.1080/14658011.2017.1399531.
[21] Colorado State University School of Advanced Materials Discovery Core Facility, “Colorado State University School of Advanced Materials Discovery Core Facility,” SciCrunch Registry. [Online]. Available: https://www.research.colostate.edu/samdcore/
[22] D20 Committee, *Test Method for Tensile Properties of Plastics*. doi: 10.1520/D0638-14.
[23] Colorado State University Analytical Resources Core Facility, “Colorado State University Analytical Resources Core Facility,” SciCrunch Registry. [Online]. Available: https://www.research.colostate.edu/arc/
[24] M. Domingo-Espin, J. M. Puigoriol-Forcada, A.-A. Garcia-Granada, J. Llumà, S. Borros, and G. Reyes, “Mechanical property characterization and simulation of fused deposition modeling Polycarbonate parts,” *Materials & Design*, vol. 83, pp. 670–677, Oct. 2015, doi: 10.1016/j.matdes.2015.06.074.
[25] A. R. Torrado, C. M. Shemelya, J. D. English, Y. Lin, R. B. Wicker, and D. A. Roberson, “Characterizing the effect of additives to ABS on the mechanical property anisotropy of specimens fabricated by material extrusion 3D printing,” *Additive Manufacturing*, vol. 6, pp. 16–29, Apr. 2015, doi: 10.1016/j.addma.2015.02.001.
[26] K. A. Martin, T. L. Thornell, H. A. Hanna, C. A. Weiss Jr., and Z. B. McClelland, “Effect of Filament Color and Fused Deposition Modeling/Fused Filament Fabrication Process on

the Development of Bistability in Switchable Bistable Squares," *ASME Open J. Engineering*, vol. 3, no. 031002, Jan. 2024, doi: 10.1115/1.4064142.

[27] T. D. McLouth, J. V. Severino, P. M. Adams, D. N. Patel, and R. J. Zaldivar, "The impact of print orientation and raster pattern on fracture toughness in additively manufactured ABS," *Additive Manufacturing*, vol. 18, pp. 103–109, Dec. 2017, doi: 10.1016/j.addma.2017.09.003.

[28] J. P. Harmon, "Thermal Analysis of Polymeric Materials By Bernhard Wunderlich (Knoxville, TN). Springer: Berlin, Heidelberg, New York. 2005. xvi + 894 pp. $89.95. ISBN 3-540-23629-5.," *J. Am. Chem. Soc.*, vol. 127, no. 42, pp. 14952–14952, Oct. 2005, doi: 10.1021/ja059803i.

[29] C. Bellehumeur, L. Li, Q. Sun, and P. Gu, "Modeling of Bond Formation Between Polymer Filaments in the Fused Deposition Modeling Process," *Journal of Manufacturing Processes*, vol. 6, no. 2, pp. 170–178, 2004, doi: 10.1016/S1526-6125(04)70071-7.

[30] J. E. Seppala, S. Hoon Han, K. E. Hillgartner, C. S. Davis, and K. B. Migler, "Weld formation during material extrusion additive manufacturing," *Soft Matter*, vol. 13, no. 38, Art. no. 38, 2017, doi: 10.1039/C7SM00950J.

[31] T. J. Coogan and D. O. Kazmer, "Prediction of interlayer strength in material extrusion additive manufacturing," *Additive Manufacturing*, vol. 35, p. 101368, Oct. 2020, doi: 10.1016/j.addma.2020.101368.

[32] L. Lendvai, I. Fekete, S. K. Jakab, G. Szarka, K. Verebélyi, and B. Iván, "Influence of environmental humidity during filament storage on the structural and mechanical properties of material extrusion 3D-printed poly(lactic acid) parts," *Results in Engineering*, vol. 24, p. 103013, Dec. 2024, doi: 10.1016/j.rineng.2024.103013.

6 APPENDIX

APPENDIX A: Pressure testing Protocol

APPENDIX B: Tensile testing Protocol

6.1 Appendix A

6.1.1 **Pressure Testing Protocol**:

The apparatus has the following components:

Figure 53-Pressure testing Apparatus

Mechanical Components:

- Compressor: A compressor that can pressurize up to 50Psi
- ¼" Compressed Air-Filter regulator
- ¼ x 4in long Brass Nipple fitting
- ¼" Flow controller
- ¼" x 2in Brass Nipple fitting
- 1/4" Full port ball valve
- ¼" x 1" Pipe adapter (2nos)
- 1" Tee fitting

- 1” x 6” Brass MIP Nipple fitting
- 1” to ½” Reducer

Electrical Components:

- Pressure sensor
- Oscilloscope: To supply 24 VDC to the DAQ
- National Instruments 9203 cDAQ card for pressure sensor
- National Instruments cDAQ-9714 Card Holder (Can be swapped with any compatible cDAQ carrier)

Tools and Supplies needed:

- Pipe Wrench
- Teflon Tapes
- Molykote 111
- Large Adjustable Wrench

Assembly flow:

1) Connect the Compressor to the Pressure regulator with Teflon tape around the connection
2) Have the Pressure regulator connected to the flow controller with the ¼ x 4in long Brass Nipple fitting. Make sure to properly use Teflon tapes around the fitting
3) Connect it to the ball valve via the ¼ x 2in Brass Nipple fitting, with proper use of Teflon tapes around it.
4) To one end of the Tee nut, screw in the ¼’ x 1” pipe adapter and connect it to the nipple fitting coming out of the ball valve as below:

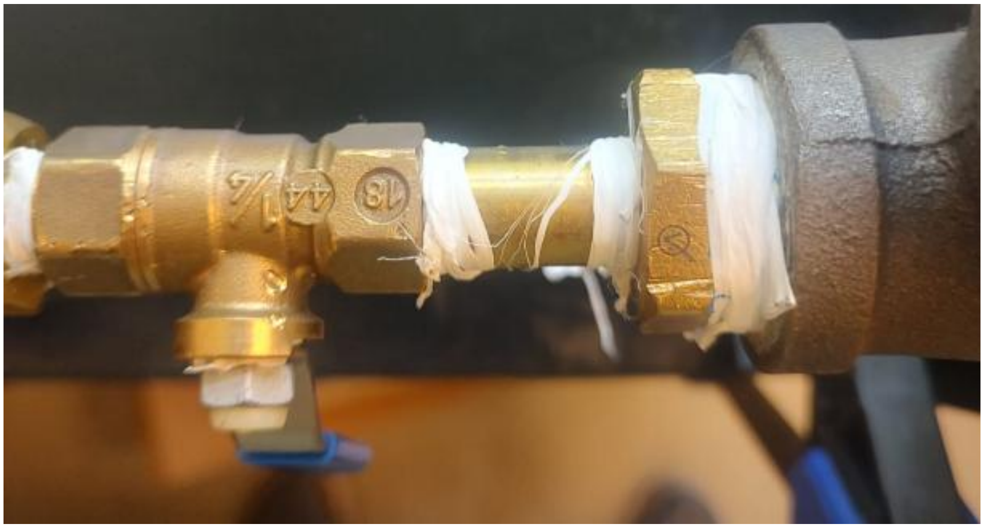

Figure 54- Connection too TEE from ball valve

5) Next connect the vertical Tee to the 1” x 6” Brass MIP Nipple fitting, on top of which screw the 1” to ½” Reducer. Make sure to have proper usage of Teflon tapes while connecting/screwing brass nipples and fittings
6) To the only open end of the Tee fitting, screw another ¼’ x 1” pipe adapter , to which the pressure sensor will be connected to.
7) This pressure sensor will be connected to the DAQ, that will be powered by a 24 VDC through an oscilloscope.

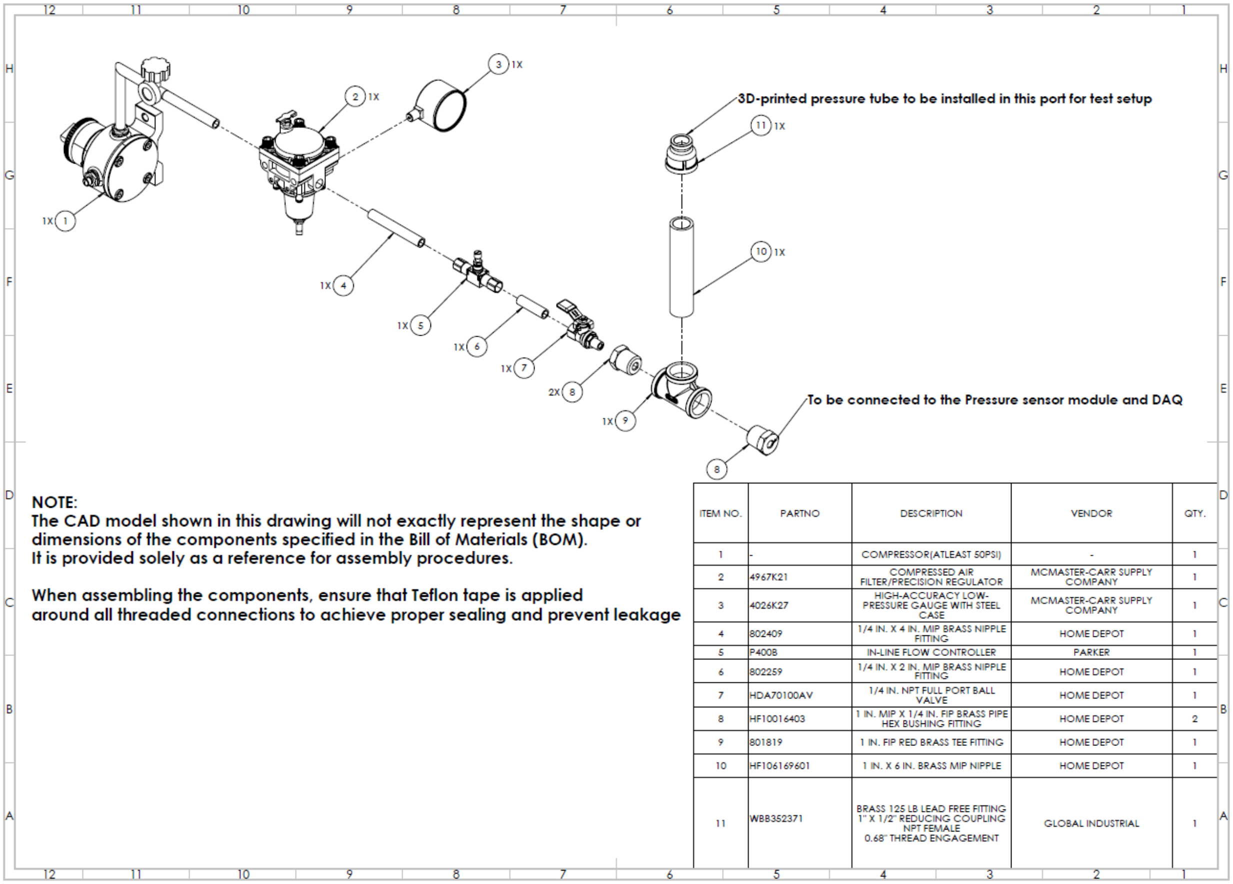

ITEM NO.	PARTNO	DESCRIPTION	VENDOR	QTY.
1	-	COMPRESSOR(ATLEAST 50PSI)	-	1
2	4967K21	COMPRESSED AIR FILTER/PRECISION REGULATOR	MCMASTER-CARR SUPPLY COMPANY	1
3	4026K27	HIGH-ACCURACY LOW-PRESSURE GAUGE WITH STEEL CASE	MCMASTER-CARR SUPPLY COMPANY	1
4	802409	1/4 IN. X 4 IN. MIP BRASS NIPPLE FITTING	HOME DEPOT	1
5	P400B	IN-LINE FLOW CONTROLLER	PARKER	1
6	802259	1/4 IN. X 2 IN. MIP BRASS NIPPLE FITTING	HOME DEPOT	1
7	HDA70100AV	1/4 IN. NPT FULL PORT BALL VALVE	HOME DEPOT	1
8	HF10016403	1 IN. MIP X 1/4 IN. FIP BRASS PIPE HEX BUSHING FITTING	HOME DEPOT	2
9	801819	1 IN. FIP RED BRASS TEE FITTING	HOME DEPOT	1
10	HF106169601	1 IN. X 6 IN. BRASS MIP NIPPLE	HOME DEPOT	1
11	WBB352371	BRASS 125 LB LEAD FREE FITTING 1" X 1/2" REDUCING COUPLING NPT FEMALE 0.68" THREAD ENGAGEMENT	GLOBAL INDUSTRIAL	1

Figure 55-Pressure Test setup exploded view

Start-up Procedure:

1) The Pressure regulator must be set to 1Psi, and the nut should be tightly closed after marking the position of the nut with a marker. (This marking is done, to check whether it has been loosened after prolonged use)

2) The **flow controller** on the compressor and the **flow regulator** must be fully open.

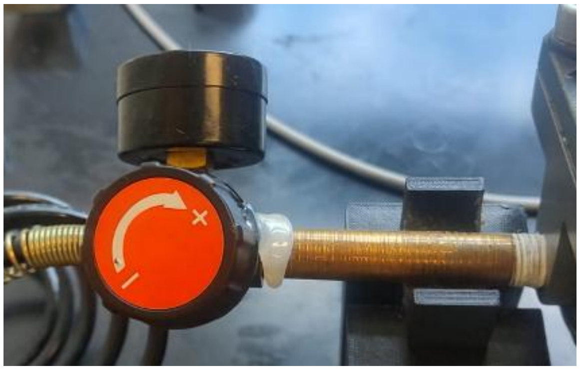

Figure 56-Flow controller on compressor and regulator

3) While starting the equipment, make sure to have the oscilloscope on with a supply of 24 VDC and 1.00Amps of current

4) Only the compressor turned on until it reached 50 Psi.

Pressure Tube Testing Procedure:

1. Ensure compressed air tank is still properly pressurized (between 25-50 PSI. (Refer back to set up procedure as necessary)
2. Apply a liberal amount of Molykote 111 lubricant to the male NPT threads of the pressure, especially the flat face/shoulder—to ensure proper sealing.
3. Thread the tube into a matching female fitting until the flat face was flush and some lubricant oozed out. Use a large adjustable wrench if necessary to ensure proper fit but use care not to overtighten and damage the tubes threads.
4. When ready to perform the test, begin the data logging.
5. Slowly open the valve while monitoring the pressure reading from the sensor. Close the valve once pressure hits 1.0 psi.
6. Monitor the sensor readings while it decays until it drops below 0.05–0.1 psi.

7. Stop the data logging.

8. Unscrew tube and repeat, as necessary.

6.2 Appendix B

6.2.1 Tensile Coupon Testing Protocol

All tensile testing was conducted using an Instron 68TM-10 Mechanical Tester equipped with 5 kN manual wedge grips featuring wide V-jaw faces, mounted on a 10 kN load cell. Prior to testing, the Instron system was reserved two days in advance.

All tensile coupons were printed one day prior to testing to ensure dimensional stability and material consistency.

Testing was performed following the standardized in-lab protocol accessible through the iLabs Kiosk system. The procedure is summarized below:

1. Instrument Setup and Session Initialization:

   The Instron was accessed via the *MEB iLabs Kiosk* by signing in through Chrome using the institutional student account. A new session was created under *Mechanical Testers → Instron → Create Session → Start*. The physical test log located on the instrument clipboard was completed prior to initiating the test.

2. Software Configuration:

   The Bluehill Universal software was launched on the Instron desktop using the login credentials:

   - Username: User
   - Password: InstronUser

The “Tensile_test_insitu_method” file was selected under the *Methods* tab. After confirming the preset limits (pressing “OK” when prompted), the upper grip was adjusted to a 67 mm separation, following the standard setup procedure.

3. Input Parameters:

   The following parameters were entered into the Bluehill interface:

   - Operator name
   - Printer serial number (corresponding to the printer used for coupon fabrication)
   - Coupon label (starting from “01” and incrementing sequentially)
   - Coupon bed location (A, B, C, or D)
   - Date of testing
   - Measured diameter (average of four calliper readings, in mm)
   - Measured gauge length (using callipers, in mm)

4. Testing Procedure:

   Each coupon was mounted in the grips with the brim facing downward. Grip separation was adjusted as necessary using the Instron remote’s up/down controls. The force and displacement channels were zeroed using the buttons labelled *1* and *2* on the remote.

The test was initiated by pressing the unlock button followed immediately by the play button. The machine was allowed to run automatically until coupon failure. In the event of slippage, the incident was recorded in the data sheet, the jaws were re-tightened, and the same coupon ID was retained before re-running the test.

5. Post-Test Data Recording:

   After fracture, the failure height was measured from the bottom of the coupon and recorded under *Height of Crack from Bottom Up*. The jaw separation was reset to 67 mm using the remote. The next coupon’s diameter and gauge length were measured with calliper's and entered into the system before continuing the next test. This process was repeated for 24 coupons per filament model.

6. Data Export and Storage:

   Upon completion, two data files were exported:

   - The complete dataset (CSV)
   - The raw data file for each test

Both files were saved in the designated samples directory. Filenames were renamed following the convention:

- Complete dataset → VendorID_Tensiletest.csv (e.g., *V08_Tensiletest.csv*)
- Raw dataset → VendorID_Tensiletest_raw (e.g., *V08_Tensiletest_raw*)

A PDF report was generated via the *Report → Printer → PDF* sequence within the Bluehill interface, ensuring that the save path matched the CSV directory.

7. Session Closure and Documentation:

   The iLabs session was then finalized, and the user signed out of both iLabs and the Chrome browser. The physical log sheet on the clipboard was completed, and data were entered into the centralized spreadsheet Tensile_Test_Data_Phase_2.xlsx for recordkeeping and analysis.

Figure 57 & 58 shows the tensile coupon geometry and test setup.

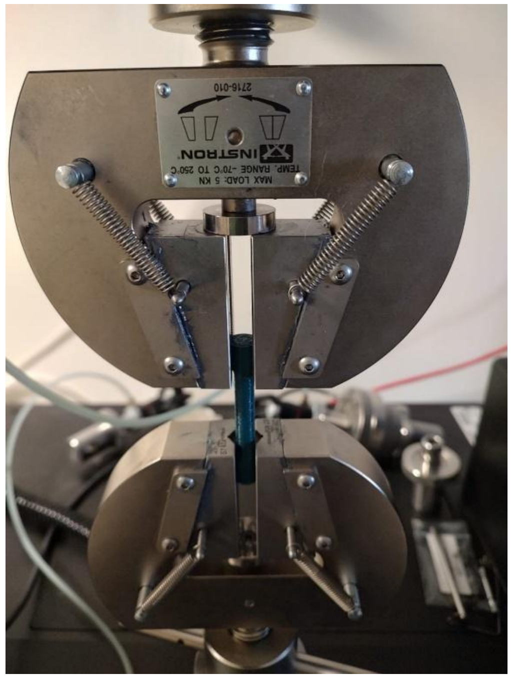

Figure 58- Close up view of a sample coupon inside the Instron

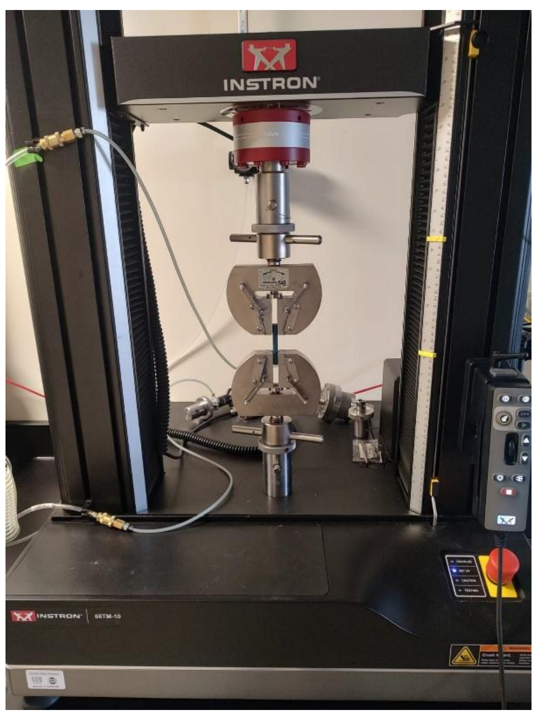

Figure 57-Instron 68TM-10